

## MAGNETOSPHERE IMAGING INSTRUMENT (MIMI) ON THE CASSINI MISSION TO SATURN/TITAN

S. M. KRIMIGIS<sup>1,\*</sup>, D. G. MITCHELL<sup>1</sup>, D. C. HAMILTON<sup>2</sup>, S. LIVI<sup>1</sup>,  
J. DANDOURAS<sup>4</sup>, S. JASKULEK<sup>1</sup>, T. P. ARMSTRONG<sup>5</sup>, J. D. BOLDT<sup>1</sup>,  
A. F. CHENG<sup>1</sup>, G. GLOECKLER<sup>2</sup>, J. R. HAYES<sup>1</sup>, K. C. HSIEH<sup>6</sup>, W.-H. IP<sup>3</sup>,  
E. P. KEATH<sup>1</sup>, E. KIRSCH<sup>3</sup>, N. KRUPP<sup>3</sup>, L. J. LANZEROTTI<sup>7</sup>, R. LUNDGREN<sup>2</sup>,  
B. H. MAUK<sup>1</sup>, R. W. McENTIRE<sup>1</sup>, E. C. ROELOF<sup>1</sup>, C. E. SCHLEMM<sup>1</sup>,  
B. E. TOSSMAN<sup>1</sup>, B. WILKEN<sup>3</sup> and D. J. WILLIAMS<sup>1</sup>

<sup>1</sup>*Applied Physics Laboratory, The Johns Hopkins University, 11100 Johns Hopkins Road, Laurel, MD 20723-6099, U.S.A.*

<sup>2</sup>*Department of Physics, University of Maryland, College Park, MD 20742, U.S.A.*

<sup>3</sup>*Max-Planck Institut für Aeronomie, D-37191, Katlenburg-Lindau, Germany*

<sup>4</sup>*Centre d'Etude Spatiale des Rayonnements, CNRS/Université Paul Sabatier, F-31028 Toulouse Cedex 4, France*

<sup>5</sup>*Department of Physics and Astronomy, University of Kansas, Lawrence, Kansas 66044*

<sup>6</sup>*Department of Physics, University of Arizona, Tucson, AZ 85721, U.S.A.*

<sup>7</sup>*Bell Laboratories, Lucent Technologies, 700 Mountain Avenue, Murry Hill, NJ 07974, U.S.A.*

(\*Author for correspondence: E-mail: Tom.Krimigis@jhuapl.edu)

(Received 16 September 1998; Accepted in final form 7 November 2002)

**Abstract.** The magnetospheric imaging instrument (MIMI) is a neutral and charged particle detection system on the Cassini orbiter spacecraft designed to perform both global imaging and in-situ measurements to study the overall configuration and dynamics of Saturn's magnetosphere and its interactions with the solar wind, Saturn's atmosphere, Titan, and the icy satellites. The processes responsible for Saturn's aurora will be investigated; a search will be performed for substorms at Saturn; and the origins of magnetospheric hot plasmas will be determined. Further, the Jovian magnetosphere and Io torus will be imaged during Jupiter flyby. The investigative approach is twofold. (1) Perform remote sensing of the magnetospheric energetic ( $E > 7$  keV) ion plasmas by detecting and imaging charge-exchange neutrals, created when magnetospheric ions capture electrons from ambient neutral gas. Such escaping neutrals were detected by the Voyager I spacecraft outside Saturn's magnetosphere and can be used like photons to form images of the emitting regions, as has been demonstrated at Earth. (2) Determine through in-situ measurements the 3-D particle distribution functions including ion composition and charge states ( $E > 3$  keV/e). The combination of in-situ measurements with global images, together with analysis and interpretation techniques that include direct "forward modeling" and deconvolution by tomography, is expected to yield a global assessment of magnetospheric structure and dynamics, including (a) magnetospheric ring currents and hot plasma populations, (b) magnetic field distortions, (c) electric field configuration, (d) particle injection boundaries associated with magnetic storms and substorms, and (e) the connection of the magnetosphere to ionospheric altitudes. Titan and its torus will stand out in energetic neutral images throughout the Cassini orbit, and thus serve as a continuous remote probe of ion flux variations near  $20R_S$  (e.g., magnetopause crossings and substorm plasma injections). The Titan exosphere and its cometary interaction with magnetospheric plasmas will be imaged in detail on each flyby. The three principal sensors of MIMI consists of an ion and neutral camera (INCA), a charge-energy-mass-spectrometer (CHEMS) essentially identical to our instrument flown on the ISTP/Geotail spacecraft, and the low energy magnetospheric measurements system (LEMMS), an advanced design of one of our sensors flown on the Galileo spacecraft. The INCA head is a large geometry factor ( $G \sim 2.4$  cm<sup>2</sup> sr) foil time-of-flight (TOF)



*Space Science Reviews* **114**: 233–329, 2004.

© 2004 Kluwer Academic Publishers. Printed in the Netherlands.

camera that separately registers the incident direction of either energetic neutral atoms (ENA) or ion species ( $\geq 5^\circ$  full width half maximum) over the range  $7 \text{ keV/nuc} < E < 3 \text{ MeV/nuc}$ . CHEMS uses electrostatic deflection, TOF, and energy measurement to determine ion energy, charge state, mass, and 3-D anisotropy in the range  $3 \leq E \leq 220 \text{ keV/e}$  with good ( $\sim 0.05 \text{ cm}^2 \text{ sr}$ ) sensitivity. LEMMS is a two-ended telescope that measures ions in the range  $0.03 \leq E \leq 18 \text{ MeV}$  and electrons  $0.015 \leq E \leq 0.884 \text{ MeV}$  in the forward direction ( $G \sim 0.02 \text{ cm}^2 \text{ sr}$ ), while high energy electrons (0.1–5 MeV) and ions (1.6–160 MeV) are measured from the back direction ( $G \sim 0.4 \text{ cm}^2 \text{ sr}$ ). The latter are relevant to inner magnetosphere studies of diffusion processes and satellite microsignatures as well as cosmic ray albedo neutron decay (CRAND). Our analyses of Voyager energetic neutral particle and Lyman- $\alpha$  measurements show that INCA will provide statistically significant global magnetospheric images from a distance of  $\sim 60 R_S$  every 2–3 h (every  $\sim 10 \text{ min}$  from  $\sim 20 R_S$ ). Moreover, during Titan flybys, INCA will provide images of the interaction of the Titan exosphere with the Saturn magnetosphere every 1.5 min. Time resolution for charged particle measurements can be  $< 0.1 \text{ s}$ , which is more than adequate for microsignature studies. Data obtained during Venus-2 flyby and Earth swingby in June and August 1999, respectively, and Jupiter flyby in December 2000 to January 2001 show that the instrument is performing well, has made important and heretofore unobtainable measurements in interplanetary space at Jupiter, and will likely obtain high-quality data throughout each orbit of the Cassini mission at Saturn. Sample data from each of the three sensors during the August 18 Earth swingby are shown, including the first ENA image of part of the ring current obtained by an instrument specifically designed for this purpose. Similarly, measurements in cis-Jovian space include the first detailed charge state determination of Iogenic ions and several ENA images of that planet's magnetosphere.

**Keywords:** energetic neutral atoms, gas – plasma interaction, hot plasma composition, magnetospheric imaging, planetary magnetosphere, Saturn magnetosphere, space instrumentation, trapped energetic charge particles

## 1. Introduction

Saturn, its atmosphere, rings, moons, and plasma envelope or magnetosphere, are all closely coupled and interact through the exchange of matter and energy. A comprehensive study and understanding of Saturn's plasma environment is a central objective for the Cassini mission. The Voyager and Pioneer encounters with Jupiter and Saturn, the Ulysses encounter with Jupiter, the Voyager 2 encounters with Uranus and Neptune, and the Galileo Jupiter orbiter have provided important new insights into magnetospheric processes.

- (a) Planetary magnetospheres are mostly populated by energized ionospheric and satellite material.
- (b) Planetary magnetospheres inject fast neutral atoms, plasmas and energetic particles into the interplanetary medium.
- (c) Energetic particles and plasmas modify the atmospheres and surfaces of natural satellites.
- (d) Solar wind plasma pressure on planetary magnetic fields establishes the bow shock, magnetopause, magnetotail, and apparently energizes magnetospheric substorms, but it apparently is not the dominant source for the magnetospheric energetic particle populations.

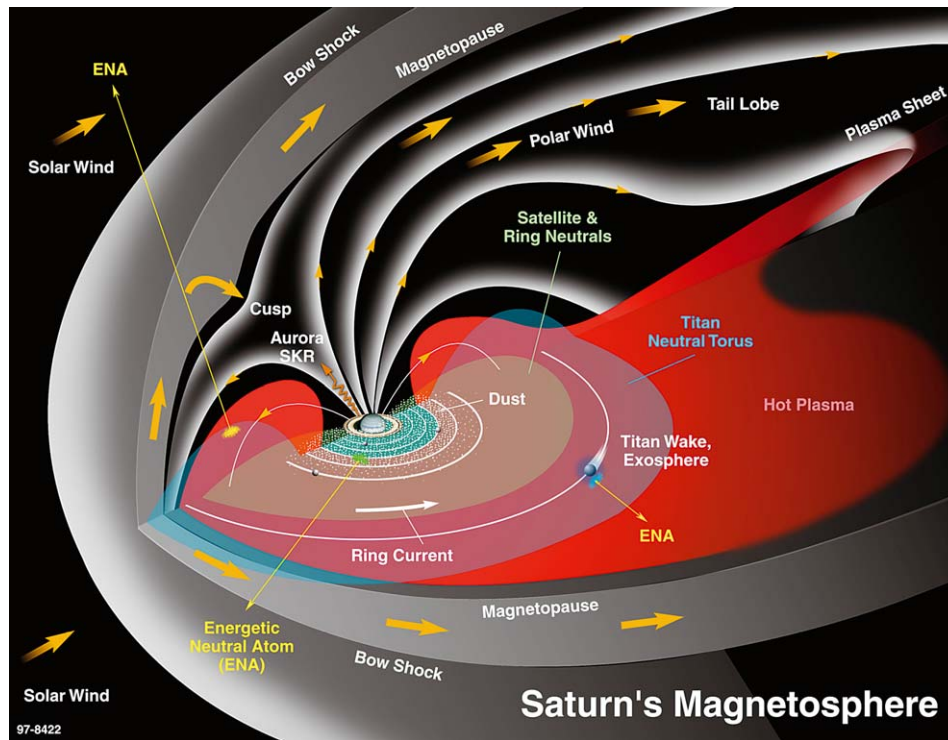


Figure 1. Saturn's magnetosphere.

In the case of Saturn, Titan presents a dense atmosphere within Saturn's magnetosphere where escape of atmospheric constituents contributes to a neutral gas cloud that is an important (perhaps dominant) source of plasma for the magnetosphere.

The Pioneer 11 and Voyager 1 and 2 encounters with the Saturn system have established the existence of a large and complicated magnetosphere, whose global configuration and dynamics are shaped not only by interactions with the solar wind and the planetary atmosphere, but also by interactions with the planetary rings and satellites (Figure 1). At Jupiter, interactions with planetary satellites, particularly Io, are of dominant importance for the magnetospheric mass and energy budgets, but it is not yet clear whether satellite-magnetosphere interactions are comparably important at Saturn.

The Cassini mission to the Saturn system will provide a unique opportunity for exploration of the magnetosphere and investigation of magnetospheric processes. Saturn's aurora may be powered by a solar wind interaction or a Titan interaction, but it is not related to interactions with the icy satellites of the inner magnetosphere. Saturn's kilometric radio emissions are strongly affected by solar wind interaction. On the other hand, the plasmas in the inner magnetosphere are dominated by heavy ions, most likely from the magnetospheric interaction with

the icy moons. Nevertheless, the cometary interaction between the magnetosphere and Titan as well as the interaction with Saturn's atmosphere both yield important plasma sources. A fundamental objective of the Cassini mission will be to clarify the relative importance of these interactions for the global mass and energy budgets. Another important objective of the Cassini mission will be to determine if there are substorms in Saturn's magnetosphere. Evidence for Earth-like substorm activity has so far been found in the magnetospheres of Mercury, Uranus, Neptune, and most recently Jupiter (Mauk *et al.*, 1997a). The question of whether substorms are a universal magnetospheric phenomenon is of fundamental importance in space plasma physics.

### 1.1. MEASUREMENTS APPROACH

To address these science issues, MIMI will carry out remote sensing of the magnetosphere by imaging energetic charge-exchange neutrals and also perform in-situ measurements of ion 3-D distributions, composition, and charge state.

The combination of imaging observations and in-situ measurements of the magnetosphere can be expected to yield a far greater science return than either of these types of measurement alone. This is amply demonstrated by experience with combined remote sensing and local measurements of Earth's aurora (DE, DMSP, Viking, Freja, Polar, etc.) as well as the Io torus of Jupiter (Voyager, Galileo). In-situ measurements provide a "ground truth" that validates inferences from remote sensing; furthermore, they provide important information and constraints to be used in deconvolving structures along the line-of-sight. The imaging observations, on the other hand, provide the global context for the local measurements, revealing global patterns of activity that would be missed or that could not be interpreted unambiguously on the basis of in-situ measurements alone.

Remote sensing of energetic charge-exchange neutrals has been used by Roelof *et al.* (1985) to measure the global decay of Earth's ring current and by Roelof (1987) to obtain images of Earth's ring current. Charge-exchange neutrals have been detected by Voyager from Saturn's magnetosphere out to  $140R_S$  (Kirsch *et al.*, 1981b) and have been the subject of extensive theoretical modeling (Ip, 1984; Cheng, 1986; Hsieh and Curtis, 1988, 1989; Cheng and Krimigis, 1989b). The far more capable MIMI sensors will image the magnetosphere from apoapsis of the Saturn orbiter tour into the inner magnetosphere. If a substorm or some other large-scale dynamic process should occur in Saturn's radiation belts, it would be detected by MIMI even during the extended periods when the orbiter is outside the magnetosphere (this will be a significant fraction of the time). Imaging and synoptic monitoring of the ring current/radiation belt ion populations by MIMI, in conjunction with imaging of the Saturnian aurora and neutral hydrogen clouds by the ultraviolet imaging spectrograph (UVIS) instrument, should greatly clarify the nature of Saturn's aurora and magnetospheric coupling to Saturn's atmosphere. Imaging

and synoptic monitoring of Titan's cometary interaction with the magnetosphere by MIMI should likewise clarify the importance of Titan interactions for the magnetosphere and should determine whether Titan is as important for Saturn as Io is for Jupiter.

In addition to the global imaging of the magnetosphere, MIMI will also carry out in-situ measurements of the energetic ion ( $\sim 7$  keV/nuc to  $> 8$  MeV/nuc) and electron (15 keV to  $> 11$  MeV) populations. Ion and electron energy spectra, ion composition, and ion charge state will be measured in order to address fundamental issues concerning the structure and dynamics of the Saturn magnetosphere. Among these are the following: What is the origin of the plasmas in the Saturn system? How and where are the plasmas transported? What processes power Saturn's aurora? What forms of global magnetospheric activity occur, how are they powered, and, specifically, do Earth-like substorms occur? Ion composition and charge state will be measured for the first time in the 10–265 keV/e range, allowing detection and tracking of tracer species from the solar wind, from Saturn's ionosphere, from Titan, and from the icy satellites, not only in the magnetosphere, but also in the upstream solar wind.

## 2. Scientific Objectives

MIMI science objectives may be summarized as follows:

### *Saturn*

- Determine the global configuration and dynamics of hot plasma in the magnetosphere of Saturn through energetic neutral particle imaging of ring current, radiation belts, and neutral clouds.
- Study the sources of plasmas and energetic ions through in-situ measurements of energetic ion composition, spectra, charge state, and angular distributions.
- Search for, monitor, and analyze magnetospheric substorm-like activity at Saturn.
- Determine through the imaging and composition studies the magnetosphere–satellite interactions at Saturn and understand the formation of clouds of neutral hydrogen, nitrogen, and water products.
- Investigate the modification of satellite surfaces and atmospheres through plasma and radiation bombardment.
- Study Titan's cometary interaction with Saturn's magnetosphere (and the solar wind) via high-resolution imaging and in-situ ion and electron measurements.
- Measure the high energy ( $E_e > 1$  MeV,  $E_p > 15$  MeV) particle component in the inner ( $L < 5R_S$ ) magnetosphere to assess cosmic ray albedo neutron decay (CRAND) source characteristics.
- Investigate the absorption of energetic ions and electrons by the satellites and rings in order to determine particle losses and diffusion processes within the magnetosphere.

- Study magnetosphere–ionosphere coupling through remote sensing of aurora and in-situ measurements of precipitating energetic ions and electrons.

#### *Jupiter*

- Study ring current(s), plasma sheet, and neutral clouds in the magnetosphere and magnetotail of Jupiter during Cassini flyby, using global imaging and in-situ measurements.

#### *Interplanetary*

- Determine elemental and isotopic composition of local interstellar medium through measurements of interstellar pickup ions.
- Study the compositional evolution at low energies of shock-accelerated ions in the interplanetary medium.
- Monitor cosmic ray intensity variations ( $E_p > 70$  MeV/nuc) and anomalous cosmic rays, and compare with similar measurement in both the inner heliosphere (advanced composition explorer, ACE) and the outer heliosphere (Voyagers 1 and 2).

### 2.1. GLOBAL IMAGING

The most fundamental relationship in physics is that of cause and effect, and the study of the magnetospheres of the giant planets has been a valiant struggle with the inseparability of temporal and spatial variations along the flyby trajectories of Pioneers 10/11, Voyagers 1/2, and Ulysses. The exciting new observations from the Galileo orbiter are adding another dimension to our understanding, just as the Cassini orbiter certainly will. However, the most dramatic and unambiguous signatures of magnetospheric electrodynamics will come from imaging the ion populations across the huge expanses of the Saturnian magnetosphere. The ion and neutral camera (INCA) will image energetic neutral atoms (ENAs) that are produced when energetic, singly charged ions undergo charge-exchange collisions with the cold neutral gas that pervades the ion populations. Because the ENA trajectories are straight lines originating at the location of the charge-exchange collision, the counting rate in each INCA pixel of the sky is proportional to the line-of-sight integral of the ion intensity (in the direction of the spacecraft) weighted by the cold neutral densities  $n_i$  and the corresponding charge-exchange rate  $\sigma_i$ :  $j_{\text{ENA}} = \sum \sigma_i \int ds n_i j_{\text{ION}}$ . Because INCA can resolve ENA hydrogen from ENA oxygen, these two species can be analyzed separately.

Nonetheless, even with resolution of H from O, the unfolding of the ion intensities from the INCA images will probably require sophisticated minimization algorithms in which parametric models of the ion intensities (and the neutral densities) are optimized so that the difference between the measured INCA pixel rates and those predicted by the models is a minimum (in a  $\chi$ -squared sense).

TABLE I

Measured neutral atom fluxes from planetary magnetospheres near 40 keV energy at large distance  $d$ .

Earth $\sim 100 \left( \frac{d}{R_E} \right)^{-2} \text{ cm}^{-2} \text{ s}^{-1} \text{ keV}^{-1}$ (quiet time)
Jupiter $\sim 440 \left( \frac{d}{R_J} \right)^{-2} \text{ cm}^{-2} \text{ s}^{-1} \text{ keV}^{-1}$
Saturn $\sim 240 \left( \frac{d}{R_S} \right)^{-2} \text{ cm}^{-2} \text{ s}^{-1} \text{ keV}^{-1}$
Uranus $< 12 \left( \frac{d}{R_U} \right)^{-2} \text{ cm}^{-2} \text{ s}^{-1} \text{ keV}^{-1}$
Neptune $< 4 \left( \frac{d}{R_N} \right)^{-2} \text{ cm}^{-2} \text{ s}^{-1} \text{ keV}^{-1}$

Energetic charge-exchange neutral emissions have been detected from the magnetospheres of Earth, Jupiter, and Saturn. Table I compares the measured neutral atom source strengths near 40 keV of five planetary magnetospheres (McEntire and Mitchell, 1989). The fluxes given in Table I are integrated over the source and apply for large distances compared to the source size. The source strengths agree with theoretical expectation (e.g., Ip, 1984; Cheng, 1986; Barbosa and Eviatar, 1986; Krimigis *et al.*, 1988).

At Earth, where ENA imaging was first developed and demonstrated, the cold neutral density takes the comparatively simple form of a nearly spherically symmetrical Chamberlin exosphere of H atoms. Not so at Saturn. Reinterpretation of the Voyagers 1/2 UVS Lyman- $\alpha$  emission demands an H-atom distribution that is more disk-like than spherical, and moreover cannot even be axially symmetric about the planet's rotation axis (Shemansky and Hall, 1992; Ip, 1996). The presence of a large amount of H in the inner system ( $r < 10R_S$ ) implies that Saturn's exosphere is a significant source, but in the outer system, Ip argued that Titan should produce significant densities of H ( $10 < n_H < 10^2 \text{ cm}^{-3}$ ) extending up to  $8R_S$ . Furthermore, Ip (1997) has recomputed the original estimates of Johnson *et al.* (1989) for the contributions of the icy moons (Enceladus, Tethys, Dione, and Rhea). He finds concentrations of O, OH, and H<sub>2</sub>O in the range  $10^2$  to  $10^4 \text{ cm}^{-3}$  in the inner system ( $3\text{--}6R_S$ ), although they are strongly confined to the equatorial plane.

Using the early models for the neutrals distribution, we have simulated idealized ENA images for INCA in Figure 2. "Fish-eye" lens projections of ENA fluxes ( $>35 \text{ keV H}$ ) are shown for four locations of Cassini. The bright object in the three more distant images is Titan's exosphere, and the putative Titan torus would be seen through most of the orbit. The color bar is logarithmic, ranging from 1 to 100% of the brightest ENA lines in each image.

*Images from  $50R_S$ .* Figure 3 shows Saturn and the Titan torus as viewed from the equatorial dawn meridian; distorted dipole field lines are drawn to show compression of the magnetosphere on the front side with the magnetopause at (a)  $25R_S$ , and (b)  $20R_S$ . Panel (c) shows the accumulated counts for (a) and (b) (upper

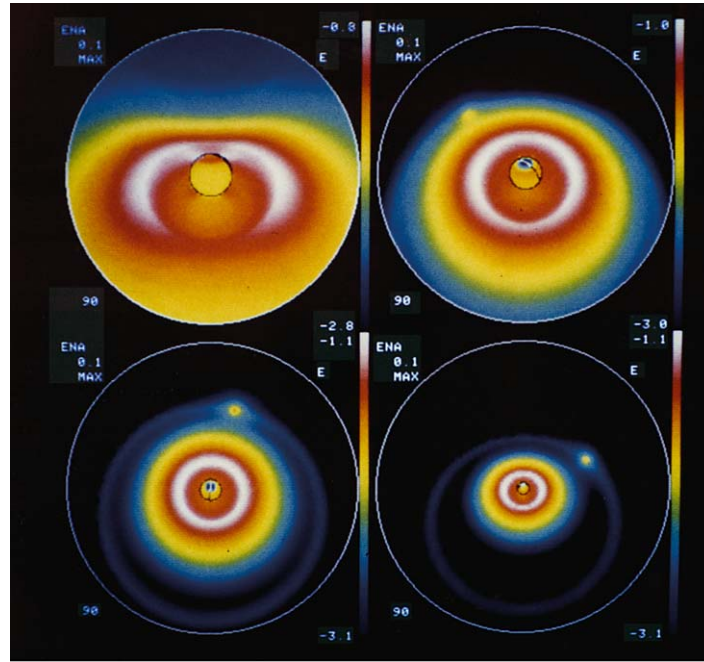


Figure 2. Four idealized ENA images ( $1 \times 1^\circ$  angular resolution, no Poisson statistical fluctuations in pixel counts) of the Saturn/Titan system, based on Voyager  $>35$  keV CPME ion measurements and early interpretation of UV observations. “Fish-eye” projection is hemisphere centered on planet (terminator indicated in black). Logarithmic color bar ranges from 1 to 100% of brightest emission in each image. Magnetosphere extends to  $25R_S$ , and Titan exosphere is shown with putative plasma torus. Cassini positions are every  $30^\circ$  of mean anomaly for inclined orbit with radius, solar longitude, magnetic latitude: (a)  $4.4R_S$ ,  $21^\circ$ ,  $26^\circ$ ; (b)  $5.9R_S$ ,  $39^\circ$ ,  $55^\circ$ ; (c)  $9.0R_S$ ,  $100^\circ$ ,  $71^\circ$ ; and (d)  $15.5R_S$ ,  $161^\circ$ ,  $55^\circ$ .

and lower curves, respectively) for a 20-min accumulation. The complete image contains 1163 counts ( $\sim 10\%$  statistics in inner ring current, 30% at  $L = 8$ ). Most importantly, ENA emission from the dayside Titan torus is significantly diminished as the magnetopause moves inward, thus enabling continuous remote sensing of such compressions, which is not possible through any other technique.

The implications of this complicated neutral distribution for ENA imaging can be looked at two ways. On one hand, it makes the problem of extracting absolute ion intensities from global ENA images extremely challenging. Clearly the Cassini UV measurements of the neutral environment and the INCA ENA intensities must be correlated wherever possible. On the other hand, the concentration of the neutrals close to the equatorial plane actually simplifies the geometry for ion injection events on localized magnetic flux tubes. At Earth, ion injection events are often difficult to analyze precisely because of the spherical distribution of the H atoms – the entire flux tube “lights up” in ENA, making it hard to determine the region of  $L$  and mean local time (MLT) containing the injection. However, at Saturn, it will be mainly the equatorial region that will emit the ENA, thus giving directly the  $L$ -MLT



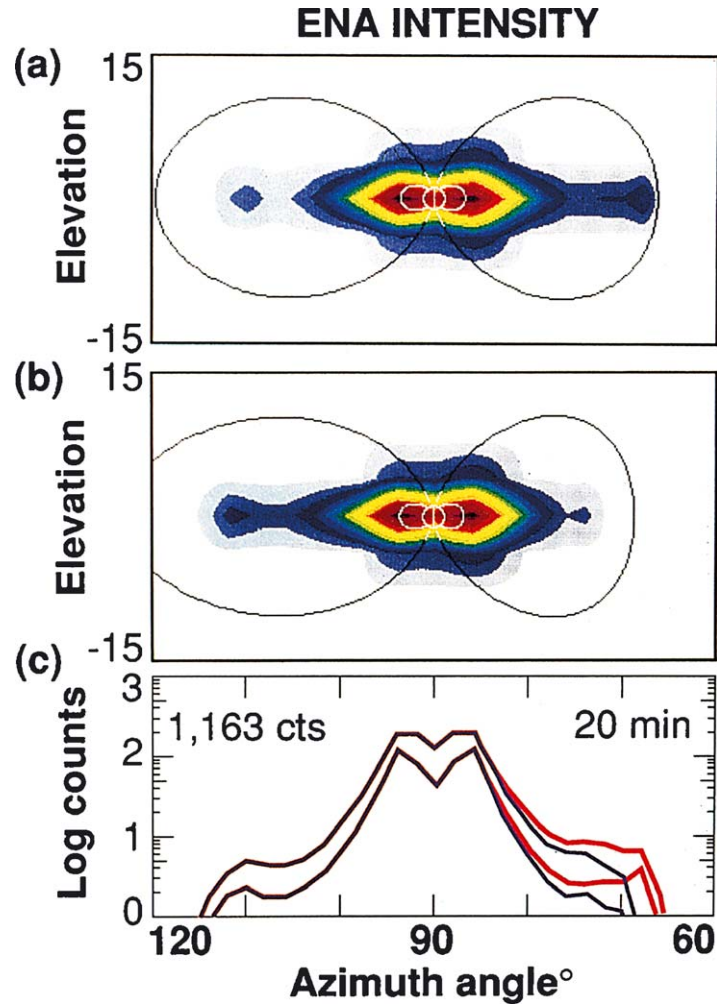


Figure 3. Simulated ENA images ( $Y = -50R_S$ ) of magnetopause compression from (a)  $25R_S$  to (b)  $20R_S$  detected by (c) change in Titan torus within 20 min (for 30–60 keV H).

location of the ion injection (without complicated unfolding of the line-of-sight integrals).

Consequently we anticipate that INCA, in combination with CHEMS and LEMMS, will produce immediate and quantitative identification of the regions of ion acceleration in Saturn's magnetosphere, some of which we can expect by analogy to the Earth-like ion injection events identified at Jupiter by Mauk *et al.* (1997a) using the Galileo energetic particle detector. It will be the causal relationships – what ions were accelerated where and when – that we look forward to discovering with INCA's global imaging.

## 2.2. SATELLITE INTERACTIONS AND AURORA

### 2.2.1. *Magnetosphere–Satellite Interactions*

A major magnetospheric goal of the Cassini mission is the measurement of the environments of the Saturnian moons and the determination of their interaction with the Saturnian magnetosphere. To this end the Cassini spacecraft will conduct numerous close (<2000 km) encounters with the moons Titan, Iapetus, Hyperion, Rhea, Dione, and Enceladus. Observations from such close encounters provide the measurements required to determine the environment of the moon and its magnetospheric interaction. In particular, energetic particle measurements with the LEMMS sensor during close flybys provide vital and often unique results that identify the character of the moon–magnetosphere interaction. For example, as has been shown at Jupiter, energetic particle observations provide a measure of the moon's surface magnetic field (Williams *et al.*, 1997b); directly measure the effect of the moon and its environment on the convecting magnetospheric plasma (Williams *et al.*, 1997a); provide a direct measure of the amount of scattering occurring on planetary field lines intersecting the moon (Williams and Mauk, 1997); provide a measure of the conductivity of the moon and its environment (Paranicas *et al.*, 1998); provide a direct measure of the effectiveness of sputtering in the formation of the moon's atmosphere, ionosphere, and associated gas torus as well as for surface mass redistribution effects (Ip *et al.*, 1997, 1998; Lagg *et al.*, 1998); and for moons with magnetic fields can identify the existence of trapped particles within that field (Williams *et al.*, 1997a).

On a broader scale, simultaneous observations by MIMI and the ultraviolet spectrometer will further elucidate the effects of magnetospheric interactions with Titan and the icy moons. The ultraviolet spectrometer observations will provide the H column density along the same lines of sight viewed by MIMI, enabling the energetic ion distributions to be obtained from the ENA images. The ENA images, obtained separately for each species, will allow a determination of the composition of the distant energetic ion population, thus providing a measure of the strengths of the various moons as sources of magnetospheric ions.

### 2.2.2. *Saturn's Aurora and Magnetospheric Activity*

Saturn's auroral energetics and morphology are Earth-like rather than Jovian, suggesting that the aurora is powered by a solar wind interaction (Sandel and Broadfoot, 1981). Alternatively, Barbosa (1987) has argued that Saturn's aurora may be powered by a Titan interaction with the magnetosphere. MIMI measurements during the many flux tube crossings at Titan will directly test this possibility. For example, at Jupiter's moon Io, intense energetic electron beams were measured flowing in both directions along Jovian field lines adjacent to Io (Williams *et al.*, 1996). An Io flux tube full of these beams would lead to aurorae at its footprint in the Jovian atmosphere. The flux tube measurements to be made with LEMMS at Titan will yield the energy content of the particles flowing into Saturn's atmosphere and thus

measure the auroral producing capability of the moon. The existence or absence of field-aligned beams at Titan will assess the effectiveness of Titan (and its environment) in converting the induced electric field resulting from its motion through the Saturnian magnetosphere into a magnetic field-aligned potential drop. Finally MIMI will search for field-aligned particle flows in the high latitude regions of Saturn's magnetosphere and directly test for the existence of field-aligned auroral zone potentials above  $\sim 10$  keV. Measurements from MIMI will determine whether the resulting energetic particle precipitation is sufficient to excite aurorae.

The existence of aurorae implies the existence of substorms. At Earth the solar wind interaction with the magnetosphere provides the dominant energy source for substorms. It is not clear what the mechanism for substorm phenomena would be at Jupiter and Saturn and, until the recent systematic study of the Jovian environment by the energetic particle instrument on Galileo by Krupp *et al.* (1998) and by Woch *et al.* (1998, 1999), it was not known whether Jupiter and Saturn could be expected to display substorm phenomena. Energetic ion and electron measurements in the Jovian magnetosphere show signatures that are basically identical to substorm injection events observed at Earth (Mauk *et al.*, 1997a). Measurements of the energy dispersion of both ions and electrons show particle injection over a narrow longitudinal band and subsequent magnetic gradient drift superimposed on magnetospheric corotation. Because of the overwhelming effect of corotation, the dispersion is best observed in the energetic particle population and is very difficult to observe at low energies. Thus, with the existence of aurorae at Saturn, it is reasonable to expect to observe substorm signatures. MIMI will provide the best opportunity to observe such signatures.

### 2.2.3. Ring Interactions

An important goal of the MIMI investigation is to understand the interactions between the planetary magnetospheric environments and Saturn's planetary rings. From the perspective of planetary ring science, charged particle environments can electrically charge ring and other particulates, thereby affecting the transport of the particulates, and perhaps of larger ring members, via collisions with the particulates (Mendis *et al.*, 1984; Goertz, 1989). The "spokes" of Saturn are the best-known example, and the braiding of the F-ring may also have an electromagnetic origin (Mendis *et al.*, 1984). Energetic charged particles can modify, sputter, and erode ring particle surfaces (Johnson, 1990). In addition, charged particle distributions can provide powerful diagnostics on the presence, character, and distributions of sparse ring materials (Krimigis and Armstrong, 1982; Esposito *et al.*, 1984). From the magnetospheric science perspective, rings provide important sources and sinks of the neutral and charged particles of planetary environments (e.g., Krimigis and Armstrong, 1982; Van Allen, 1984). Also, ring/charged-particle interaction features provide powerful diagnostics on the transport of charged particles within the magnetospheric environments (e.g., Van Allen, 1984; Mauk *et al.*, 1994). Finally, the charged particle and ring particulate environments of planetary magnetospheres

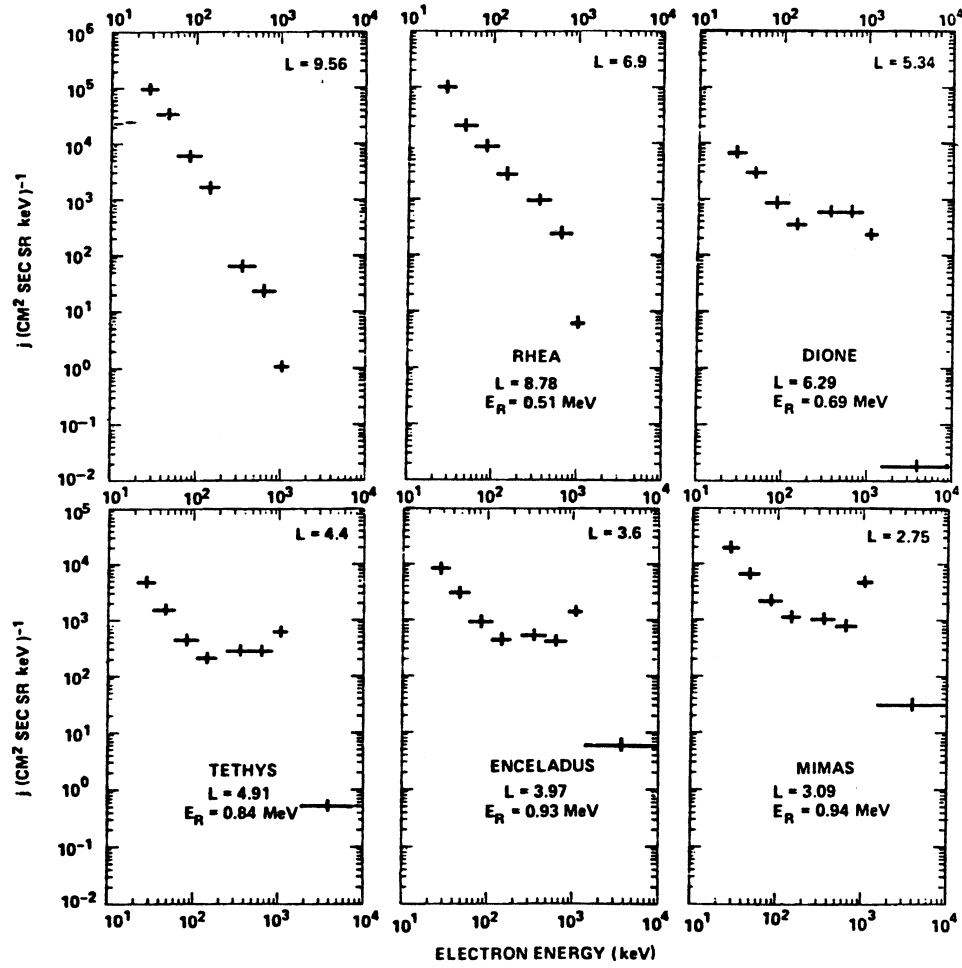


Figure 4. The evolution of the electron energy spectrum at various  $L$  values, upper left to lower right, as registered by LECP on Voyager 2. The  $L$  values are indicated in each panel, and the resonant electron energy  $E_R$  at each satellite is shown in successive panels. From Krimigis *et al.* (1982a).

are perhaps the best laboratories for studying certain aspects and phases of the formation of planetary nebula (Burns *et al.*, 1994).

Numerous signatures of the interaction between energetic charged particles and ring particles were observed by Pioneer 11 and the Voyagers 1 and 2. Figures 4 and 5 show, respectively, examples of explicit radial profile signatures and bite-outs in pitch angle distributions attributed to the effect of ring dust materials. However, the ENA imaging capabilities of INCA, combined with the information of energy spectra, angular distribution, and charge state obtained with LEMMS and CHEMS, provides a powerful new technique for diagnosing ring-particulate/energetic-particle interactions, as described below.

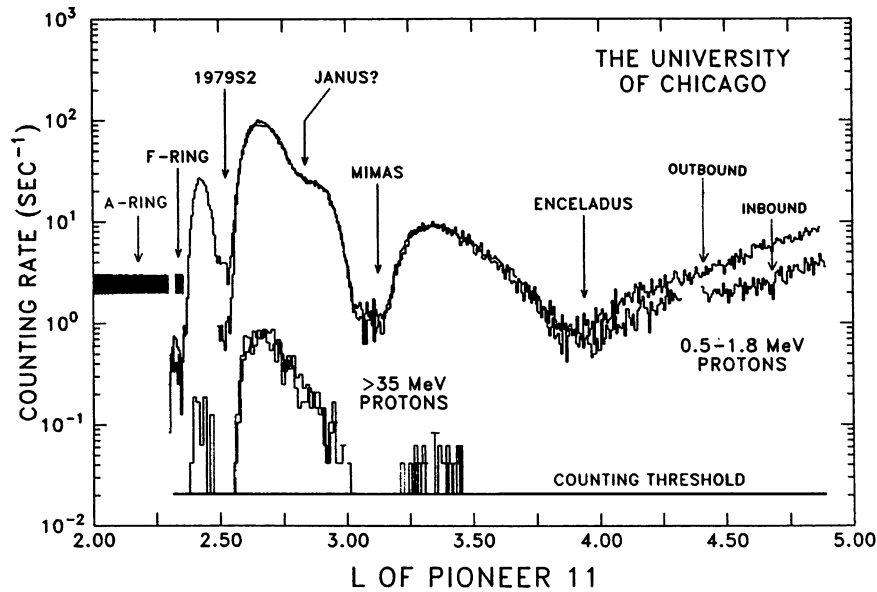
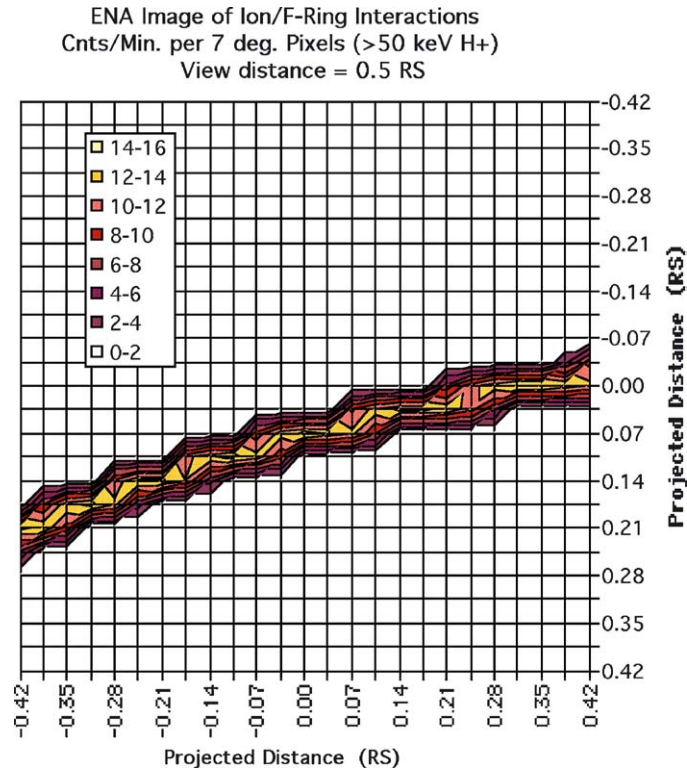


Figure 5. Energetic ions measured by Pioneer 11 in Saturn's inner magnetosphere (after Simpson *et al.*, 1980).

The intense populations of magnetically trapped, energetic charged particles that constitute the radiation belts of Saturn's inner magnetosphere are slowly transported towards the planet by radial diffusion processes. Many of them interact with the rings of Saturn and ultimately are lost to the magnetospheric system. Energetic protons with energies greater than  $\sim 50$  keV will completely penetrate ring particulates with diameters in the sub-micron regime, such as those that are key constituents of the F, G, and E rings of Saturn. A substantial fraction of those penetrating protons ( $\sim 60\%$  at 50 keV) will emerge neutralized by the interaction, ending up as hydrogen ENAs. Thus, the interactions between the trapped energetic particles and the ring particulates may be observed remotely by an ENA camera that measures the energy, mass species, and the arrival direction of ENAs. The ability of the INCA sensor of the MIMI instrument to image energetic-particle/ring-particulate interactions within Saturn's inner magnetosphere during the SaturN orbit insertion (SOI) phase of the Cassini mission was recently documented by Mauk *et al.* (1998). A simulated ENA image of Saturn's F-ring from that work is shown in Figure 6. Mauk *et al.* (1998) showed that with such images we can obtain powerful new diagnostics of magnetospheric radial transport of energetic charged particles. Also, the impact rates for the consideration of sputtering and erosion will be better constrained, and the relative importance of the rings as a sink of radiation belt particles will be determined. Finally, the energy spectra of the ENA emissions will provide a new type of constraint on the size distribution of the ring particulates. Figure 7 shows a sample of the modeled sensitivity of the ENA spectra to the dust particulate sizes.



*Figure 6.* Simulated ENA image of a portion of the F-ring as it might appear to the INCA MIMI ENA camera on the Cassini spacecraft at a distance from the ring segment near the center of the image of  $0.5R_S$  during the Saturn orbit insertion phase of the mission. The units are counts per minute. The F-ring dust particulates are assumed to have a size of  $0.5 \mu m$ . A lower limit assumption has been made concerning the radial transport of energetic protons ( $\sim 0.01$  km/s). After Mauk *et al.* (1998).

### 2.3. SATURN CHARGED PARTICLE ENVIRONMENT

Saturn's magnetosphere is a prodigious accelerator of charged particles, as apparently are the magnetospheres of all strongly magnetized planets. There is no clear understanding why planetary magnetospheres have this characteristic. Saturn's magnetosphere has unique properties that can help unravel the relative importance of various proposed mechanisms for particle acceleration and transport. Saturn's energetic particle population is also unique in the degree of interaction between the charged particle populations and the neutral and solid materials such as planetary gases, dust and ring materials, and satellite surfaces. Thus, Saturn's magnetosphere may come closest to emulating the conditions that existed within the Sun's planetary nebula and during later stages in the formation of the solar system.

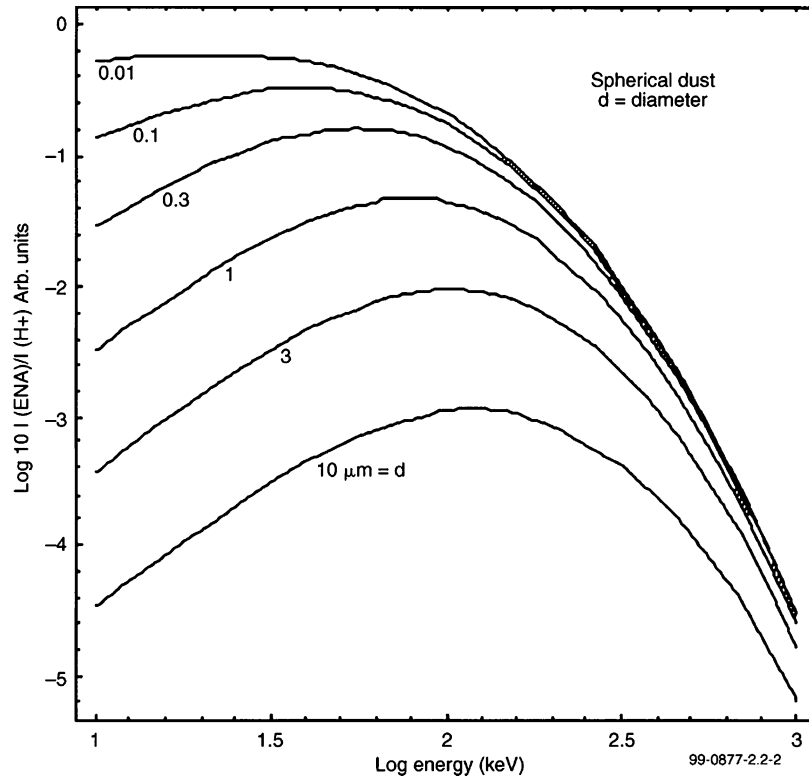


Figure 7. Model calculations of ENA emission energy-spectra from the dust particulates as a function of particulate size and shape. The spectra are normalized by the parent ion spectra. It was assumed the dust particulates are spherical. Other simulations given by Mauk *et al.* (1998) test for sensitivity to particulate shape.

Figure 8 shows Saturn's energetic charged particle environment as characterized with the low energy charged particle (LECP) instrument on Voyager 2 (Krimigis *et al.*, 1983). Energetic particles fill the magnetosphere to the dayside magnetopause and participate in the force balance of the magnetosphere with the interplanetary environment. Energetic particles clearly leak out of the magnetospheric boundary. Strong inbound/outbound (dayside/predusk) asymmetries have been interpreted as being the result of temporal dynamics. Shorter-scale temporal dynamics are also apparent in the so-called "mantle" region (inbound-dayside,  $r > 10R_S$ ), undoubtedly related to dense, detached, cold plasma regions, apparently shed from the interior plasma sheet (Sittler *et al.*, 1983). Large-scale modulations observed in the outbound regions, apparently related to the Saturn rotational modulations reported from the Voyager 1 encounter (Carbary and Krimigis, 1982), are surprising, given the near-exact alignment of Saturn's magnetic axis with its spin axis. Energetic particles in the inner regions show the clear signatures of strong interactions with materials, including the natural satellite surfaces. The very peculiar electron spectra

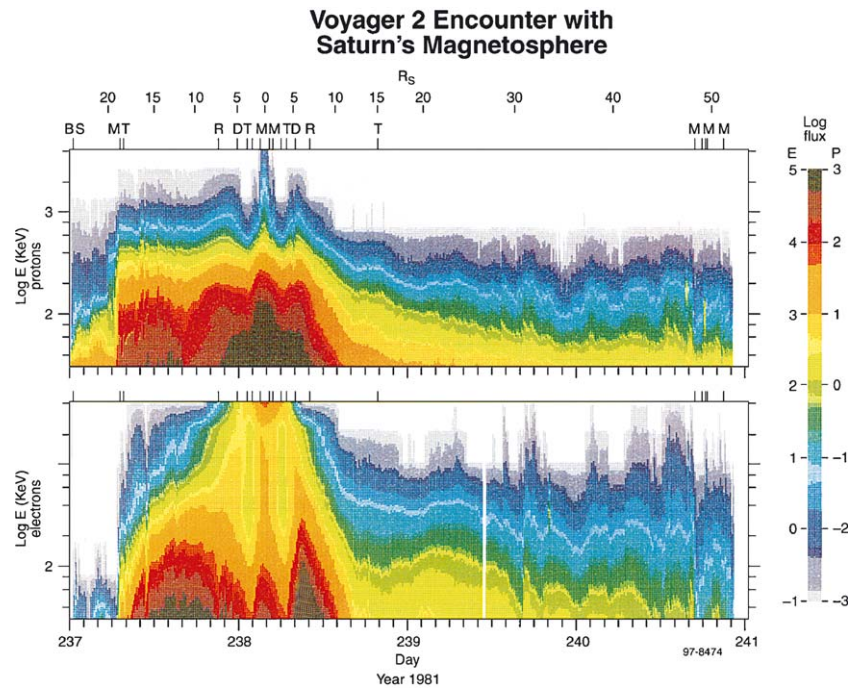


Figure 8. Color spectrogram of energetic ions (top) and electrons (bottom) measured by low energy charged particle (LECP) instrument on Voyager 2 during its encounter with Saturn. The color is coded according to the  $\log_{10}$  of intensity ( $(\text{cm s sr keV})^{-1}$ ). Radial distance (in  $R_S$ ) is given below each color panel, and various events are given above each panel. The events are: BS = bow shock, M (first and last three) = magnetopause, T (first and last) = Titan L-shell, R = Rhea L-shell, D = Dione L-shell, T (middle 2) = Tethys L-shell, and M (middle 2) = Mimas L-shell. The unlabeled tick marks between Tethys and Mimas represent the Enceladus L-shell. After Krimigis *et al.* (1983).

near closest approach (Krimigis *et al.*, 1982a), showing the intensities rising at the highest energies, are interpreted as being the signature of a drift period resonance with orbital period of the satellites (see Figure 4).

The temporal dynamics mentioned above are of particular interest for the MIMI investigation of the Saturnian system. Saturn's magnetosphere is thought to occupy a middle ground between magnetospheres such as that of Earth, whose dynamics and energetics are determined by a strong interaction with the interplanetary medium, and magnetospheres such as that of Jupiter, thought to be controlled predominantly by the rapid rotations of the central planet. By comparing the energetic particle characteristics, and their temporal dynamics among Earth, Jupiter, and Saturn, we will be able to sort out the relative influences of rotational and interplanetary environment on the energization of charged particles to high energy. Temporal dynamic processes at Earth are well characterized, and Galileo is now shedding substantial light on the energetic particle dynamics at Jupiter. MIMI will provide



for an unprecedented characterization of the energetic particle dynamics within the Saturnian magnetosphere.

The critical influence of such materials as dust, rings, and satellite surfaces on the character of the energetic particle populations is shown most clearly in Figure 5 (Simpson *et al.*, 1980). Dust particulates of the F, G, and E-rings clearly have roles to play, as do both the larger particles of the A and F rings and the satellites. Ring interaction signatures are highlighted further in Figure 9 with the 90° bite-outs observed in energetic particle pitch angle distributions measured near the G-ring (Krimigis and Armstrong, 1982). Also, the very high energy component of the spectra shown (the bump at ~100 MeV) has been interpreted as resulting from CRAND from impacts on the rings. LEMMS will be able to measure these features at all local times, various distances, and latitudes over the entire mission of at least 4 years.

Energetic particle composition is another clear signature of the importance of materials interactions for establishing the character of the energetic particle populations. Figure 10 shows that both Jupiter's atmosphere ( $H_2$ ,  $H_3$ ) and the solar wind (He) are contributors to the energetic particle populations, and the presence of heavier ions (C, N, O) are possible tracers of satellite and ring sources (Krimigis *et al.*, 1982b). Evidence not shown here (Krimigis *et al.*, 1983) suggests that oxygen ions dominate the energy density of the ion populations planetward of  $\sim 6R_S$ , indicating that sputtering off the icy satellites may be a dominant source of energetic particles in these regions. The relative strengths of all sources, particularly of Titan versus the icy satellites, is not known. MIMI, with compositional and charge state discrimination capabilities that dwarf previous measurements at Saturn, will establish where the energetic particles come from.

Dust, ring particles, satellites surfaces, and gas distributions help determine the characteristics of the energetic particles, but these materials are in turn modified by the energetic particles. Energetic particles process and change the surfaces of materials (e.g., Johnson, 1990), and they affect the transport of dust, and perhaps larger ring particles (Mendis *et al.*, 1984; Goertz, 1989). The use of MIMI in concert with the comprehensive suite of Cassini instruments (e.g., UVIS measurements of gas distributions, imaging science subsystems (ISS) images of dust distributions, etc.) will allow for an epochal characterization of the solar nebula-like interactions that are now occurring within the Saturnian system.

MIMI will also provide unprecedented new information about several other aspects of the Saturnian energetic particle populations that have remained ambiguous since the Voyager encounters. Previous limitations in ion compositional analysis and angular resolution and coverage have prevented us from achieving closure in the analysis of force balance between magnetic fields and plasmas (Mauk *et al.*, 1985). Saturn appears to be unique in the interplay that exists between the contributions of cold and hot plasmas in balancing magnetic stresses. Pressure gradient and anisotropy effects appear to dominate ring current generation in the inner and middle regions, as at Earth, whereas corotational stresses dominate in the outer regions, as was once thought to be true at Jupiter. We will now have the opportunity of

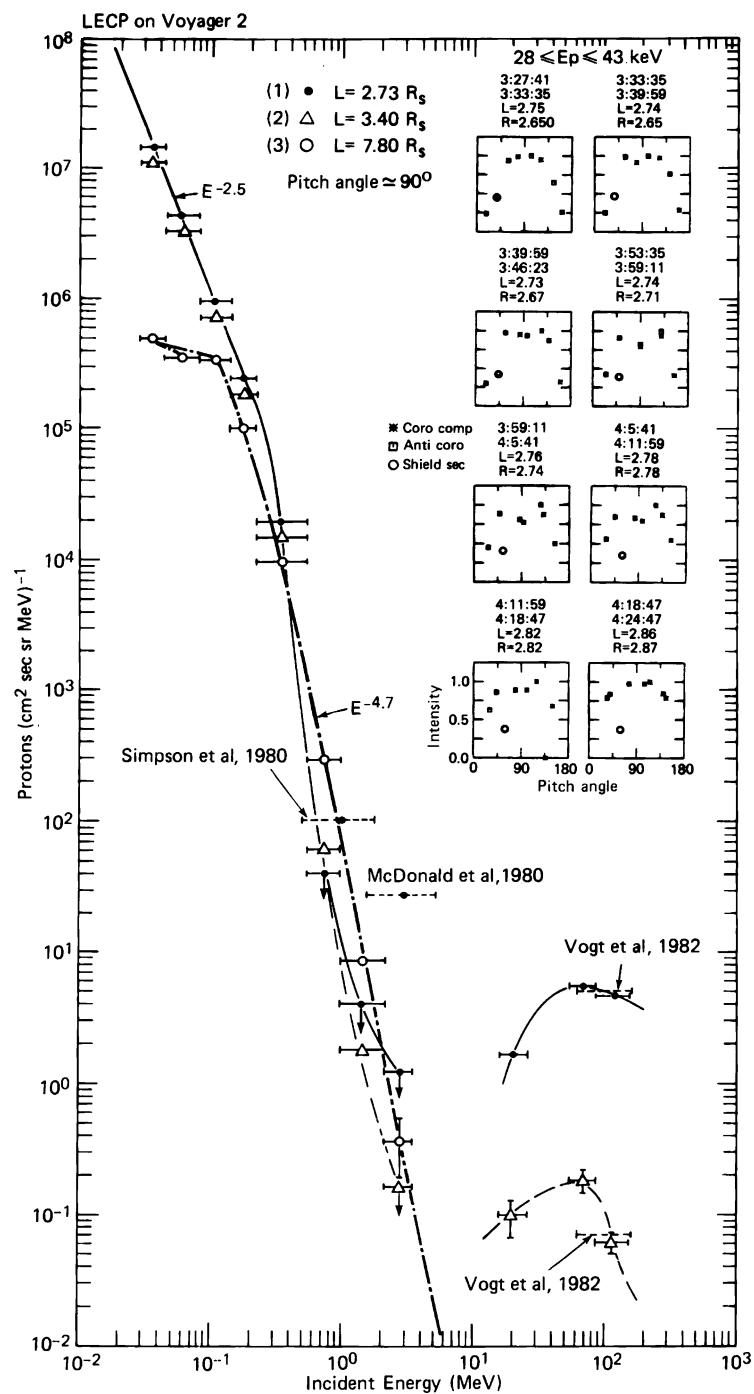


Figure 9. Spectra and pitch angle distributions of energetic ions measured in Saturn's inner magnetosphere by Voyager 2 and comparison with Pioneer-11. After Krimigis and Armstrong (1982).

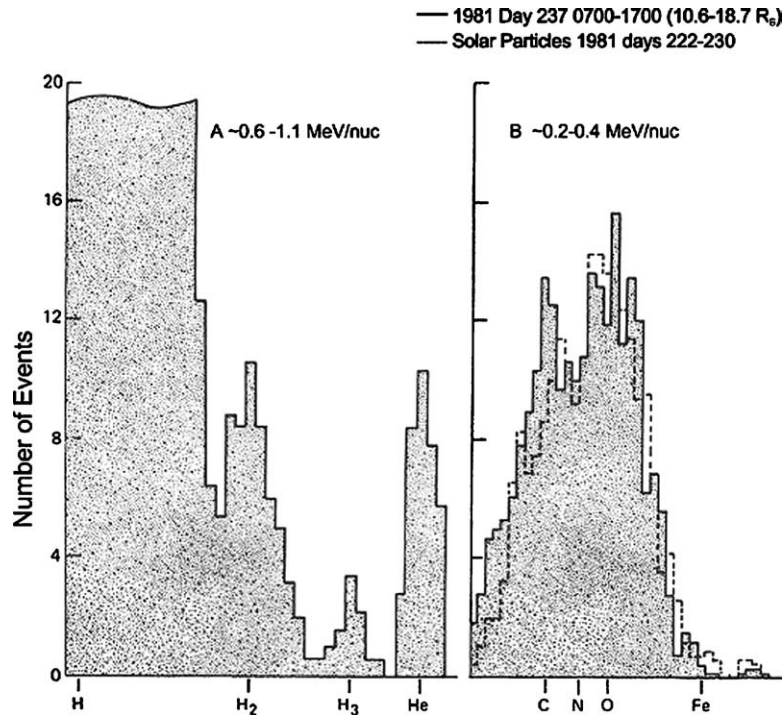


Figure 10. Composition distribution of energetic ions measured by Voyager 2 in Saturn's middle magnetosphere. After Krimigis *et al.* (1982b).

obtaining information about stress balance at Saturn that will tell us a great deal about how such balance is achieved in planetary magnetospheres in general. These same measurement limitations (composition, angular information) have also resulted in very wide uncertainties in our knowledge of radial transport rates of energetic particles at Saturn (Paonessa and Cheng, 1986). Phase space density analyses of the energetic particle populations, in the context of radial diffusion theory (Schulz and Lanzerotti, 1974), should constrain the radial transport and loss rates to a much higher precision than previously available once accurate charged particle invariant parameters are established (with improved angular coverage and resolution) and once the compositional state of the energetic particles can also be established.

#### 2.4. TITAN INTERACTIONS

Titan's nitrogen-rich atmosphere is subject to direct magnetospheric interaction due to its lack of a significant intrinsic magnetic field. To some extent, the dynamical process will be similar to the solar wind interaction with Mars or comets, with the major difference that no bow shock will form because the local value of the magnetosonic Mach number is less than one. The Voyager 1 plasma measurements at Titan flyby showed that a well-defined magnetotail was formed in the wake

region (Ness *et al.*, 1982). However, a four-lobe configuration can also be deduced from both the magnetometer and plasma wave observations (Ness *et al.*, 1982; Gurnett *et al.*, 1982; Neubauer, 1992). This unique phenomenon is caused by the finite gyroradius effect of the exospheric ions created in the vicinity of Titan. This also suggests that Titan's exospheric and ionospheric structures should be highly asymmetric because of the preferential sputtering of the pickup ions on the hemisphere opposite to Saturn. The immediate consequence for the MIMI instrument is that such exospheric structures could be revealed by the ENA images in detail (see Amsif *et al.*, 1997). (We expect a more extensive structure of Titan's exosphere on the anti-Saturn side because of the reimpact effect of the pickup ions.) The MIMI experiment can also be used to study the possible occurrence of particle acceleration in the magnetotail of Titan.

On a global scale, the injection of nitrogen and carbon ions from Titan's exosphere into the Saturnian magnetosphere also provides an ideal set of tracer particles to follow the transport process of energetic ions. The possible detection of molecular ions such as  $\text{CH}_3^+$ ,  $\text{CH}_5^+$ , and  $\text{H}_2\text{CN}^+$  created in Titan's ionosphere (Ip, 1990) could also be used to diagnose time-dependent mechanisms since their life-times are limited by electron dissociative recombination.

As indicated, the very weak or nonexistent intrinsic magnetic field of Titan gives the Kronian magnetospheric plasma direct access to the upper Titan atmosphere, where a variety of complex phenomena take place (Eviatar, 1992; Ip, 1992). Energetic ions in the magnetosphere occasionally will undergo a charge-exchange collision with cold neutral atoms from the upper Titan atmosphere, giving rise to the production of ENAs. The energy of the incident ions is almost entirely transferred to the charge-exchange-produced ENAs, which then propagate along nearly rectilinear ballistic trajectories. The coexistence of energetic ions and cold tenuous gas in the Saturn/Titan system thus makes this system particularly suitable for magnetospheric imaging via ENAs (Cheng and Krimigis, 1989b; Curtis and Hsieh, 1989).

The first simulated ENA images of the Saturn/Titan system are due to Hsieh and Curtis (1988), who modelled the Titan torus around Saturn. Later, Roelof and Williams (1990) included Titan itself, and further examples were presented by Cheng *et al.* (1993). ENAs emitted from the Saturn magnetosphere were detected (without imaging) by the LECP instrument onboard Voyager 1, which was designed to detect mainly charged particles, so there was no system to reject the ions (Kirsch *et al.*, 1981a; Cheng, 1986). The observations were made during periods when Voyager 1 was on open field lines, where there were no significant ion fluxes. The emission was modeled by Hsieh and Curtis (1988).

Amsif *et al.* (1997) presented a study of the energetic neutral atom production, resulting from the interaction of Titan's exosphere with Saturn's magnetosphere. This necessitated the development of a model for the altitude density profile and composition of both the inner and the outer exosphere of Titan. They used a Chamberlain model for the inner exosphere (altitude  $< 6000$  km), for particles with ballistic and escaping orbits, and included the five major species: H,  $\text{H}_2$ , N,  $\text{N}_2$ , and  $\text{CH}_4$ . The

exospheric density and composition altitude profiles obtained from this model were then used in order to calculate the fluxes and the energy spectra of the ENAs produced in the “inner exosphere” of Titan, considering a proton spectrum measured by Voyager in the Saturnian magnetosphere as the parent ion population (Krimigis *et al.*, 1983). The results show how the exospheric species contribute in a different way, as a function of altitude, to the ENA flux spectra. For look directions that go from the Cassini orbiter almost all the way down to the exobase, the contribution to ENA production comes mostly from charge exchanges with  $\text{CH}_4$  and  $\text{N}_2$ . This not only is due to the high integral column density of these molecules, but also is mainly the result of their high charge-exchange cross sections.  $\text{H}_2$  has also high integral column densities, but its lower charge-exchange cross sections significantly reduce its contribution to the ENA fluxes. This sensitivity of ENA production to the composition of the neutral atmosphere means that the ENA directional fluxes and spectra, which MIMI will measure, will constitute a powerful diagnostic tool for evaluating the abundance of the different species in the layers of the Titan exosphere. The calculated spectra of the ENAs are also much softer than the spectrum of the parent energetic ion population. This is due to the filter effect of the charge-exchange cross sections, which decreases the efficiency of ENA production at high energies.

In the outer exosphere (altitude  $> 6000$  km), molecular hydrogen is the dominant species, and a Chamberlain model that included  $\text{H}_2$  particles with ballistic, satellite, and escaping orbits was utilized to evaluate the altitude density profile. This permits an estimate of the ENA intensities several Titan radii from the moon and was used to simulate a flyby of Titan, from 1 day before closest approach to 1 day after, just as will occur about 40 times during the Cassini orbiter tour. Figure 11 (Amsif *et al.*, 1997), shows such a simulated flyby for the 24 h following Titan closest approach. Times are given in hours (H) or minutes (M). The images in each panel are Mercator projections of the entire sky as viewed from the Cassini spacecraft. ENA intensity is shown in the left panels, and equivalent neutral hydrogen column density in the right panels. Near Titan, the molecular  $\text{H}_2$  densities were treated as atomic H densities of twice the value. The coordinate system is Sun–Saturn–ecliptic, with the azimuth angle plotted horizontally (in values decreasing from approximately  $360^\circ$  on the left of the panel to  $0^\circ$  on the right, both  $0$  and  $360^\circ$  being the sunward viewing direction), and the elevation angle plotted vertically (increasing upwards from  $-90^\circ$  to  $+90^\circ$  relative to Saturn). Coordinate labels are suppressed because of the small size of each panel. A logarithmic color bar has been used, covering a range from the maximum value to  $1/100$  of that value, for both the ENA unidirectional intensity  $j_{\text{ENA}}$  (left panels) and column density  $h$  (right panels). The maximum values for each panel are given in dimensionless units scaled for convenience so that the maxima from the numerical computation would be of order unity. The Titan exosphere is nearly as bright in ENA as the inner magnetosphere of Saturn, making it possible to image the exosphere out to at least five Titan radii, and even to resolve it when the spacecraft is several Saturn radii distant from the moon.

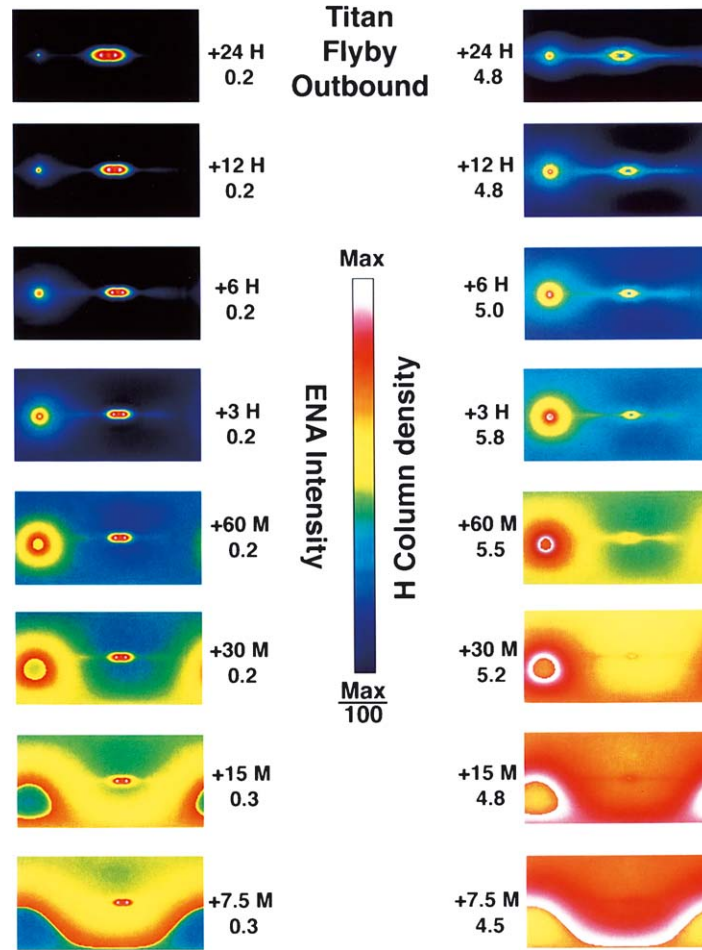


*Figure 11.* ENA intensity (left panels) and equivalent neutral hydrogen column density (right panels) for a simulated outbound Titan flyby of Cassini orbiter. Where hydrogen is molecular (Titan exosphere), density is  $2[\text{H}_2]$ . Mercator projections of the entire sky ( $-90$  to  $+90^\circ$  in elevation centered on Saturn, and  $360^\circ$  in Saturn equatorial azimuth, centered for each panel so as to include both Saturn and Titan). Bold numbers are times relative to closest approach (M = minutes, H = hours). Logarithmic color bar (factor of 100) normalized to brightest pixel in each panel. Maximum values in each panel given as dimensionless numbers. Multiply dimensionless column densities by  $1.2 \times 10^{13} \text{ cm}^{-2}$  (cf. Amsif *et al.*, 1997). Distant Saturn magnetosphere (brightest points are ring current at  $L \cong 3$ ) is comparable in ENA brightness to Titan exosphere, while Titan hydrogen torus (idealized) is much weaker. Note ENA image of Titan exosphere is distinct from Saturn magnetosphere (except within an hour of closest approach).

In Figure 11 it is assumed that the energetic ion population in the vicinity of Titan is uniform and that its pitch angle distribution is isotropic. Well away from the moon these simplifications are the most justifiable. Near Titan, however, and possibly in the vicinity of its wake, finite Larmor radius effects will be important. As

an example, a 20 keV proton in a 5 nT magnetic field, as was measured by Voyager near Titan (Neubauer, 1992), has a  $\sim 4000$  km gyroradius. This is comparable to the Titan exobase radius, which is about 4175 km. Some dark areas in the ENA images are thus expected, in the one side of Titan, due to the screening effect from Titan and its lower atmosphere. In order to simulate these effects, a 3-D model of the interaction of Titan's exosphere with Saturn's magnetosphere has been developed (Amsif, 1996; Dandouras and Amsif, 1999). This necessitated 3-D trajectory tracing techniques for each ion. The results are shown in Figure 12, where a Titan flyby image sequence is simulated, for selected altitude values. Limb brightening effects above the Titan exobase are very clear in these images, and are due to the integrated optical depth in an optically tenuous medium, at certain grazing angles. The other salient feature is shadow effects in the ENA images of the Titan exosphere, which as explained above are due to the finite gyroradii of the parent ion population and the screening effect of Titan. These shadows depend on the ENA energy, on the relative geometry of Titan, and on the magnetic field and the location of the Cassini spacecraft. The INCA images will thus allow remote sensing, not only of the ion fluxes and spectra, but also of the magnetic field in the Titan vicinity. The magnetospheric imaging technique via energetic neutral atom detection is thus a powerful diagnostic tool for the interaction of Saturn's magnetosphere with Titan.

Typical ENA fluxes over Titan are generally of the order of  $200\text{--}3000 \text{ cm}^{-2} \cdot \text{s}^{-1} \cdot \text{sr}^{-1}$ . By taking into account the geometrical factor of the INCA ENA imager, which is  $\sim 2.4 \text{ cm}^2 \cdot \text{sr}$  for the full  $90^\circ \times 120^\circ$  field of view, and considering  $32 \times 32$  pixel images with 86-s exposure (high time resolution images), we get on the order of 40–600 counts/pixel in the 10–50 keV energy range. This corresponds to Poisson uncertainties in the 4–15% range (at  $1\sigma$ ), showing the capabilities for performing magnetospheric imaging studies of the Titan–Saturn interaction with good resolution.

Note that the spacecraft velocity effects on this type of imaging are minimal. For a typical Titan flyby, the Cassini relative velocity is  $\sim 5.9$  km/s, which corresponds to a  $\sim 507$  km interval along the spacecraft trajectory during the 86 s exposure. If we take as an example a 2781-km minimum altitude flyby, the spacecraft altitude evolves from 5000 to  $\sim 4640$  km, which corresponds to an evolution of the angle  $\varphi$ , for the exobase, from  $33.5$  to  $35.4^\circ$ . The resulting  $\Delta\varphi = 1.9^\circ$  is smaller than the  $2.8^\circ$  pixel resolution of the ENA images in the high time resolution images ( $90^\circ \times 120^\circ$  field of view).

## 2.5. AUXILIARY SCIENCE: JUPITER AND INTERPLANETARY PARTICLE ENVIRONMENT

### 2.5.1. *MIMI Measurements at Jupiter*

In December 2000, the Cassini spacecraft obtained a gravity assist from Jupiter as it heads toward Saturn. It encountered the Jovian system with a closest approach distance of  $\sim 139R_J$  at  $\sim 1600$  local time (LT). Several aspects of the Cassini

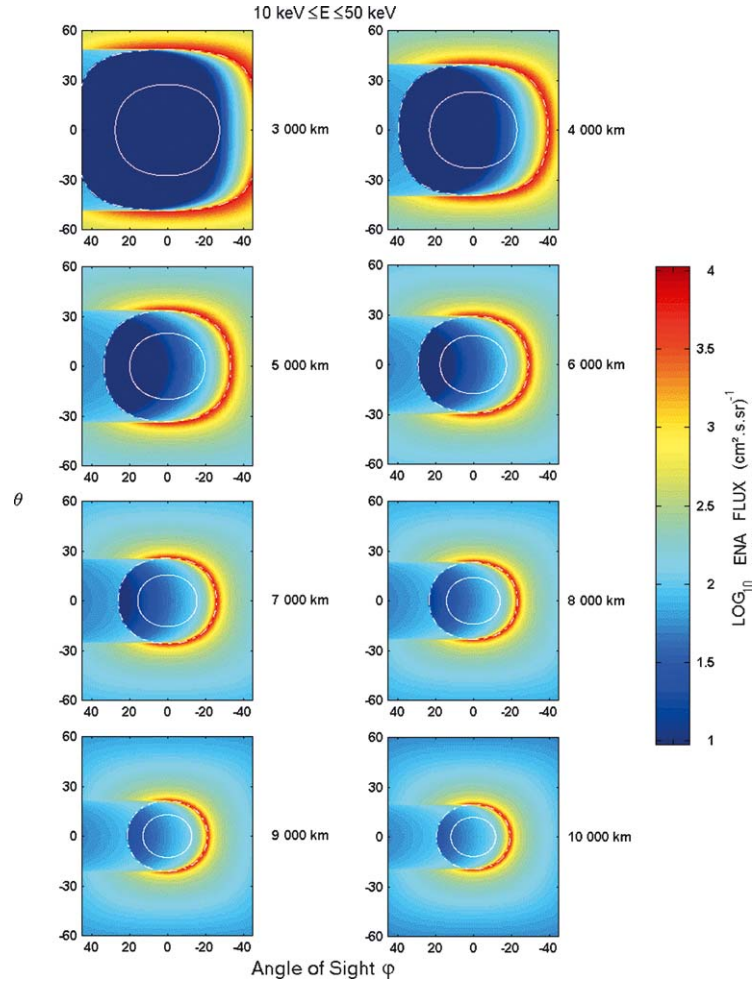


Figure 12. ENA flux as a function of the azimuth view angle  $\phi$  and the elevation view angle  $\theta$ , for eight altitude values of the Cassini orbiter above the Titan surface, ranging from 3000 to 10,000 km. The ENA energy range is 10–50 keV, and the images correspond to the INCA field of view ( $90^\circ \times 120^\circ$ ). The continuous white circle represents the Titan surface, and the dashed white circle represents the Titan exobase. (Dandouras and Amsif, 1999).

encounter with Jupiter have made it possible to address key science questions about Jupiter's space environment that other missions, including Galileo, have not been able to address as effectively or at all. Among these aspects are the unique capabilities of the MIMI instrument. In particular, at Jupiter the MIMI instrument has (Krimigis *et al.*, 2002):

- (1) Provided the first global magnetospheric images of Jupiter using the ENA imaging capabilities of INCA head. The ability of MIMI to obtain high-quality



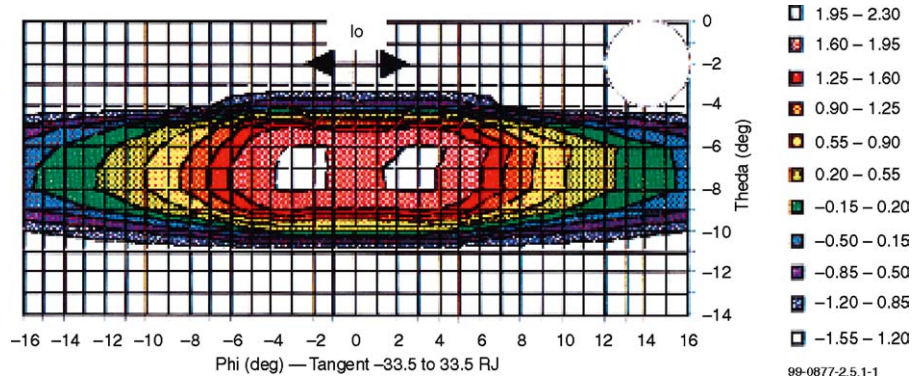


Figure 13. Simulation of an ENA (hydrogen) image of Jupiter's magnetosphere as it would appear to the MIMI/INCA head from  $139R_J$  and  $5^\circ$  magnetic latitude. Color is coded according to the log 10 of counts of 60–120 keV H atoms as observed within  $4^\circ$  angular pixels for a 3-h accumulation. Deconvolution would result in a much thinner (more pancake) structure. The circle shows angular resolution capabilities of INCA after deconvolution.

images of Jupiter's inner and middle magnetosphere ( $r < 30R_J$ ) during Cassini's gravity-assist flyby was documented by Mauk *et al.* (1998). A simulated raw image of Jupiter as it would be viewed by INCA from a distance of  $\sim 139R_J$  is shown in Figure 13. The color is coded according to log 10 of the counts received in 3 h. Approximately 160 of these images have been obtained over a 20-day period, even while Cassini's main communications antenna remained pointed toward the Earth. The images will be sorted and summed according to the variations in systems drivers, including solar wind variations, Jupiter's rotation, the orbital position of Io, etc. The circle shows the anticipated resolution of the INCA measurements after deconvolution procedures have been applied. We expect to separately characterize the regions planetward of  $\sim 10R_J$ , the transition region between dipolar and magnetodisc configurations ( $10\text{--}20R_J$ ), and the magnetodisc regions out to beyond  $\sim 30R_J$ . This analysis is currently in progress.

- (2) Provided the first measurement of the relative concentrations of singly to multiply charged energetic heavy ions using the Cassini MIMI/CHEMS head. The Ulysses SWICS instrument made the first measurements of energetic ion charge states in Jupiter's magnetosphere (Geiss *et al.*, 1992), but was unable to uniquely identify singly charged oxygen and was essentially blind to singly charged sulfur (Geiss *et al.*, 1992). MIMI/CHEMS is the first instrument at Jupiter capable of making this discrimination. More sensitive than the SWICS instrument by a factor of  $\sim 30$ , CHEMS has been able to sense the charge state distributions of the outer magnetospheric regions remotely by characterizing the charge state distributions of pickup ions (PUIs) and other upstream ion events. These events are common in the upstream solar wind regions near Jupiter and are heavily

laden with heavy ions from Jupiter's outer magnetospheric regions and the Io torus (Zwickl *et al.*, 1981; Krimigis *et al.*, 1985; Barbosa and Eviatar, 1986).

With these capabilities the Cassini MIMI instrument will play a critical role in addressing several outstanding questions regarding the Jovian system including:

- (a) *What is the influence of the interplanetary environment, relative to other drivers, on the structure and dynamics of Jupiter's magnetosphere and what are the mechanisms by which such influence is exercised?*

The dynamics of Jupiter's magnetosphere are driven predominantly by planetary rotation (Gehrels, 1976; Dessler, 1983). However, the Jovian magnetosphere is much more dynamic than might be anticipated in a system controlled largely by "rock-steady" planetary rotation, and there is increasing evidence that the interaction with the interplanetary medium can exercise an important influence on magnetospheric processes (Desch and Barrow, 1984; Barrow and Desch, 1989; Reiner *et al.*, 1993; Kaiser, 1993; Prangé *et al.*, 1993; Schneider and Trauger, 1995; Baron *et al.*, 1996; Clarke *et al.*, 1996; Satoh *et al.*, 1996; Mauk *et al.*, 1999). The MIMI/INCA head has obtained ENA images that could illuminate the dynamics of Jupiter's inner and middle magnetosphere while other instruments (dual technique magnetometer (MAG), Cassini plasma spectrometer (CAPS)) are monitoring the conditions of the interplanetary environment. These images may discriminate structures that are influenced by interplanetary conditions from those that are not.

- (b) *How are hot plasmas transported and energized to generate and support Jupiter's unique magnetodisc configuration?*

It is now known that the magnetodisc is predominantly supported by pressures and pressure anisotropies in the sparse, hot plasma components (Mauk and Krimigis, 1987; Paranicas *et al.*, 1991). We do not know how these hot plasmas are energized and transported, and therefore we cannot begin to understand how these populations are able to form the magnetodisc configuration. According to the "neutral wind" model, corotating Io torus ions are neutralized by charge exchange, reionized in the middle and outer magnetosphere by photoionization, energized by pickup and other processes, and then transported back towards the planet by global radial diffusion processes (Eviatar *et al.*, 1976; Barbosa *et al.*, 1984). Alternatively, Io torus plasmas may be transported outward as a cold component by plasma processes, energized, and then transported inward as a hot component. The charge state of the hot heavy ions provided by the MIMI/CHEMS head, and the angular distribution together with the energy spectral shape provided by MIMI/LEMMS, yield a unique finger-print of the neutral wind model, because according to this model, singly charged ions would be very strongly favored when compared with the charge states measured in the Io torus (Belcher, 1983). Once the transport mechanism is established, researchers can then address mechanisms of magnetodisc formation.

Additionally, the Cassini spacecraft has been the first spacecraft to visit the dusk flanks of the Jovian magnetosphere near the equatorial plane, complementing Ulysses' high-latitude pass. This unique opportunity allows for the completion of the "exploration" of Jupiter's broad magnetospheric region. Of particular interest are the indications of solar wind and boundary layer flow, and the associated draping of the magnetic field configuration inside the dusk flank magnetosphere, as a signature of the strength of interactions between the solar wind flow environment and the corotating magnetospheric plasmas (Cheng and Krimigis, 1989a). Observations of detached Jovian plasmas may provide signatures of the plasma shedding processes in the outer Jovian magnetosphere.

### 2.5.2. Pickup Ions

Before arriving at Saturn, the Cassini spacecraft will spend half a solar cycle in interplanetary space, providing a unique opportunity to study in detail a variety of interplanetary particle populations and acceleration processes. MIMI/CHEMS with its large geometry factor and its ability to measure charge states and resolve ion species (e.g., N from O), will provide detailed information on the variations of these populations with radial distance and solar activity. Of particular interest will be (a) interstellar pickup ions (and the low energy portions of the anomalous component); (b) ion acceleration, especially at high-Mach number shocks and in corotating interaction regions (CIRs); and (c) bow shock processes upstream of Saturn and Jupiter (including leakage of energetic ions from the magnetospheres of these planets).

The presence of pickup ions in the inner solar system ( $\sim 1\text{--}5$  AU) is now well established (e.g., Gloeckler *et al.*, 1993; Geiss *et al.*, 1994, 1995; Gloeckler, 1996; Mall *et al.*, 1998; Gloeckler and Geiss, 1998). Investigation of the characteristics of this important heliospheric ion population has already revealed fundamental information about the acceleration of these suprathermal ions (Gloeckler *et al.*, 1994; Fisk *et al.*, 1997), as well as properties of our local interstellar cloud (Gloeckler and Geiss, 1996, 1998; Gloeckler *et al.*, 1997) that could not otherwise be obtained.

The Cassini orbit and the excellent capabilities of CHEMS will make it feasible to gain new information on pickup ions and to measure pickup Ar for the first time. With continuing pickup ion measurements at 1 AU on ACE and from  $\sim 1.5$  to  $\sim 5.5$  AU on Ulysses, together with the recent results from Voyager 1 (Krimigis *et al.*, 2000), the Cassini MIMI observations are essential for providing us with a good global, 3-D view of the spatial distribution of neutrals in the heliosphere. Examples of some of the anticipated results are described below.

**2.5.2.1. Composition of the Interstellar Cloud.** Because the density of pickup ions (except for He) increases almost exponentially with increasing distance from the Sun, Cassini MIMI measurements at  $\sim 10$  AU with a more sensitive instrument (CHEMS) than those on Ulysses and ACE will give us the most precise information on the composition of pickup ions. In Figure 14 the pickup  $\text{O}^+$  spectrum

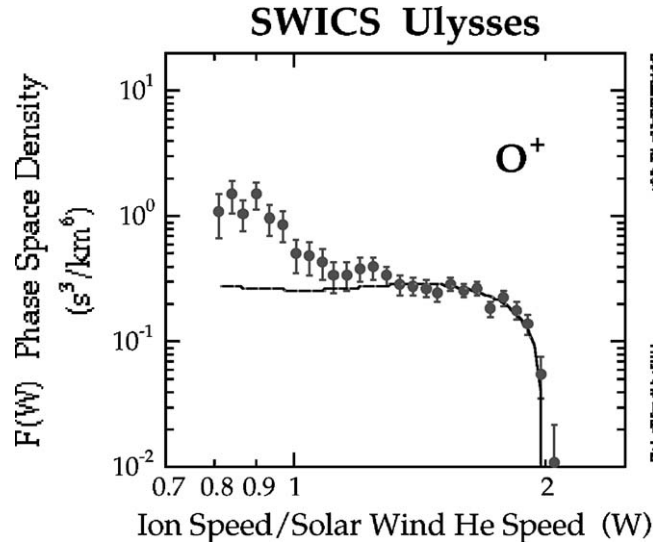


Figure 14. Ulysses SWICS observations of the phase-space density of  $O^+$  averaged over 135 days from 17 February to 1 July 1992. The average solar wind speed was relatively steady at  $442 \pm 36$  km/s and the distance from the Sun remained close to 5.4 AU during the entire time period of these observations. The curve is the model calculation of interstellar pickup  $O^+$ . While the agreement between the model and data is excellent above  $W$  of about 1.3, a significant amount of  $O^+$  from another source is evident below  $W \sim 1.2$ . Adapted from Figure 10 of Gloeckler and Geiss (1998).

obtained with Ulysses at  $\sim 5$  AU is shown. The data used were averaged over a 5-month period in order to reveal the spectral shape in sufficient detail to identify both the interstellar and inner source for oxygen. With CHEMS at 10 AU the statistical accuracy of pickup ion measurements will improve by about a factor of 10. This will lead directly to establishing accurate elemental (and in some cases isotopic) abundances in the local interstellar cloud surrounding our solar system, information of considerable importance for models of stellar evolution. It will also provide powerful constraints on acceleration models for anomalous cosmic rays.

**2.5.2.2. Ionization Rates of the Neutral Gas.** Analysis of the distribution functions of pickup ions measured by CHEMS over a range of heliocentric distances ( $\sim 3$ –10 AU) combined with similar measurements by SWICS on Ulysses, will give us our best determination of ionization loss rates of the various interstellar neutral species (e.g., H, N, O, Ne) inside the heliosphere. Knowledge of these ionization rates is essential for deriving accurate interstellar abundances.

**2.5.2.3. Temperature of the Interstellar Gas.** Measurements of the spatial variations of pickup ions with Cassini MIMI as its orbit crosses the so-called gravitational focusing cone (e.g., Holzer, 1977) gives us the only chance to determine

the temperature of several atomic species (e.g., O, N, Ne) in the local interstellar cloud. Combining this with knowledge of the atomic He temperature (Witte *et al.*, 1996) will give clues to how this warm cloud is heated.

### 2.5.3. *Upstream Particle Events:*

#### *Bow Shock Processes and Magnetospheric Leakage*

Cassini will spend most of its first 15 orbits upstream of the Saturnian bow shock. MIMI/INCA with its large geometry factor in the ion mode is ideal for studies of upstream ion activity, originally observed by Voyagers 1 and 2 (Krimigis *et al.*, 1983; Krimigis, 1986) out to  $\sim 200R_S$ . The early Cassini apoapses lie in the dawn sector, where the spiral interplanetary magnetic field is most likely to connect to the bow shock. Substantial upstream particle activity is therefore expected and will be detected by MIMI/LEMMS. During the Voyager 2 flyby, upstream ion bursts were present at least half the time (Krimigis *et al.*, 1985).

At a planetary bow shock, solar wind ions are reflected into the upstream region. Theories of first-order Fermi acceleration (e.g., Lee, 1982) suggest that such ions should act as a seed population for diffusive acceleration by ion-generated irregularities upstream of the bow shock. Cassini measurements offer the opportunity to perform extensive tests of this model at a planetary bow shock with higher Mach number and much larger dimensions than at Earth. The acceleration region upstream of Saturn is at least ten times larger, so that the cutoff energy in the spectrum should be substantially larger than the  $\sim 200$  keV/e calculated for the case of Earth. MIMI is ideally suited for making the required measurements of energy spectrum, composition, and anisotropy to test diffusive shock acceleration models.

Another source for upstream particle events is leakage of energetic magnetospheric ions (and electrons) into the interplanetary medium. Observations at Earth, Jupiter, Saturn, and Uranus have been interpreted as favoring this hypothesis (Krimigis, 1986, 1992). MIMI/INCA and MIMI/CHEMS will measure ion composition and charge state down to  $\sim 7$  keV/nuc and  $\sim 3$  keV/e, respectively, unambiguously separating accelerated solar wind ions (high charge states) from ions of magnetospheric origin (low charge states). MIMI/LEMMS will measure the anisotropy of these events at energies above 30 keV.

### 2.5.4. *MIMI/INCA Remote Sensing of Heliospheric Shocks*

ENAs are produced whenever energetic singly charged ions undergo charge-exchange (electron capture) collisions with a background population of neutral atoms. These conditions occur not only within planetary magnetospheres, but also in the interplanetary medium throughout the heliosphere. The neutral atoms therein are those of the interstellar gas that flows through the heliosphere and thereby generate the pickup ions, discussed in Section 2.5.2. Those ionization processes systematically diminish the density of interstellar neutrals in the inner heliosphere. For hydrogen, the dominant atom, the attenuation is the most severe, setting in at  $\sim 3$  AU and reducing the H atom intensity to  $\sim 95\%$  of the interstellar value

by 1 AU. The energetic, singly charged ions, again predominantly hydrogen, are protons accelerated by processes associated with the formation and propagation of heliospheric shocks.

Three types of shocks can accelerate protons to energies  $>10$  keV and thus be imaged in ENA by MIMI/INCA: (1) the forward and reverse shocks produced by corotating interaction regions (CIRs); (2) the driven shocks associated with large solar flare ejecta and coronal mass ejections (CMEs); and (3) the termination shock (TS) of the heliosphere itself, where the supersonic solar wind makes a transition to the subsonic interstellar plasma. Roelof (1992) estimated the ENA intensities  $>10$  keV as they would be viewed by Cassini at Saturn for the first two types of interplanetary shocks, while Hsieh *et al.* (1992b) provided estimates from 1 AU. A topic of concern in both studies was whether the ENA emission from interplanetary shocks of either type would obscure the ENA emission from the heliospheric termination shock. Hsieh *et al.* (1992a) had proposed that ENA would be produced at the TS by low-energy anomalous cosmic-ray protons that are eventually accelerated to  $\sim 100$  MeV. Hilchenbach *et al.* (1998) claimed to have identified ENA hydrogen at 55–80 keV coming from the anti-apex direction using the CELIAS/HSTOF ion telescope on the SOHO spacecraft during solar minimum conditions.

While the construction of ENA global images of the energetic proton population associated with the heliospheric termination shock is an exciting possibility for MIMI/INCA, the imaging of interplanetary shocks is practically expected. Based on the Voyagers 1 and 2 measurements of differential proton intensities  $j_{\text{ion}}$  for  $E > 35$  keV, Roelof (1992) estimated the global distribution of ENA hydrogen intensities as they would be viewed from 10 AU (Saturn orbit) from the general relation

$$j_{\text{ENA}} = \sigma \int ds n_{\text{H}} j_{\text{ion}}.$$

Using Voyager proton spectra representative of the peak values at the shock  $j_0$ , ( $E$ ) the integral intensity (above an energy  $E$ ) can be written as

$$J_{\text{ENA}} = \int dE j_{\text{ENA}} = n_0 I \int dE \sigma_{16} j_0,$$

where the integral over the spatial dependence of  $n_{\text{H}}$  and  $j_{\text{ion}}$  is

$$I = (1.5 \times 10^{-3} \text{ cm}) \int (ds/a) (n_{\text{H}}/n_0) (j_{\text{ion}}/j_0).$$

Here  $\sigma_{16}$  is the charge-exchange cross section in units of  $10^{-16} \text{ cm}^2$ ,  $a = 1 \text{ AU}$ , and  $n \cong 00.1 \text{ cm}^{-3}$  is H atom density in the interstellar medium.

Values of the Voyager peak intensity spectra (normalized to 10 AU) and the integral  $\int dE \sigma_{16} j_0$  are compiled in Table II, while Figure 15 presents the spatial dependence of  $I$  as “fish-eye” ENA images of the sunward hemisphere (as viewed

TABLE II  
Integral ENA energy coefficient derived from Voyager energetic ions.

$E$ (keV)	10	20	40	70	100	200	400
$\sigma_{16}$ (cm <sup>2</sup> )	7.75	4.45	1.67	0.377	0.101	6.09(3)	1.76(4)
$j_{\text{ion}}$ (cm <sup>2</sup> sr s keV) <sup>-1</sup>	[0.70]	[0.55]	0.35	0.20	0.125	0.036	0.010
$dE s_{16} j_{\text{ion}}$ (sr s) <sup>-1</sup>	[71.6]	[34.6]	8.81	1.36	0.31	9(3)	1(4)

Ion fluxes in [brackets] are extrapolated downward in energy from 35 keV.

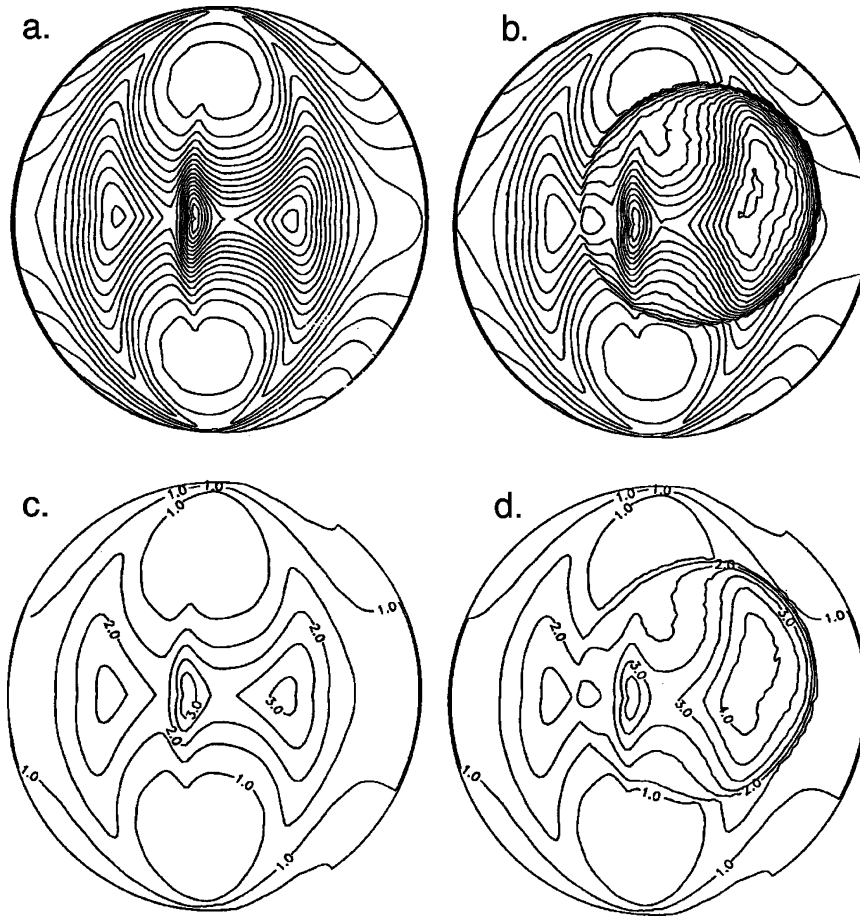


Figure 15. Sunward hemisphere views from Saturn (10 AU) of simulated ENA images of interplanetary shock-associated energetic protons from (a) forward and reverse shocks bounding a corotating interaction region (CIR) and (b) solar transient shock superimposed upon a CIR. ENA flux contours are labeled in (c) and (d) in units of  $100I$ , as defined in the text, and may be converted into ENA hydrogen flux (as a function of energy) using the values given in Table II.

from Saturn). The ENA images of a large CIR are shown in the left-hand panels, while a large driven shock has been superimposed upon the CIR in the right-hand panels. Contours with  $2^\circ \times 2^\circ$  are shown in the upper panels, while a subset of contours of the quantity  $100I$  are drawn in the lower panels. The antisunward hemispheres (not shown) exhibit very low contrast, with contours only between 0.5 and 1.0. Based on the instrument response characteristics of MIMI/INCA, Roelof (1992) estimated that images like those shown could be accumulated (in Cassini roll mode) in 3 days with  $\sim 10\%$  counting statistics in  $6^\circ \times 6^\circ$  pixels. These statistics were deemed adequate for interpreting the image in terms of global topology, particularly in the portions of the image where the contrast is strongest (at the edge of the shock structure). It was also concluded, in agreement with Hsieh *et al.* (1992b), that only the largest CIR or transient solar shocks would obscure the ENA emission from protons associated with the global heliospheric shock.

### 3. Description of Instrumentation

The MIMI instrument consists of one set of electronics servicing three detector heads which perform a broad variety of measurements. Figure 16 shows the mechanical configuration of the instrument on Cassini with each of the major

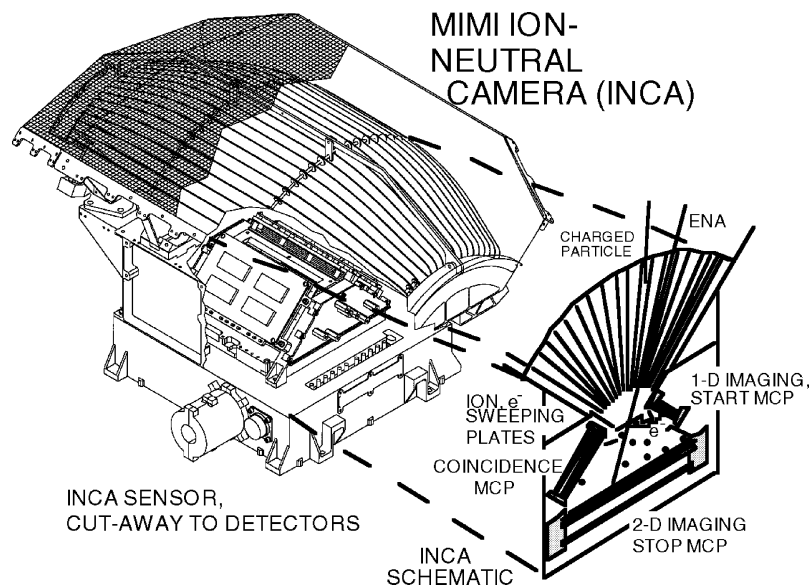


Figure 16. Perspective drawing of the INCA head, with section schematic. Serrated charged collimator plates sweep charged particles out of aperture. ENAs penetrate front foil covering entrance slit, producing secondary electrons for start pulse and 1-D position. ENA travels to back foil and 2-D imaging microchannel plate (MCP), and back-scattered secondary electrons provide coincidence pulse. Dots indicate the locations of wire electrodes for secondary electron steering.



subsystems detailed. The electronics box contains the data processing unit (DPU), as well as all the digital processing electronics for all three detector heads (LEMMS, CHEMS, and INCA). The LEMMS head is double-ended, with oppositely directed 15 and 30° (full angle) conical fields of view (FOV). LEMMS is mounted on a rotation platform, with the spin axis parallel with the spacecraft  $y$ -axis, such that when rotating, the LEMMS telescopes sweep through 360° in the spacecraft  $x$ - $z$  plane. The CHEMS head sits on the particles and fields instrument pallet, with a field of view of  $\sim 160^\circ$  in latitude (bisected by the spacecraft  $x$ - $y$  plane) by 4° in azimuth centered on the spacecraft  $x$ -axis. CHEMS measures the charge state and composition of ions from  $\sim 3$  to 220 keV/e, comprising the most energetically important portion of the Saturnian magnetospheric plasma. The INCA head is separately mounted and nearly co-aligned with the remote sensing instruments, with a field of view  $\sim 120^\circ$  in latitude by 90° in azimuth, centered on a vector rotated 9.5° toward the spacecraft  $+x$ -axis from the  $-y$ -axis. INCA makes two different types of measurements. It obtains the directional distribution, energy spectra, and crude composition of magnetospheric ions between  $\sim 7$  keV/nuc and  $\sim 3$  MeV/nuc; and it makes remote images of the global distribution of the energetic neutral emission of hot plasmas in the Saturnian magnetosphere, measuring the composition and energy spectra of those energetic neutrals for each image pixel. When the spacecraft is rotating, the MIMI sensors obtain measurements over  $\sim 4\pi$ . The different MIMI sensors share common electronics and provide complementary measurements of energetic plasma distribution, composition, and energy spectrum, and the interaction of that plasma with the extended atmosphere and moons of Saturn.

### 3.1. THE INCA SENSOR

INCA is a large ( $\epsilon G \sim 2.4 \text{ cm}^2 \text{ sr}$ ; where  $G$  is the geometric geometry factor, and is the efficiency) time-of-flight (TOF) detector that analyzes separately the composition and direction of motion of the incident energetic neutral atom. Elements of the detector assembly can be seen in Figure 16. Sensor characteristics are summarized in Table III. The entrance includes a serrated-plate fan for charged particle deflection, with an FOV of 90° in the nominal ( $z$ -axis) spin direction (the azimuthal direction) by 120° in the direction perpendicular to the spin plane (elevation), centered on the spin plane. The calculated angular response in the 120° direction, including efficiencies is shown in Figure 17.

#### 3.1.1. Deflector

The magnesium deflector plates are serrated to inhibit forward scattering of incident particles. Commandable potentials of up to  $\pm 6$  kV are applied to alternate plates to sweep energetic charged particles with energies  $\leq 500$  keV/e into the plate walls (excluding them from the detector). The shielding effectiveness of the collimator has been measured in the laboratory (Figure 18; also Mitchell *et al.*, 1996) and is

TABLE III  
INCA sensor characteristics.

Energetic neutral atoms or ions, chosen by command	
Energy range	<7 keV to 3 MeV/nuc
Velocity resolution	50 km/s (1 ns TOF)
Mass resolution	H, O, Heavies
Field of view	$120^\circ \times 90^\circ$
Angular coverage	$0.7\pi$ sr ( $\pi$ , if spinning)
Angular resolution	$\sim 8^\circ \times 4^\circ$ , $E_H > 50$ keV
(scattering in foils at low $E$ )	$> 8^\circ \times > 8^\circ$ , $E_H \sim 20$ keV
Time resolution	6 s, PHA events
	85 s, low resolution
	6 min, high resolution
	23 min, full sky
$G \times \varepsilon$ ( $\text{cm}^2$ sr)	$\sim 2.4$ for O, $\sim 0.6$ for H
$G \times \varepsilon$ for $4^\circ \times 4^\circ$ pixel (O)	0.007, tapered at edges
Dynamic range	$\sim 10^7$

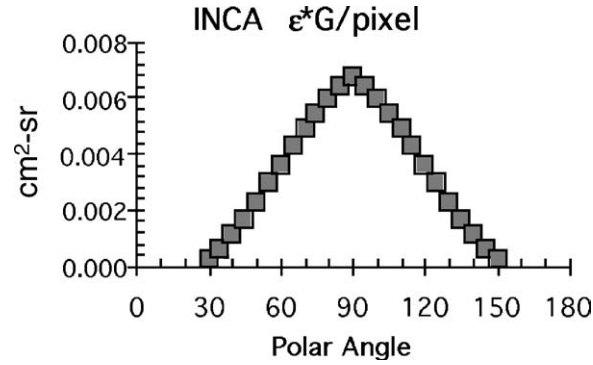


Figure 17. INCA polar angle response function,  $\varepsilon^*G/\text{pixel}$  (oxygen).

adequate to permit neutral particle imaging below the sweeping energy even while the instrument is within moderate magnetospheric plasma environments.

### 3.1.2. Measurement Technique

Incoming neutral particles encounter and penetrate a thin foil, producing secondary electrons (Figure 16). The secondary electrons are first accelerated perpendicular to the foil by the E-field which is locally normal to the equipotential surface of the foil, and then steered electrostatically (using a combination of wires and shaped electrodes at fixed potentials) onto a side, start microchannel plate (MCP) with 1-D

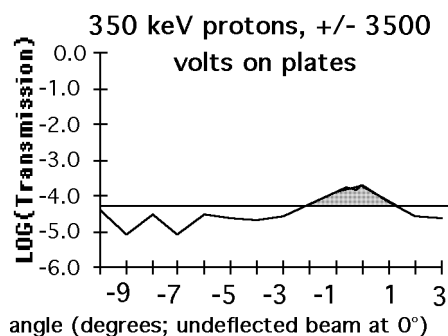


Figure 18. Accelerator test of deflector ion sweeping at an intermediate voltage, indicating charged particle rejection at better than four orders of magnitude. The peak with shading is in the position of the undeflected beam, and results from energetic neutrals created via charge exchange of energetic ions in the Van deGraff beam tube.

position sensitive anode. A start time taken from a capacitively coupled electrode of the start MCP is generated by this event. The original incident particle, after some angular scattering in the front foil, continues through the instrument, striking a second foil just in front of the stop MCP assembly. Secondary electrons produced on the exit surface of the imaging foil are accelerated into the stop MCP and 2-D imaging anode, mapping the position of impact and registering the stop time for the TOF measurement. Figure 19 presents the basic geometry used to determine the ENA trajectory through the sensor. In addition to this TOF and trajectory measurement, secondary electrons produced as the ENA enters the back foil are electrostatically accelerated and guided to the side coincidence MCP (see Figure 16). The electron travel time for these back-scattered electrons is constrained to  $<40$  ns by the steering potentials. The pulse generated in the coincidence plate is used in the valid

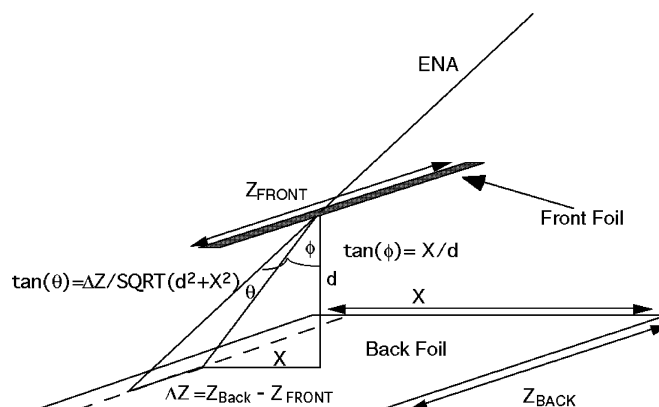


Figure 19. INCA imaging geometry.

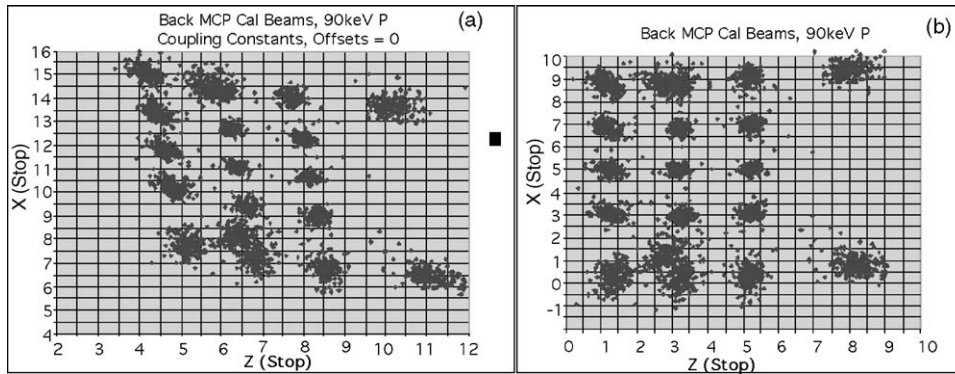


Figure 20. (a) INCA back microchannel plate (MCP) positions (including scattering in front foil) for 90 keV protons, before correction for interelement capacitance. (b) Same data as in (a), with capacitive coupling correction factors applied. Pattern reflects beam positions faithfully.

event logic circuitry as a coincidence check on the measurement, further reducing the probability that uncorrelated background will be falsely counted as a neutral.

The position-sensitive anodes used to register the front foil and back foil positions use proportional charge deposition on shaped elements (wedges and strips) to yield position. Because these elements are in very close physical proximity, there is considerable capacitive coupling between them. The resulting image is skewed, as shown in Figure 20.

### 3.1.3. Mass Determination

The number of secondary electrons produced in each foil is dependent on the atomic number of the neutral atom; for the two most common neutral atoms expected, oxygen has been found to produce several times the number of secondaries that hydrogen will produce. Exploiting this phenomenon, we record the pulse-height of the MCP signal and determine the species based on that measurement (Table IV).

As shown in Figure 21 and Table V (which is based on data shown in Figure 21, as well as higher energy data similar to that in Figures 21 and 22), MCP pulse-height is sufficient to discriminate hydrogen from oxygen. Since hydrogen is expected to

TABLE IV

Algorithm for mass determination based on MCP pulse-height, using the inequality  $\text{IF}[(\text{PH}_{\text{BACK}}) \cdot \text{GT} \cdot (B - A \times \text{PH}_{\text{FRONT}})] \text{ THEN } \Rightarrow \text{SPECIES} = \text{Oxygen}.$

Energy/nucleon (keV/nuc)	$B$	$A$	H counted as O (%)	O counted as H (%)
31	16,000	4	0.2	17.08
46	19,000	4	0.2	5.34
80	19,000	4	0.2	?

TABLE V  
INCA calibration resolution results.

keV/nuc	$s_\theta$ H ( $^\circ$ )	$s_\phi$ H ( $^\circ$ )	$s_\theta$ O ( $^\circ$ )	$s_\phi$ O ( $^\circ$ )
5	11.6	15.1	7.1	4.6
20	6.75	6.5		
31	5.25	3.5	2.9	1.7
46	3.2 <sup>a</sup>	2.6 <sup>a</sup>	2.0	1.8
80	3.9 <sup>a</sup>	1.8 <sup>a</sup>	2.8	1.4
90	4.8	2.2		
200	4.2	1.3		

<sup>a</sup>Large pulse-height events only.

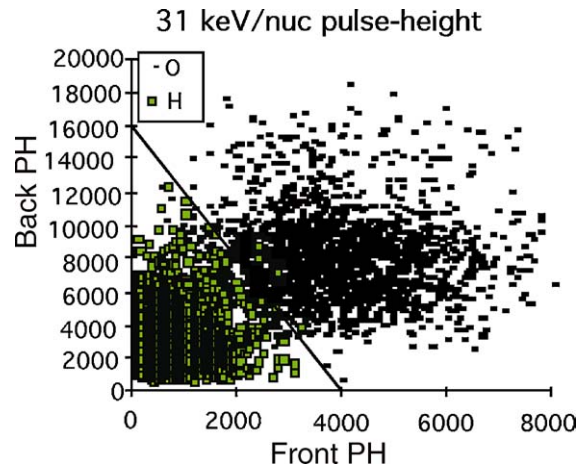


Figure 21. Separation of oxygen and hydrogen using MCP pulse-height signatures. 31 keV/nuc O and H measurements, overplotted. The hydrogen separates as lower MCP pulse-heights. At higher energies, this separation becomes more complete.

dominate the low pulse-height data, the fraction of O mistakenly identified as H is not considered significant. The measured positions of the penetration of the foils determine the particle arrival direction and its path length within the instrument; the TOF associated with this path length (and thus velocity) combined with the species determination based on pulse-height analysis determine particle energy. Although the species are not well resolved, the neutral fluxes at Saturn are expected to consist almost exclusively of hydrogen and oxygen, and these will be relatively well determined.

#### 3.1.4. Foils and UV Sensitivity

Electrons are also produced in the foils by photoionization by extreme and far ultraviolet light (EUV and FUV), predominantly in the Ly- $\alpha$  line at Saturn. The

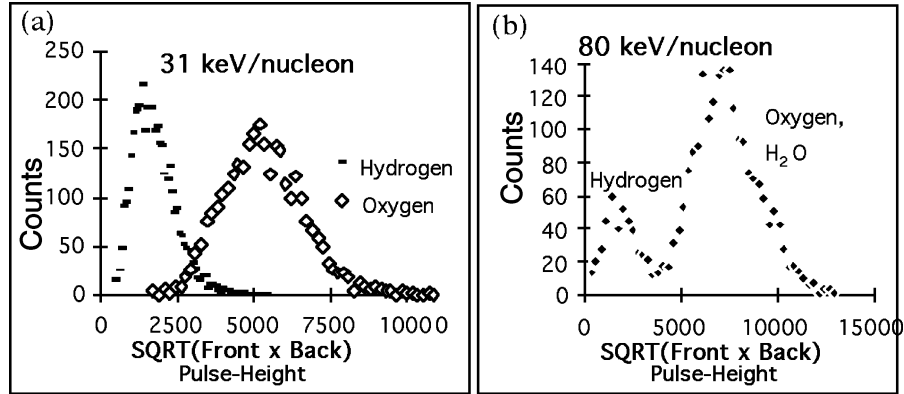


Figure 22. (a) Data shown in Figure 21, re-cast as square root of front pulse-height back pulse-height, showing the separation between hydrogen and oxygen. (b) Same format, for a run at 80 keV/nuc, in which the dominant constituent was water. Some molecules broke up in the beam tube, resulting in a mix of hydrogen and oxygen in the same beam with the same velocity. The separation by pulse-height is clear.

chosen foil must therefore be thick enough to attenuate the Ly- $\alpha$  to an acceptable level, so that the position and TOF circuitry is not swamped by false counts. The TOF measurement is made by recording a start signal followed by a stop signal some time later. Any single photon can produce a start or a stop, but not both. As long as the time between a false Ly- $\alpha$  start and a separate false Ly- $\alpha$  stop is long compared with the maximum valid TOF period ( $\sim 100$  ns), this background will not produce false events. The electronic design assumes nominal upper limits for Ly- $\alpha$  start events of  $\leq 5 \times 10^4$  secondary electrons/s, and for stop events of  $\leq 1000$  secondary electrons/s. The peak Ly- $\alpha$  flux at Saturn (excluding the Sun itself) is  $\sim 1$  kR (Broadfoot *et al.*, 1981), which corresponds to  $\sim 6 \times 10^8$  photons/s incident on the front foil (which has a geometry factor of  $\sim 7$  cm<sup>2</sup> sr). The secondary electron production efficiency for Ly- $\alpha$  photons is  $\sim 1\%$  (Hsieh *et al.*, 1980). The INCA foil comprises 5.5 mg cm<sup>-2</sup> Si, 3.6 mg cm<sup>-2</sup> Lexan, and 1.0 mg cm<sup>-2</sup> C with a measured  $5.0 \times 10^{-3}$  Ly- $\alpha$  transmittance to reach a conservative design goal of  $\leq 3 \times 10^4$  Ly- $\alpha$  induced secondary electrons/s when the brightest portion of the Saturnian atmosphere/exosphere is in view. The choice of Si and C for the foil was based on the work of Hsieh *et al.* (1991). This foil is mounted on a 70 line/inch nickel mesh (82% transmission). The stop foil, composed of Lexan and carbon, will reduce the Ly- $\alpha$  flux to the back, 2-D imaging MCP by about another factor of 100. With the Sun in view at Saturn, because the quantum efficiency for secondary electron production is so high at EUV wavelengths, no practical combination of foil composition and thickness could be identified to sufficiently suppress it. We therefore included a recloseable shutter, designed such that when the Sun is nominally in view, the shutter will reduce the geometry factor enough (by  $\sim 30$  times) to allow operation.

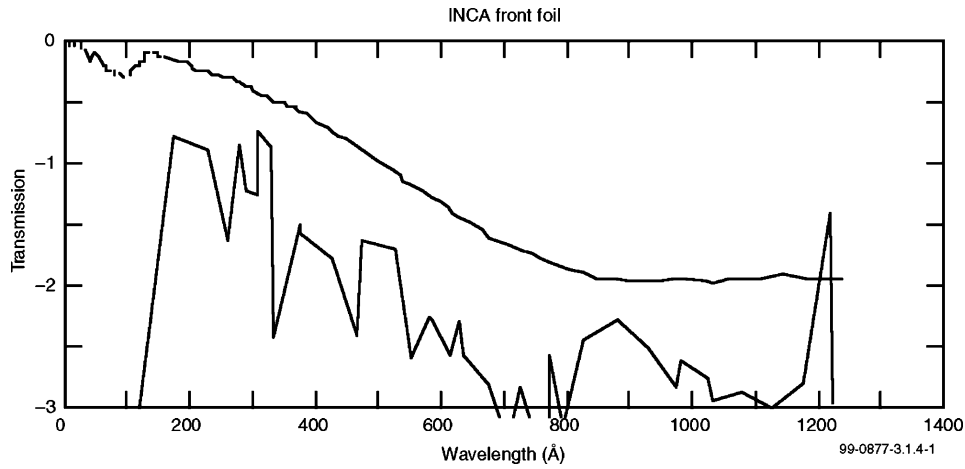


Figure 23. Modeled transmission of INCA front foil as a function of wavelength. Piecewise integrated solar spectrum, after filtering by the foil, is shown in lower curve.

The measured Ly- $\alpha$  front foil transmission, in the lot from which the flight foil was selected, is approximately  $5 \times 10^{-3}$ . The predicted transmission, as a function of wavelength, is shown in Figure 23.

### 3.1.5. Angular Resolution

Angular scattering in the foils, along with the angular spread introduced in the electron optics, has been measured during accelerator tests of the complete engineering model INCA sensor. Representative angular standard deviations are given in Table V.

The  $\phi$  resolution is dominated by scattering in the front foil and the entrance slit width in all cases. The  $\theta$  resolution is dominated by the scattering in the front foil and by the electron optics for the front foil imaging. The latter effect is dominant at higher hydrogen energies, where the number of secondary electrons produced on average is  $\sim 1$ . The position resolution achievable by the start electron optics is modeled in Figure 24.

For the models, data from Meckbach *et al.* (1975) was used to represent the secondary electron energy spectrum. The figure suggests that for single secondary electrons, the spread in the start position will have a full width half maximum (FWHM) of  $\sim 2$ –4 mm. This is consistent with our calibration results for high energy protons. For moderate proton energies, a fraction of the events will produce two or more secondaries; therefore, we will be able to create separate images selected on the basis of start anode pulse height, allowing for higher resolution to be achieved on the two or more secondary events. This has the effect of improving the standard deviations stated above for  $>45$  keV hydrogen by about  $1^\circ$ .

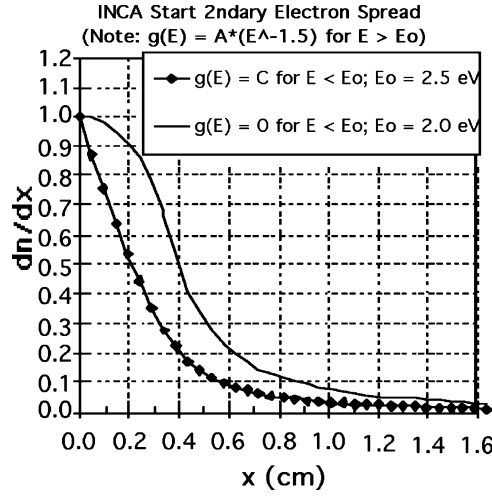


Figure 24. Model start position uncertainty due to random velocities of start secondary electrons. The constant  $C = g$  (2.5 eV).

### 3.1.6. Sensitivity and Background Rejection

The INCA head relies upon valid TOF (separate start and stop) measurements, as well as coincidence pulses to differentiate background from foreground events. EUV will produce secondary electrons, but not correlated start, stop, and coincidence pulses. In order to produce false events that appear valid, an EUV start must be followed by EUV (or other) stop and coincidence pulses. Other sources of false signals may come from high-energy penetrating 2 MeV energetic electrons, which should only become a significant background inside  $L = 5-6$ , as well as ion fluxes above the rejection cutoff energy of the deflection plates. The latter will be discriminated against by their TOF signatures (i.e., too fast to be valid neutrals below the cutoff), although we expect to be able to image neutrals up to  $\sim 6$  MeV when the ambient energetic ion flux above the cutoff energy is sufficiently low. The expected environment will give foreground count rates ranging from  $\sim 10^3 \text{ s}^{-1}$  for the inner Saturnian magnetosphere down to  $\sim 1 \text{ s}^{-1}$  at great distances.

The system has an intrinsic window for valid events of  $\sim 100$  ns, based on the maximum valid TOF for a  $\sim 50$  keV oxygen (which is the slowest valid ENA expected to be analyzed), and the coincidence window is  $\sim 40$  ns. The background rate for false valid events from uncorrelated background rates will therefore be  $\sim 1 \times 10^{-7} \cdot \sim 4 \times 10^{-8} \cdot R_{\text{start}} \cdot R_{\text{stop}} \cdot R_{\text{coincidence}}$ , where  $R_{\text{start}}$  ( $R_{\text{stop}}$ ,  $R_{\text{coincidence}}$ ) is the uncorrelated singles rate due to penetrating background and EUV on the start (stop, coincidence) MCP. Thus, the false valid event rate is  $\sim 4 \times 10^{-15} \cdot R_{\text{start}} \cdot R_{\text{stop}} \cdot R_{\text{coincidence}}$ , assuming the accidental rates are uncorrelated. For the EUV generated background rates expected with the design foil thicknesses, i.e.,  $R_{\text{start}} = R_{\text{coincidence}} = \sim 30,000$  counts/s and  $R_{\text{stop}} = \sim 300$  counts/s



(see discussion in Section 1.3), the maximum false coincidence rate attributable to EUV, will be  $(4.5 \times 10^{-4})$  events/s in regions with low foreground rates. If a penetrator hits both MCPs and produces a correlated pulse pair, the probability of a false coincidence event being registered goes up. However, by requiring a minimum TOF of about 1.5 ns (corresponding to a  $\sim 6$  MeV proton TOF), we will discriminate against some of these very fast particles. Using the coincidence requirements, background rates from penetrators (cosmic rays and magnetospheric energetic particles) combined with uncorrelated EUV, rates are expected to be  $<0.001 \text{ s}^{-1}$  at apoapsis, increasing as Cassini enters the penetrating  $>2$  MeV electron flux in the inner magnetosphere.

Calibrations made with a setup including both a low intensity 50 keV proton beam and a high-intensity UV light source (Figure 25) show that even with an order of magnitude higher UV rates than those expected at Saturn (when the Sun is not in the FOV), the protons can be imaged with a signal-to-noise ratio of between 30 and 100. It should be noted that when MIMI flew past Venus, the accidental rate from the intense UV at Venus was higher by approximately one order of magnitude than would be predicted by the above discussion. While this remains unexplained, the background at Earth from UV was not significant, and the UV background expected at Saturn should be lower than the Earth environment even in the worst case.

Because hydrogen produces only  $\sim 1$  secondary electron, on average, when it strikes a surface (foil, MCP), any given hydrogen atom may not produce any secondaries at a surface. Therefore, many hydrogen atoms are not counted at all, because they do not produce all three pulses required to be registered as valid events (start, stop, and coincidence pulses). For this reason, protons suffer from an additional (energy dependent) efficiency factor of  $\sim 0.2$ – $0.5$ , relative to oxygen, which produces an average of  $\sim 6$ – $8$  electrons at a surface.

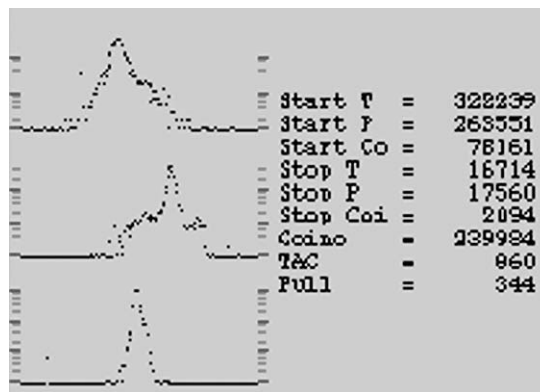


Figure 25. Calibration data for UV rates  $\sim 300,000$  counts/s. The 50 keV protons in the beam can be seen in the position plots (front foil top, back Z position middle, back X position bottom). Rates are displayed to the right.

### 3.1.7. *INCA Analog Processing*

Figure 26 shows a block diagram of the INCA analog processing electronics. The INCA sensor generates an MCP start signal, an MCP stop signal, and MCP position signals. The timing signals will be processed in the time-to-amplitude converter (TAC) circuitry over the range of  $\sim 2$  to  $\sim 100$  ns with total system resolution of  $\sim 1.0$  ns. The TAC processing time through the A/D converter is  $\sim 10 \mu\text{s}$ . Position measurements are derived from the start and stop MCP anode signals. The timing and angle information from a valid event is latched into an event register, where it is stored until the DPU is ready to process it.

### 3.1.8. *INCA High Voltage*

Chevron stacks of two MCPs require high bias voltages extending up to about 3500 V to operate properly. While these voltages are high, very little current is drawn ( $< 60 \mu\text{A}$ ), so power consumption is low. These bias voltages are commandable to adjust the gain of the MCP devices, thus correcting any gain shifts due to aging, burn-in, radiation effects, etc. Secondary electron focusing is accomplished with voltages provided by the same supplies. The INCA sensor contains a total of three MCP high-voltage supplies, one to bias the start MCP, one to bias the coincidence MCP, and the third for the stop MCP. The electron steering elements use voltages provided by these same supplies. INCA also has similar high-voltage supplies to bias the charged particle deflection plates. These supplies are commandable, such that the deflection plate voltages can be varied between a low voltage and about 6 kV.

### 3.1.9. *INCA in-Flight Performance*

The INCA instrument has returned excellent data during the Earth and Jupiter flybys, while its response at Venus was dominated by intense UV interference, as pointed out in Section 3.1.6.

One of the Earth flyby images was obtained while the spacecraft was located at GSE coordinates  $X = -9R_E$ ,  $Y = -3R_E$  and the field-of-view spanning a range from  $\sim 45^\circ$  from the Sun to  $\sim 135^\circ$ , i.e., viewing a substantial part of the ring current from duskward to tailward. The data are shown in Figure 27, projected as detailed in the caption. The resolution is excellent, as is the dynamic range of the instrument, as shown in the lower panel. The upper panel represents a smoothed distribution with the Earth to scale and with proper orientation of the magnetic axis. This image of the partial ring current represents the first obtained by an instrument specifically designed to measure ENAs.

## 3.2. CHARGE-ENERGY-MASS-SPECTROMETER (CHEMS)

The CHEMS instrument will characterize the suprathermal ion populations in the magnetosphere of Saturn and in interplanetary space by measuring the 3-D distribution functions of elemental and molecular ions. CHEMS uses energy

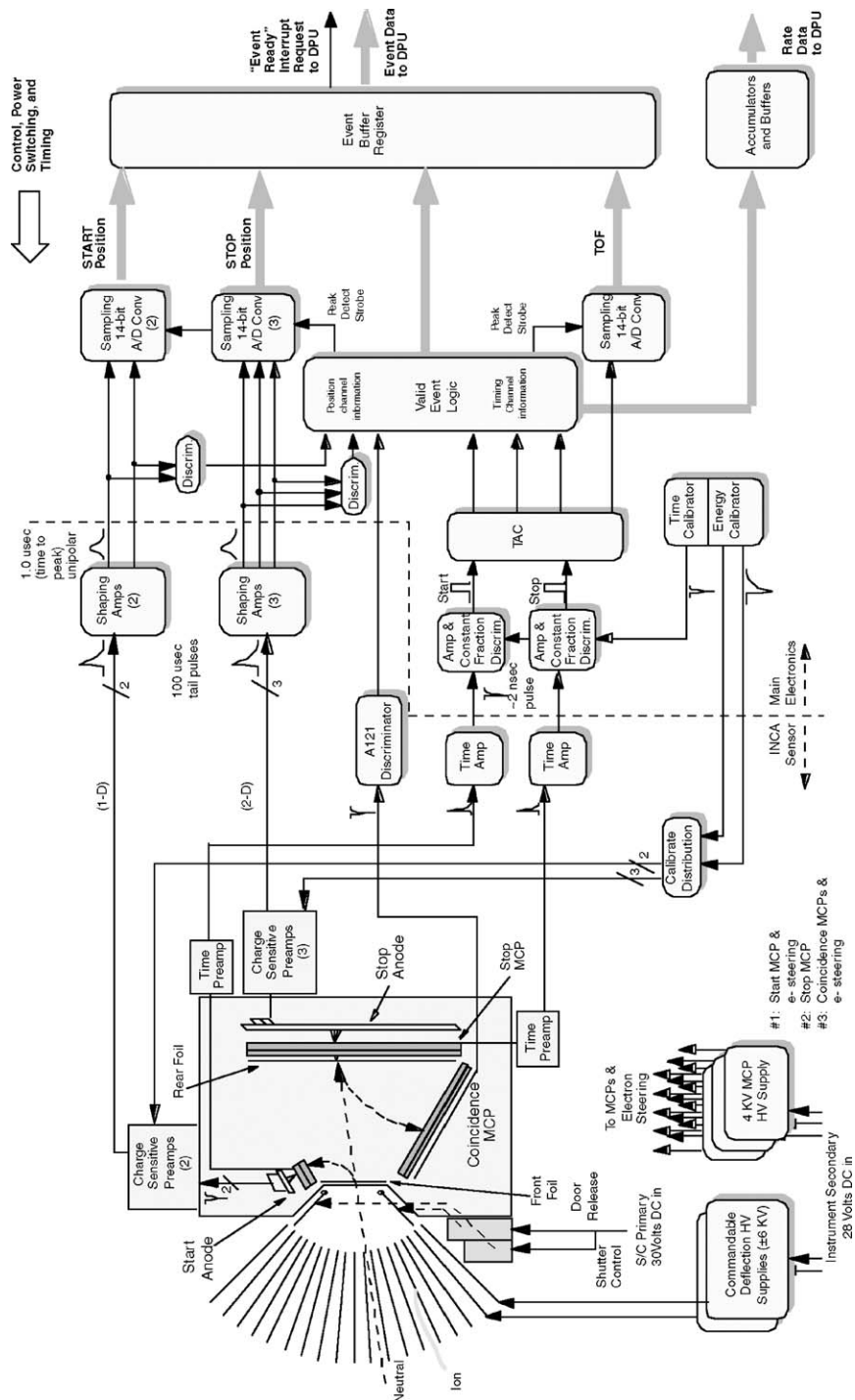
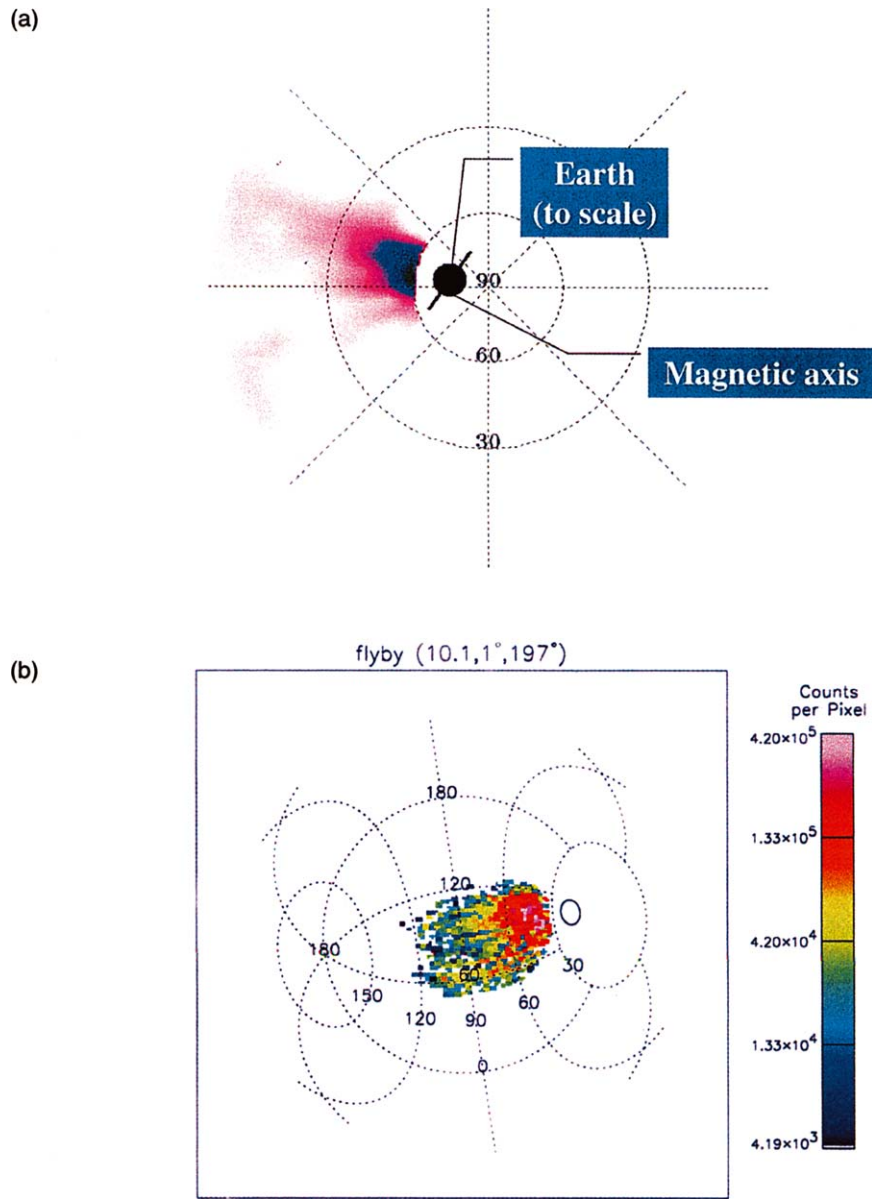


Figure 26. Functional block diagram for INCA.



*Figure 27.* ENA images obtained by the INCA sensor August 18, 1999, 4:17–4:35 UT, during Cassini's Earth flyby. (a) Smoothed INCA image of ring current from time-of-flight channel (27–39 keV, H atoms). Representation is a fish-eye projection centered on the Sun. Cassini is  $10.1R_E$  from the Earth on the night side. Region of the dusk side ring current imaged extends between  $30^\circ$  to beyond  $60^\circ$  from the Sun ( $5 < L < 10$ ). (b) INCA image (every pixel) of the Earth's ring current from time-of-flight channel (27–39 keV, H atoms) represented in instrument coordinates (elevation and azimuth). Cassini vantage point is from a radius of  $10.1R_E$ ,  $1^\circ$  latitude and  $197^\circ$  longitude (GSE).

TABLE VI  
Capabilities of the CHEMS instrument.

Energy per charge range	3–220 keV/e
Ion species	H–Fe
Mass per charge range	1–80 amu/e
Resolution (FWHM)	
Energy per charge, $\Delta(E/Q)/(E/Q)$	0.03
Mass per charge, $\Delta(M/Q)/(M/Q)$	0.08, He <sup>2+</sup> at 100 keV/e 0.07, O <sup>+</sup> at 100 keV
Mass, $\Delta M/M$	0.15, He <sup>2+</sup> at 100 keV/e 0.5, O <sup>+</sup> at 100 keV
Geometrical factor	0.05 cm <sup>2</sup> sr
Field of view (FWHM)	4.0° by 159°
Dynamic range	10 <sup>10</sup>

per charge analysis followed by the TOF versus energy technique to determine both the mass per charge and mass of ions. CHEMS has a relatively large geometrical factor for a charge state-determining instrument. It also has a nearly  $4\pi$  viewing geometry when the spacecraft is rolling, affording the capability of measuring 3-D distribution functions. The CHEMS sensor is very similar to the STICS sensor on the GEOTAIL spacecraft (Williams *et al.*, 1994) and the STICS sensor on the Wind spacecraft (Gloeckler *et al.*, 1995). The capabilities of the CHEMS instrument are summarized in Table VI and a photograph is shown in Figure 28.

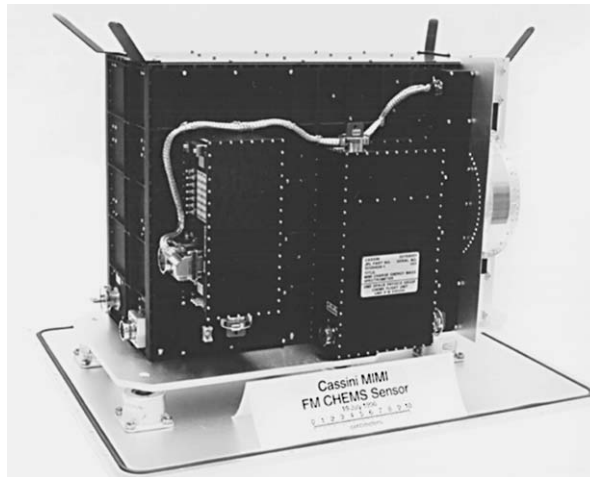


Figure 28. Photograph of the CHEMS instrument.

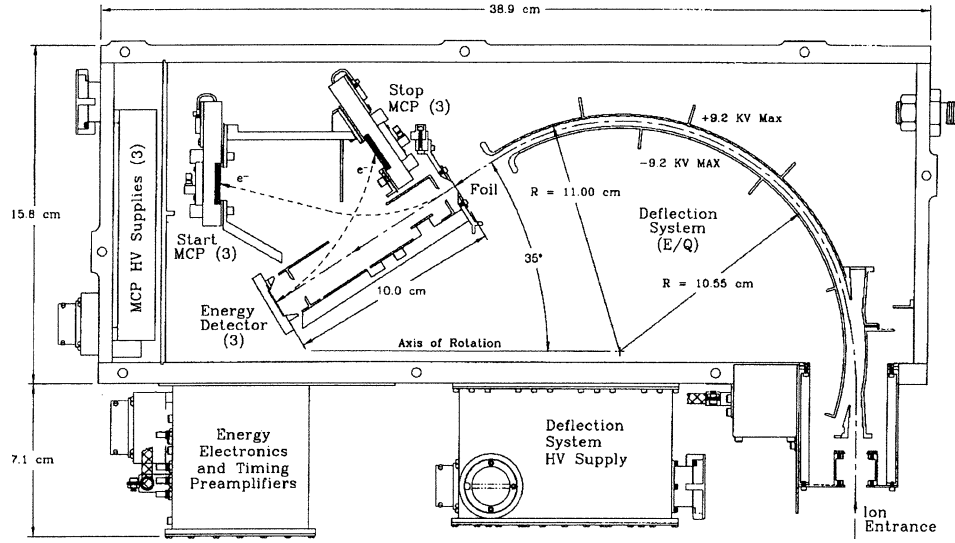


Figure 29. CHEMS mechanical configuration.

### 3.2.1. Principal of Operation of CHEMS

The CHEMS sensor is based on the technique of particle identification using electrostatic deflection combined with TOF and energy measurements (Gloeckler and Hsieh, 1979). The sensor's configuration is shown in Figure 29.

Ions of kinetic energy  $E$ , mass  $M$ , and charge state  $Q$  enter the sensor. The electrostatic deflection analyzer serves both as a UV trap and an energy per charge ( $E/Q$ ) filter, allowing only ions within a small ( $\sim 3\%$ ) energy per charge interval centered on a value determined by the stepped deflection voltage to enter the TOF versus energy system.

In the TOF system the speed of each ion is determined by measuring the travel time  $\tau$  of the particle between the start and stop detectors separated by a distance of 10.0 cm. The particle identification is completed by measuring the residual energy of the ion in an ion-implanted, low-noise, silicon solid-state detector (SSD).

From simultaneous measurements of the time-of-flight,  $\tau$ , and residual energy,  $E_{\text{meas}}$ , and a knowledge of  $E/Q$ , the mass  $M$ , charge state  $Q$ , and incident energy  $E$ , of each ion is determined as follows:

$$\frac{M}{Q} = 2 \left( \frac{\tau}{d} \right)^2 \left( \frac{E'}{Q} \right) \quad Q = \left( \frac{E_{\text{meas}}}{\alpha} \right) \left( \frac{E'}{Q} \right)$$

$$M = 2 \left( \frac{\tau}{d} \right)^2 \left( \frac{E_{\text{meas}}}{\alpha} \right) \quad E = Q \left( \frac{E'}{Q} \right)$$

where  $d$  is the flight path,  $E'/Q$  the ion's energy per charge after the carbon foil, taking into account the small energy loss in the thin foil, and  $\alpha$  gives the ratio of

measured energy in the SSD to kinetic energy incident at the detector, a number less than 1 due to nuclear defect. The reduction in measured energy due to nuclear defect becomes more important at lower energies and for higher masses (Ipavich *et al.*, 1978).

In general the measurements of  $\tau$  and  $E/Q$  are more accurate than that of  $E_{\text{meas}}$  at the energies covered by CHEMS. Therefore the determination of  $M/Q$  is more precise than that of  $M$  or  $Q$  individually. For ions with insufficient energy to trigger the 26 keV SSD electronic threshold, only  $M/Q$  is determined.

### 3.2.2. Description of the CHEMS Instrument

The CHEMS sensor contains a deflection system, three TOF telescopes, each of which includes an SSD for the energy measurement, the high-voltage power supplies for the deflection analyzer system and the MCPs, analog electronics to produce shaped signals from the SSDs, and six preamplifiers for the fast timing signals. The various detector signals are sent to the MIMI Main Electronics Unit for further processing. Basic instrument characteristics are listed in Table VII, and a block diagram of the CHEMS electronics is given in Figure 30.

**3.2.2.1. Deflection Voltage System.** Particles enter the CHEMS electrostatic deflection analyzer system through a simple entrance aperture that includes a light trap. The deflection system consists of two concentric spherical segments. The deflection plate power supply (DPPS) supplies symmetric positive and negative voltages to the outer and inner plates, respectively. The DPPS supplies 32 output voltages up to a maximum of  $\pm 9.225$  kV as listed in Table VIII. The logarithmic spacing of the steps is about 14.9% and the passband is  $\sim 3\%$ . Normally, the DPPS will step through a sequence of 16 steps, consisting of the odd-numbered steps from 31 to 1, but the sequence used is completely commandable. The  $E/Q$  values of the steps are used in the MIMI DPU for the mass per charge classification. The  $E/Q$  values given in Table VIII are derived from the potential differences between the two DPPS outputs measured before launch, multiplied by the nominal analyzer constant of 11.97. Error in the analyzer constant was found to be  $<1\%$  during accelerator calibrations of the sensor.

**3.2.2.2. Time-of-Flight System.** The CHEMS TOF versus energy assembly consists of a start and stop detector separated by 10.0 cm. Particles with the correct energy per charge pass through the deflection system and penetrate the thin ( $\sim 2.5 \mu\text{g}/\text{cm}^2$ ) carbon foil at the entrance of the TOF telescope (see Figure 29). Secondary electrons are emitted from the point where the ion exits the foil. These secondary electrons are deflected by electric fields inside the telescope and strike one of the three start MCPs, generating the start signal for the TOF analysis. At the far end of the TOF telescope, the ion strikes one of the three SSDs. Secondary electrons from the front surface of the SSDs are deflected onto one of three stop MCPs, providing the stop signal for the TOF analysis. The SSDs also provide

TABLE VII  
CHEMS instrument characteristics.

Mass	6.84 kg
Dimensions	22.9 cm × 38.9 cm × 28.0 cm (x, y, z)
Carbon foils	Three segments for each of three telescopes supported on 100 line/inch nickel mesh on a conical frame, 80% transmission Each segment: 6 mm high, 22.85 mm wide Thickness: nominal – 2.0 $\mu\text{g}/\text{cm}^2$ ; measured – 2.5 $\mu\text{g}/\text{cm}^2$
Microchannel plates (MCPs)	Six borderless chevron pairs from Galileo Electro-Optics Corp. (3 Start, 3 Stop) Active area: 15 mm by 37 mm (555 mm <sup>2</sup> each) Pore size: 25 $\mu\text{m}$ Length to diameter ratio: 40
Solid-state detectors (SSDs)	Three specially made, thin window, ion-implanted silicon (PIPS) detectors from Canberra Industries Depletion depth: 300 $\mu\text{m}$ Entrance window: $\sim 30$ nm Si Trapezoidal shape Height: 12.0 mm Width (top): 12.0 mm Width (bottom): 22.2 mm Active area: 206 mm <sup>2</sup>
Electrostatic deflection system	Two concentric spherical segments with opposite polarities Mean radius: 107.75 mm Gap: 4.5 mm Analyzer constant: 11.97 Deflection angle: 125°
TOF measurement	Three independent telescopes; 53° FOV each Flight path: 10.0 cm Minimum TOF: 6 ns Maximum TOF: 523 ns 0.511 ns/channel Nominal shielding: 1.57 g/cm <sup>2</sup> Al
Energy measurement	Electronic threshold: 26 keV Maximum energy: 2455 keV 2.46 keV/channel

energy information on the incident particles if the incident energy is sufficiently high to exceed the electronic threshold of 26 keV.

The three TOF telescopes are independent. Each telescope covers 53° in polar angle as shown in Figure 31. The telescopes have a narrow 4° acceptance in the



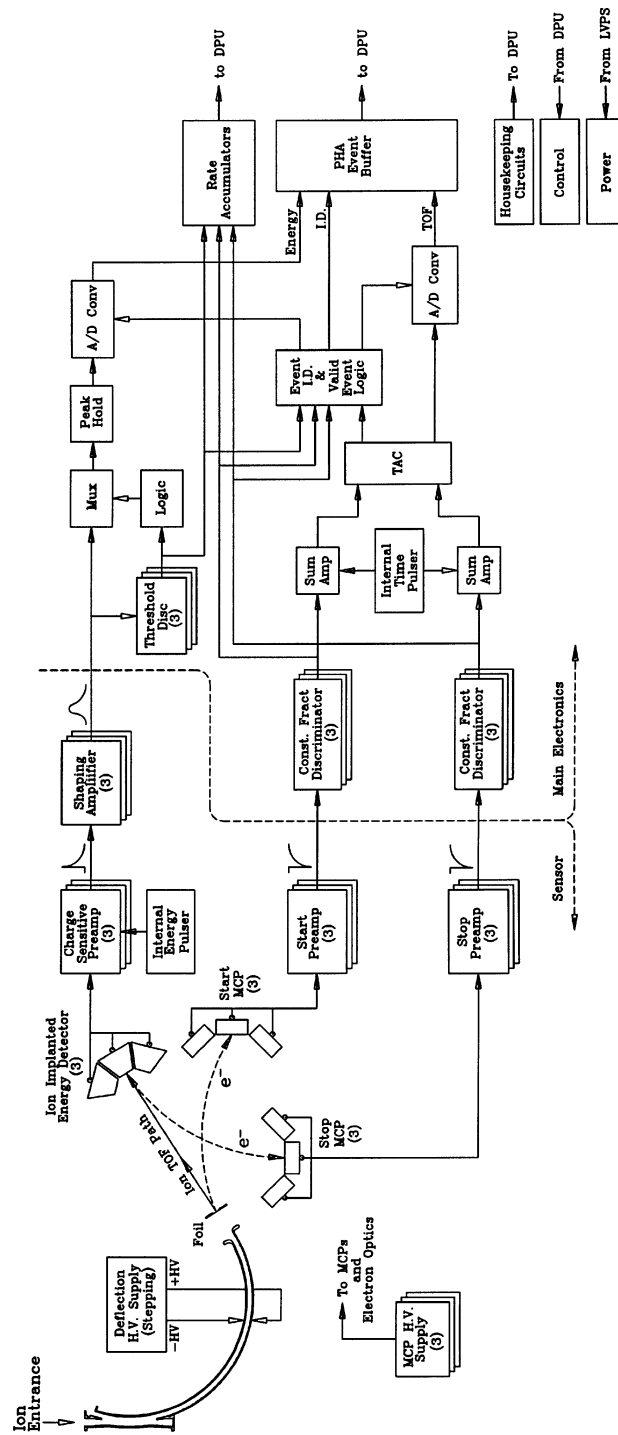


Figure 30. CHEMS analog electronics block diagram.

TABLE VIII  
CHEMS deflection system.

Step no.	Energy per charge (keV/e)	Measured deflection voltage (kV)
0	2.81	0.235
1	3.29	0.275
2	3.78	0.316
3	4.40	0.368
4	5.05	0.422
5	5.86	0.490
6	6.75	0.564
7	7.81	0.653
8	8.92	0.745
9	10.3	0.861
10	11.8	0.984
11	13.6	1.141
12	15.7	1.309
13	18.1	1.509
14	20.8	1.734
15	23.9	1.996
16	27.4	2.290
17	31.5	2.635
18	36.2	3.027
19	41.6	3.48
20	47.8	3.99
21	54.9	4.59
22	63.2	5.28
23	72.6	6.07
24	83.4	6.97
25	95.9	8.01
26	110.1	9.20
27	126.6	10.58
28	145.3	12.14
29	166.9	13.95
30	191.6	16.01
31	220.2	18.40

direction perpendicular to that figure. When the spacecraft rolls about the  $z$ -axis, CHEMS covers most of the unit sphere. Each of the three telescopes has its own microchannel plate power supply (MCPPS), which supplies both the start and stop plates. The secondary electron steering voltages are provided by a diode 'OR' of

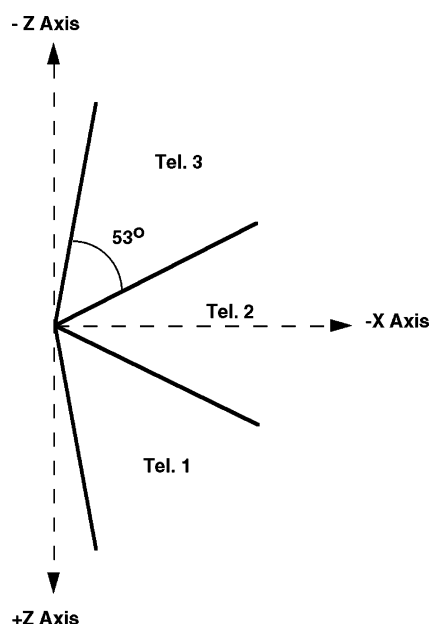


Figure 31. CHEMS telescope view directions relative to the indicated spacecraft axes.

the appropriate outputs of the three supplies. Thus a failure of one MCPPS causes a loss of only one-third of the angular coverage.

Shielding was strategically added in and around the TOF telescopes to reduce the singles counting rates in those portions of Saturn's magnetosphere with high fluxes of relativistic electrons. The MCP housings were made from 1.0-mm tungsten. The cylindrical structure surrounding the TOF region was made from 3.5-mm aluminum. All of the open pockets were removed from the pyramid on which the SSDs are mounted. These measures plus a number of others provide the equivalent of at least 5.8 mm of aluminum ( $1.57 \text{ g/cm}^2$ ) in almost all directions, which will protect the detectors from electrons below 2.5 MeV.

### 3.2.3. CHEMS Data Types

CHEMS returns three types of counting rate data along with pulse-height analysis (PHA) events that give complete information on individual ions. Engineering rates (listed in Table IX) are derived from individual detectors or detector coincidences and are useful in assessing instrument health, in the overall normalization of fluxes in high rate periods, and in assessing the extent of any accidental coincidences or pulse pileup in the SSDs.

The other two types of counting rates and the PHA data use the capability of the DPU to rapidly classify individual ion events as to mass per charge and mass (several thousand per second). PHA events contain complete information on a sampling of the incident ions. A PHA event consists of two 10-bit linear channel

TABLE IX  
CHEMS engineering rates.

	Name	Coincidence requirement	Description
1	START1	None	Start MCP, Telescope 1
2	START2	None	Start MCP, Telescope 2
3	START3	None	Start MCP, Telescope 3
4	STOP1	None	Stop MCP, Telescope 1
5	STOP2	None	Stop MCP, Telescope 2
6	STOP3	None	Stop MCP, Telescope 3
7	ENERGY1	None	Solid-State Detector, Telescope 1
8	ENERGY2	None	Solid-State Detector, Telescope 2
9	ENERGY3	None	Solid-State Detector, Telescope 3
10	DCR1	Double	Start-Stop Coincidence, Tel. 1
11	DCR2	Double	Start-Stop Coincidence, Tel. 2
12	DCR3	Double	Start-Stop Coincidence, Tel. 3
13	TCR1	Triple	Start-Stop-SSD Coincidence, Tel. 1
14	TCR2	Triple	Start-Stop-SSD Coincidence, Tel. 2
15	TCR3	Triple	Start-Stop-SSD Coincidence, Tel. 3
16	UFSR	None	Universal Start MCP, Any Telescope
17	URSR	None	Universal Stop MCP, Any Telescope

TABLE X  
CHEMS pulse height analysis events.

Item	No. of bits
Energy channel number	10
TOF channel number	10
SSD ID	2
Start MCP ID	2
Range ID	3
DPPS step number	5

numbers representing time-of-flight and measured energy in an SSD (Table X), two ID numbers specifying which Start MCP and SSD were triggered, the DPPS step number (equivalent to energy per charge), and a range ID determined by the DPU based on its calculation of mass and mass per charge. For improved accuracy, the DPU uses two-segment linear approximations in the conversion of time and energy channel numbers to physical units.

The seven range IDs are indicated in Figure 32 and Table XI. Each range corresponds to a range of mass per charge and mass as indicated. The DPU calculates

TABLE XI  
CHEMS PHA ranges and basic rates.

Range	Number of rates	Rate FOV (°)	Coincidence requirement	NM (inclusive)	NQ (inclusive)	Mass (amu)	Mass per charge (amu/e)
0	3	53	Double	0–0	1–22	0–0	0.70–1.60
1	3	53	Double	0–0	23–73	0–0	1.60–10.9
2	3	53	Double	0–0	74–126	0–0	10.9–80.0
3	3	53	Triple	1–62	1–22	0.50–95.0	0.70–1.60
4	3	53	Triple	1–32	23–73	0.50–7.50	1.60–10.9
5	3	53	Triple	1–62	74–126	0.50–95.0	10.9–80.0
6	3	53	Triple	33–62	23–73	7.50–95.0	1.60–10.9

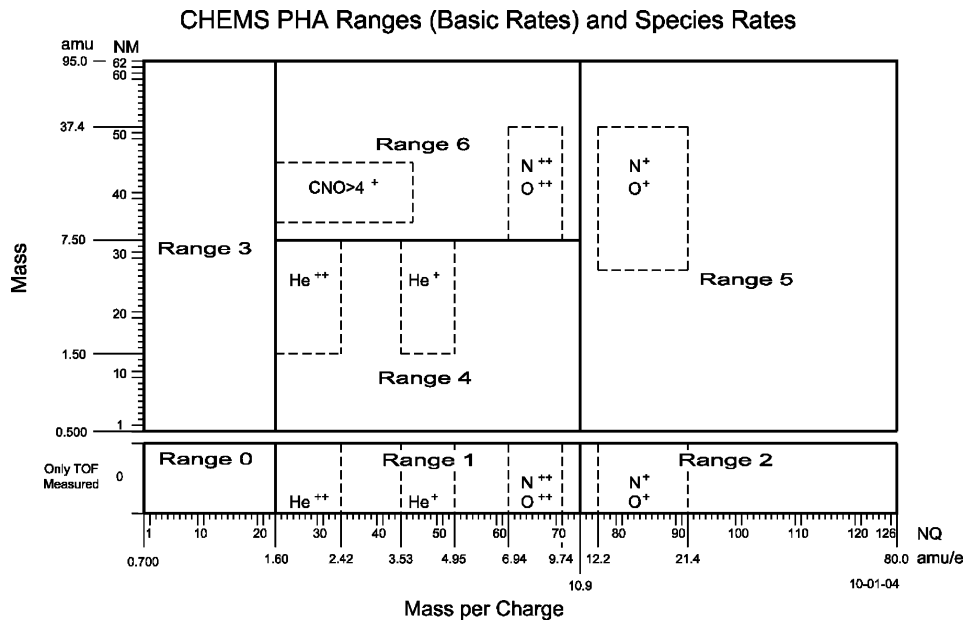


Figure 32. CHEMS PHA ranges, basic rates, and species rates.

two integers,  $NQ$  (1–126) and  $NM$  (0–62), logarithmically related to mass per charge and mass, respectively. Ranges 0–2 correspond to  $NM = 0$ , indicating that there was no SSD trigger, in which case, no mass is determined. Ranges 3–6 correspond to triple coincidences that include an energy measurement as well as a time-of-flight. A basic rate is associated with each range. The basic rates record the total number of events of each range separately for the three TOF telescopes.

There is insufficient telemetry to send down PHA events for all particles, so the DPU selects a random sample of events, giving each range equal weight. Each range

TABLE XII  
CHEMS species rates.

Species	Number of rates	Rate FOV (°)	Coincidence requirement	NM (inclusive)	NQ (inclusive)	Mass (amu)	Mass per charge (amu/e)
He <sup>+</sup>	1	159	Double	0–0	44–52	0–0	3.53–4.95
He <sup>+</sup>	1	159	Triple	14–32	44–52	1.50–7.50	3.53–4.95
He <sup>2+</sup>	1	159	Double	0–0	23–33	0–0	1.60–2.42
He <sup>2+</sup>	1	159	Triple	14–32	23–33	1.50–7.50	1.60–2.42
N <sup>+</sup> , O <sup>+</sup>	3	53	Double	0–0	77–91	0–0	12.2–21.4
N <sup>+</sup> , O <sup>+</sup>	3	53	Triple	28–51	77–91	4.91–37.4	12.2–21.4
N <sup>2+</sup> , O <sup>2+</sup>	1	159	Double	0–0	62–70	0–0	6.94–9.74
N <sup>2+</sup> , O <sup>2+</sup>	1	159	Triple	33–51	62–70	7.50–37.4	6.94–9.74
CNO > 4 <sup>+</sup>	1	159	Triple	36–45	23–45	9.67–22.5	1.60–3.80

purposely contains only double coincidence or triple coincidence events. In high background regions of the Saturnian radiation belts, the double coincidence events will become dominated by accidental coincidences before the triple coincidence events do. By placing the double coincidences in separate ranges, they are never able to displace the more reliable triple coincidences. By command, the PHA events from any range can be excluded from the telemetry.

Nine smaller regions of  $M$  versus  $M/Q$  space are defined, corresponding to species expected to be common in Saturn's magnetosphere. Events falling in those regions are counted by species rates, as listed in Table XII and shown in Figure 32. Only double and triple coincidence O<sup>+</sup> and N<sup>+</sup> events are separately counted for each telescope. There are no species rates dedicated to H<sup>+</sup> since basic rates 0 and 3 will respond almost entirely to H<sup>+</sup>.

### 3.2.4. CHEMS Modes of Operation

CHEMS has relatively few modes. When the Cassini spacecraft is rolling, a complete energy spectrum will be obtained during each 16th of the roll (22.5°) by commanding the CHEMS DPPS through 16 steps. At a nominal roll period of 23 min, CHEMS spends 5.39 s at each energy per charge with 0.150 s after each transition blocked from data accumulation by the DPU to allow the DPPS output voltage to settle. When the spacecraft is not rolling, CHEMS will be commanded through its stepping sequence on a time basis with a similar amount of time spent at each step. There is an in-flight calibrator that can stimulate the CHEMS electronics with timing pulses of known separation (20–300 ns) and energy pulses of known amplitude.

CHEMS has eight trigger modes for the initiation of DPU classification and preparation of PHA events. The standard mode will accept double or triple

coincidence events. A triple coincidence only mode exists that may be useful during high background periods. A mode requiring a calibrate strobe is used during in-flight-calibrate periods. There is a mode requiring only an energy pulse that could be used in the event of a TOF failure. The other four trigger modes were used for diagnostic purposes before launch.

### 3.2.5. CHEMS Calibration

The CHEMS flight unit was calibrated before launch at the Goddard Space Flight Center accelerator facility. The final calibration was performed there in April 1997 using the MIMI flight unit DPU. The sensor was exposed to beams of various ion species ( $H^+$ ,  $H_2^+$ ,  $He^+$ ,  $C^+$ ,  $N^+$ ,  $O^+$ ,  $H_2O^+$ ,  $Ne^+$ ,  $Ar^+$ ,  $CO_2^+$ , and  $Kr^+$ ) at energies between 3.3 and 96 keV. These data were used to determine carbon foil thickness, SSD nuclear defect, TOF and energy resolution, and detection efficiencies as a function of energy and species.

**3.2.5.1. Time-of-Flight Resolution.** It is very important that the CHEMS instrument be able to distinguish between the suggested candidates for the heavy ion plasma in Saturn's magnetosphere. These ions include  $N^+$ ,  $O^+$ ,  $OH^+$ , and  $H_2O^+$ . The TOF distributions for three of those ions plus  $C^+$  are shown in Figure 33 for 96-keV beams. The distributions are well separated. At lower energies, the TOF

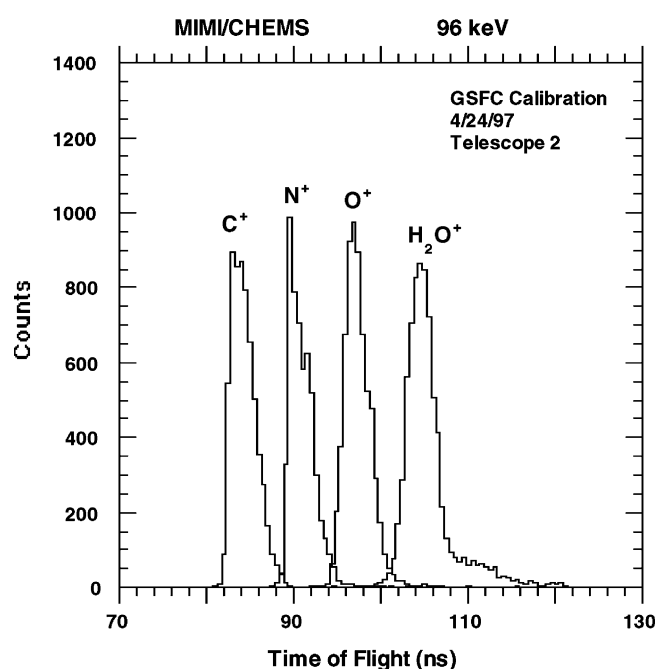


Figure 33. CHEMS time-of-flight distributions for 96 keV ions.

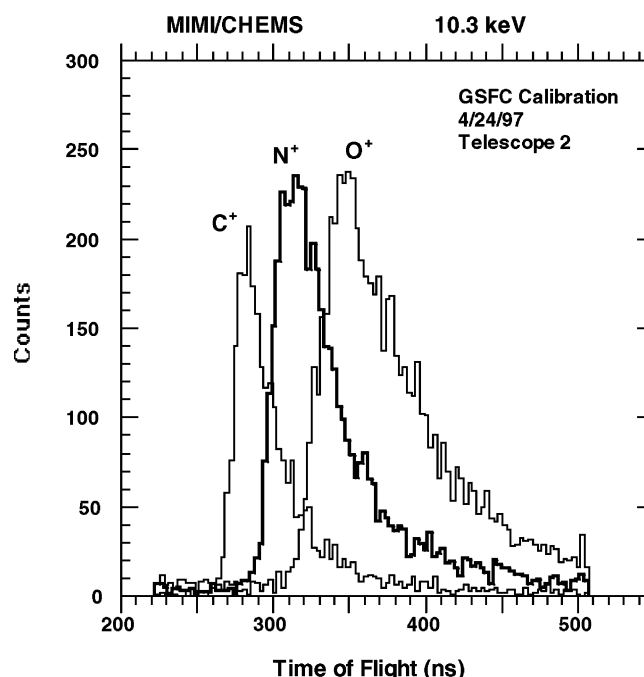


Figure 34. CHEMS time-of-flight distributions for 10 keV ions.

resolution worsens due to energy straggle in the carbon foil. Figure 34 presents distributions from 10.3 keV beams. The means of the three distributions are still well separated but the distributions are much broader.

**3.2.5.2. Efficiencies.** In general, the TOF detection efficiency increases with increasing energy in the CHEMS energy range. In Figure 35 the TOF start efficiency is shown as a function of beam energy for eight different ion species. The start efficiency was determined by dividing the double coincidence counting rate by the stop singles rate. The variation largely tracks the change in secondary electron emission.

The stop efficiency is displayed in Figure 36. The stop efficiency was determined by dividing the double coincidence counting rate by the start singles rate. The stop efficiency shows a larger variation than the start because it includes not only the variation in secondary electron production, but also the effect of scattering in the carbon foil. Ions that do not hit an SSD do not produce secondary electrons that can be detected. Since the SSD subtends a relatively small angle, the large decrease in stop efficiency at low energies and for heavier ions is largely due to increased scattering in the foil. The total TOF efficiency is obtained by multiplying the start and stop efficiencies.



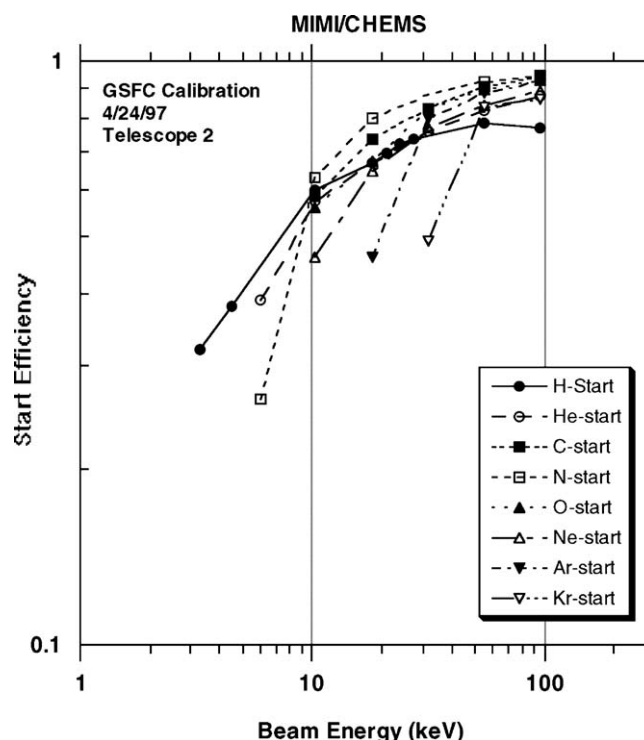


Figure 35. CHEMS TOF telescope start efficiencies. Start efficiencies include the effects of production and detection of secondary electrons from ions passing through the carbon foil.

3.2.5.3. *Comparison with the Wind/STICS Instrument.* The CHEMS sensor is very similar to the STICS sensor on GEOTAIL (Williams *et al.*, 1994) and the STICS sensor on the Wind spacecraft (Gloeckler *et al.*, 1995). However, a major effort was made to increase the TOF efficiency compared to those instruments. Two major changes were made. The CHEMS solid-state detectors are 56% larger in area than the STICS detectors and extensive 3-D modeling was performed to optimize the steering potentials to improve secondary electron collection. The results were a significant efficiency improvement as shown in Figure 37 for hydrogen and oxygen.

### 3.2.6. CHEMS in-Flight Performance

The CHEMS sensor returned excellent data from the Venus 2 and Earth flybys. Figure 38 illustrates its performance with triple coincidence PHA data from the outer portion of the Earth's ring current. Major species are labeled, and boxes for the four triple coincidence species rate implemented at the time of Earth flyby are shown. Observed resolution is consistent with that expected from prelaunch calibration. In June 2000, small changes were made to the CHEMS Range and Species definitions in the MIMI flight software. These later definitions are shown in

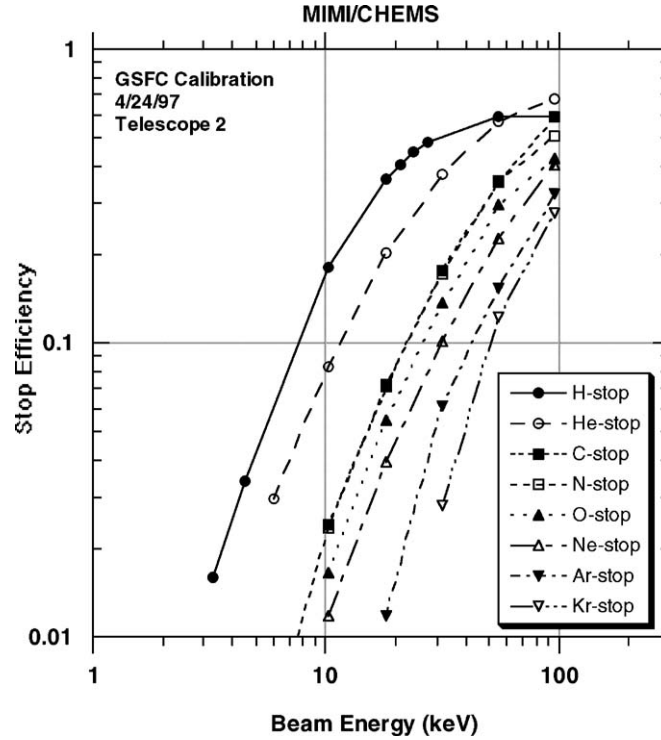


Figure 36. CHEMS TOF telescope stop efficiencies. Stop efficiencies include the effects of particle scattering in the carbon foil as well as the production and detection of secondary electrons from ions that hit the solid state detectors.

Figure 32 and listed in Tables XI and XIII including an additional triple coincidence species rate for high charge state CNO.

### 3.3. LOW ENERGY MAGNETOSPHERIC MEASUREMENTS SYSTEM (LEMMS)

#### 3.3.1. Detector Description

The LEMMS instrument is designed to measure the three-dimensional distribution of energetic ion and electron fluxes. The instrument head consists of a double-ended telescope (low energy and high energy end) heavily shielded by a platinum cover around the whole assembly to avoid penetrating particles with energies  $E < 30$  MeV through the sides of the instrument. The instrument head and the electronic boxes are mounted on top of a rotating platform. A picture of LEMMS is shown in Figure 39.

LEMMS rotates about the  $-y$ -axis of the spacecraft, co-aligned with the remote sensing and optical instruments, and therefore measures angular distributions of ions and electrons within a scan plane, defined by the  $x$ - $z$  plane in the spacecraft system of reference (see Figure 40). Three-dimensional particle

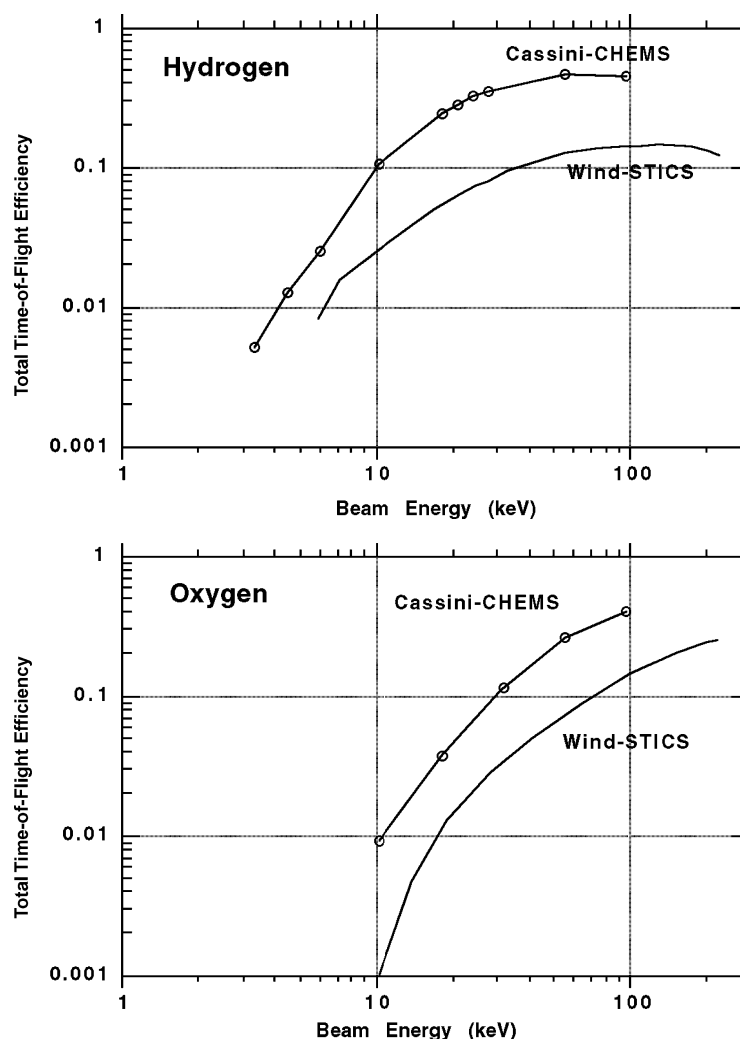


Figure 37. Comparison between Cassini-CHEMS and Wind-STICS TOF efficiencies for hydrogen and oxygen. Total efficiencies are the product of the start and stop efficiencies.

distributions can only be obtained if the spacecraft itself is rotating about the  $z$ -axis.

During one complete motor rotation, which is performed in 86 s, 16 subsectors are defined for all 57 counters (see Tables XIII and XIV). In addition four priority counters are defined for which each subsector is divided in eight microsectors as indicated in Figure 40. The low or high energy ends may be positioned behind the calibration shield for background measurements. Collimators define 7 and 19 hexagonal-shaped aperture entrance channels for the low and high energy end, respectively. This geometry is also used on the particle spectrometer EPD-LEMMS

TABLE XIII

Parameter of the semiconductor detectors used in the LEMMS instrument.

Detector	L/H end	Thickness ( $\mu\text{m}$ )	Active area ( $\text{mm}^2$ )
E1	Low	$300 \pm 15$	90
E2	Low	$300 \pm 15$	90
F1	Low	$700 \pm 15$	90
F2	Low	$300 \pm 15$	90
A	Low	$150 \pm 15$	35
B	Low	$700 \pm 25$	35
D1	High	$150 \pm 15$	100
D2	High	$700 \pm 15$	150
D3a	High	$700 \pm 15$	150
D3b	High	$700 \pm 25$	150
D4	High	$700 \pm 25$	150

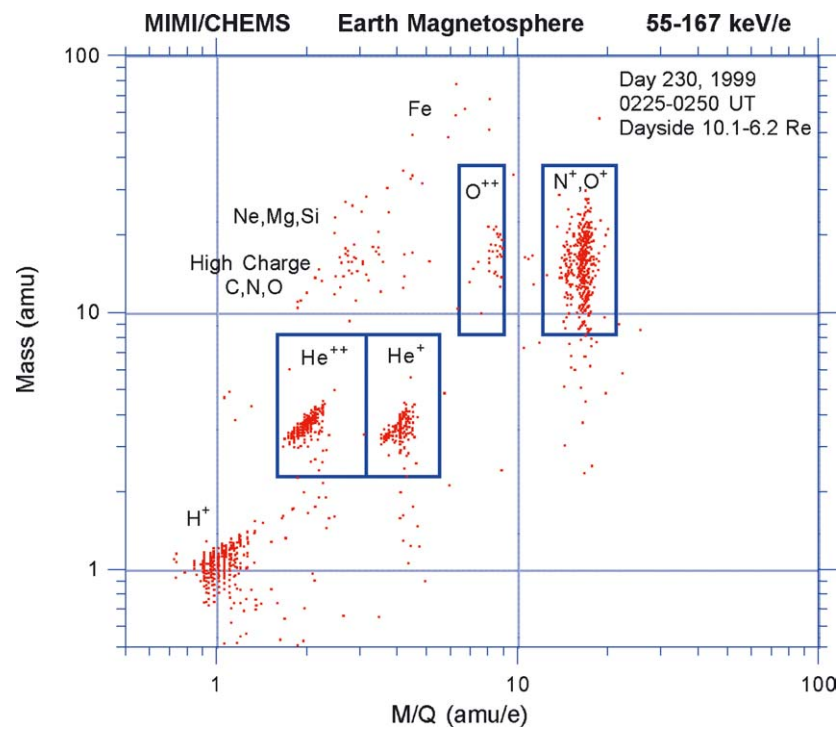


Figure 38. CHEMS PHA data from the outer portion of the Earth's ring current.

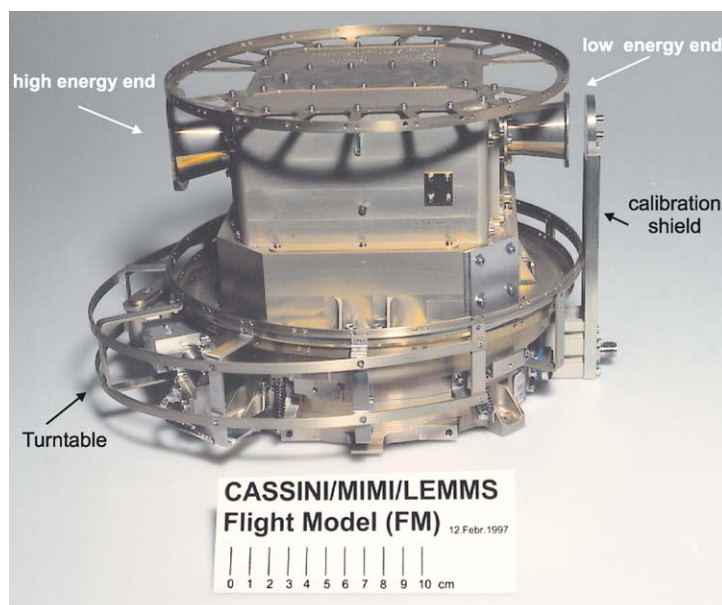


Figure 39. Photograph of the low energy magnetospheric measurement system (LEMMS) flight unit. The double-ended detector head (low energy end and high energy end) is surrounded by the electronic boxes and mounted on the programmable turntable platform. The calibration shield is used for background measurements.

on board the Galileo spacecraft and provides narrow acceptance angles for focused deflection of electrons inside the instrument. The new position of the instrument on the spacecraft (after the removal of the spacecraft scan platform) is different from originally planned. The LEMMS field of view is partly obscured by parts of the spacecraft itself. As shown in Figure 40, the cover of one of the radioactive thermal generators (RTG), one of the thrusters, and the high-gain antenna are partly blocking incoming particles. This obscuration limits the three-dimensional data coverage and has to be taken into account in the data analysis. Reflected sunlight from the cover of the RTG and the thruster is being removed for software routines comparing intensities in adjacent subsectors and by including energy spectral information.

### 3.3.2. Measurement Technique

The measurement principle of LEMMS is based on energy loss of incidenting particles in semiconductors. The position of the detectors inside the assembly determines the species and energy of the incidenting particle. The overall configuration of LEMMS and the positions of all the 11 semiconductor silicon detectors are shown in Figure 41. Table XIII summarizes the parameters of the LEMMS detectors.

*Low Energy End.* The low energy end of LEMMS is designed to measure low-energy ions ( $E \geq 30$  keV) and electrons (15 keV–1 MeV). An inhomogeneous

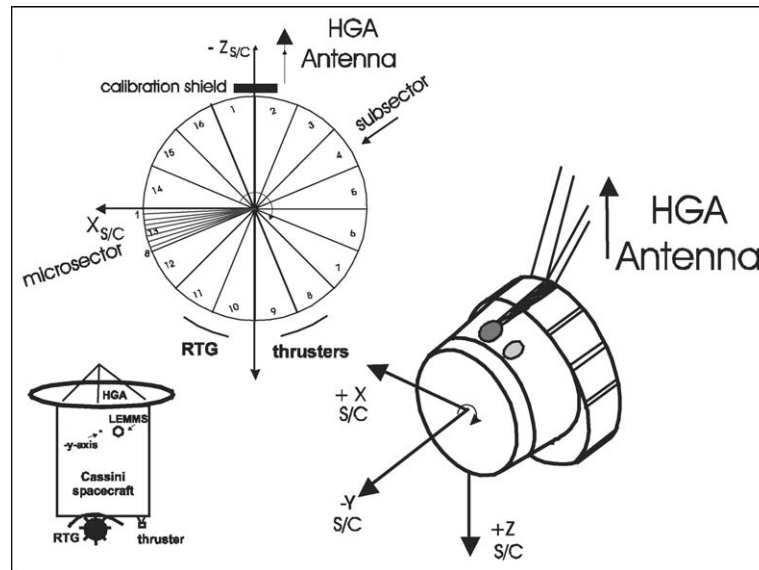


Figure 40. Upper left: LEMMS scan plane defined by the  $x$ - $z$  plane in the spacecraft frame of reference; lower left: LEMMS position on the spacecraft. The high-gain antenna (HGA), the cover of one of the radioactive thermal generators (RTG), and one of the thrusters are partly obscuring the field of view of the instrument; right: LEMMS orientation in the spacecraft frame of reference with the scan platform rotation axis along the  $-y$ -axis.

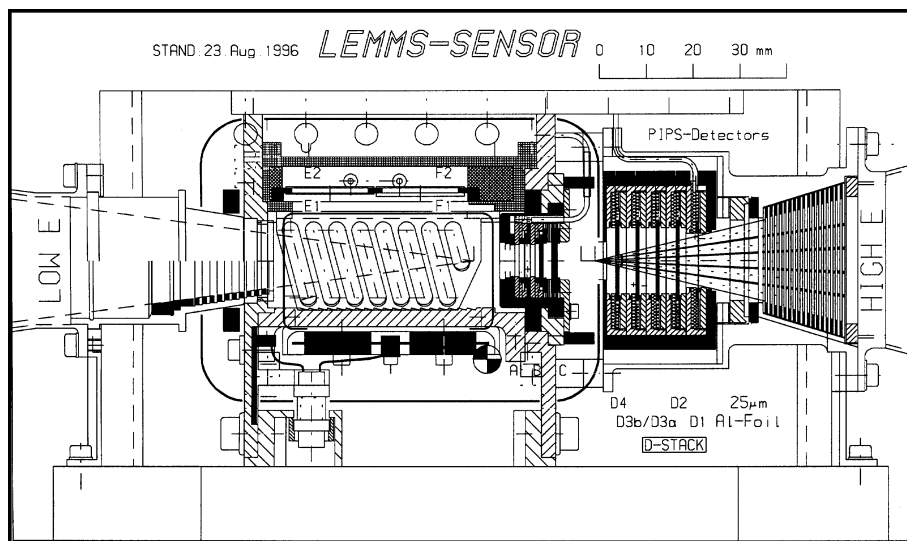


Figure 41. Configuration of the LEMMS detector head. Low energy particles entering the low energy end (LOW E) are measured with detectors E1, E2, F1, F2 (for electrons) and A, B (for ions). Particles with higher energies entering the high energy end (HIGH E) are detected in a stack of detectors (D1, D2, D3a, D3b, D4). Between detectors B and D4 a gold absorber C is inserted. The whole assembly is shielded with a platinum box.

TABLE XIV  
LEMMS channels description (low energy end) from calcluations and calibration measurements.

Readout N	LEMMS channels	Logic	L/H end	Species	P		He		C		O		Fe		Electrons		Geometry factor cm <sup>2</sup> -sr
					$E_{min}$ (MeV)	$E_{max}$ (MeV)	$E_{min}$ (MeV/N)	$E_{max}$ (MeV/N)	$E_{min}$ (MeV/N)	$E_{max}$ (MeV/N)	$E_{min}$ (MeV/N)	$E_{max}$ (MeV/N)	$E_{min}$ (MeV/N)	$E_{max}$ (MeV/N)	$E_{min}$ (MeV)	$E_{max}$ (MeV)	
0	A0	A1(A2)(B1)	Low	$Z \geq 1$	0.027	0.035	0.008	0.010	0.004	0.0048333	0.004	0.004	0.003	0.003			0.0112 A0
1	A1	A2(A3)(B1)	Low	$Z \geq 1$	0.035	0.056	0.01	0.016	0.0048333	0.007	0.004	0.006	0.003	0.004			0.0112 A1
2	A2	A3(A4)(B1)	Low	$Z \geq 1$	0.056	0.106	0.01575	0.029	0.007	0.012	0.006	0.010	0.004	0.006			0.0112 A2
3	A3	A4(A5)(B1)	Low	$Z \geq 1$	0.106	0.255	0.02925	0.068	0.012	0.0260833	0.010	0.021	0.006	0.011			0.0112 A3
4	A4	A5(A6)(B1)	Low	$Z \geq 1$	0.255	0.506	0.0675	0.130	0.0260833	0.0483333	0.021	0.038	0.011	0.018			0.0112 A4
5	A5	A6(A7)(B1)	Low	$Z \geq 1$	0.506	0.805	0.13	0.205	0.0483333	0.075	0.038	0.058	0.018	0.025			0.0112 A5
6	A6	A7(A8)(B1)	Low	$Z \geq 1$	0.805	1.6	0.205	0.400	0.075	0.1416667	0.058	0.106	0.025	0.043			0.0112 A6
7	A7	A8(A9)(B1)	Low	$Z \geq 1$	1.6	3.5	0.4	0.875	0.1416667	0.3	0.106	0.231	0.043	0.080			0.0112 A7
8	A8	A9(B1)	Low	$Z \geq 1$	3.5	4	0.875	4.000	0.3	7.25	0.231	8.313	0.080				0.0112 A8
9	B0	A8(A9)B1(B5)(D41)	Low	$Z \geq 1$	4.10	7.70	17.5	41.000	250.00								0.0112 B0
10	B1	A6(A8)B4(B5)(D41)	Low	$Z \geq 1$	7.70	14.00	41.3	67.750									0.0112 B1
11	B2	A9B1(B5)(D41)	Low	$Z \geq 1$	4.00	4.10	4.0	5.500	7.25	316.67	8.375	8.625	13.11	13.36			0.0112 B2
12	B3	A9B5(D41)	Low	$Z > 1$			5.5	15.500	7.58	316.67	8.625		13.41				0.0112 B3
13	BE	A2(A7)B1(B3)(D41)	Low	e <sup>-</sup>											1	2.6	0.0112 BE
14	C0	E11(E12)(E22)	Low	e <sup>-</sup>											0.020	0.030	0.0075 C0
15	C1	E12(E13)(E22)	Low	e <sup>-</sup>											0.030	0.045	0.0207 C1
16	C2	E13(E14)(E22)	Low	e <sup>-</sup>											0.045	0.060	0.0324 C2
17	C3	E14(E15)(E22)	Low	e <sup>-</sup>											0.060	0.100	0.0321 C3
18	C4	E15(E16)(E22) + F11(F12)(E22)	Low	e <sup>-</sup>											0.100	0.200	0.0271 C4
19	C5	F12(F13)(E22)	Low	e <sup>-</sup>											0.170	0.300	0.0102 C5
20	C6	F13(F14)(E22)	Low	e <sup>-</sup>											0.300	0.528	0.0250 C6
21	C7	F14(F15)(E22)	Low	e <sup>-</sup>											0.528	0.900	0.0258 C7
22	AS	A1	Low	$Z \geq 1$	0.027		0.008		0.004		0.003		0.003				— AS
23	BS	B1	Low	$Z \geq 1$	4		4.0		7.250		8.375		13.11				— BS
24	ES	E11	Low	e <sup>-</sup>											0.02		— ES
25	E2/F2S	E22	Low	e <sup>-</sup>											1		— E2/F2
26	FS	F11	Low	e <sup>-</sup>											0.1		— FS

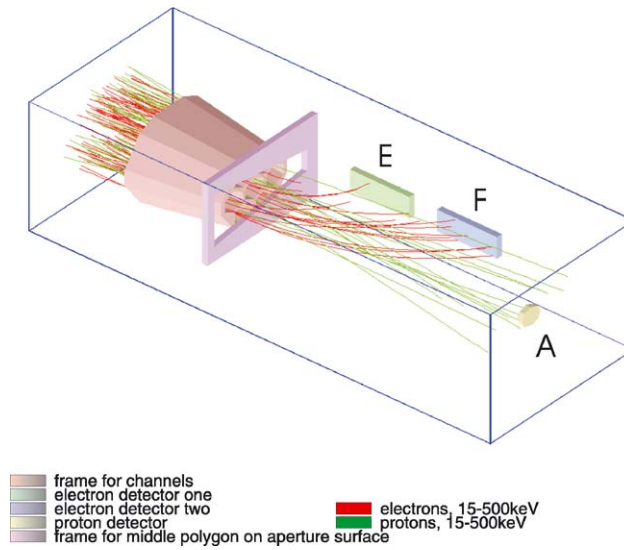


Figure 42. Particle trajectories in the LEMMS low energy end geometry from simulation.

magnetic field produced by an internal permanent magnet separates incident ions and electrons which subsequently strike different detectors inside. Figure 42 illustrates sample particle trajectories in the internal magnetic field. Electrons and ions enter the low energy end from the left through the collimator. Low-energy electrons up to 884 keV are deflected by the magnet and measured by the electron detectors E (E1 and E2) and F (F1 and F2) depending on their incident energy. Electrons with energies between 200 and 600 keV are detected in both electron detectors dependent on their collimator entrance angles. Therefore, the calculated geometric factors as shown in Figure 43 overlap in that energy range.

Electrons with energies  $E \leq 1$  MeV cannot reach detector A directly. However, low-energy ions, which are less affected by the magnetic field, are measured by the low energy end ion detectors A and B (B not shown in the simulation). The aperture angle of the low energy end collimator is  $15^\circ$ . Between detectors B and the high energy end detector D4, a Gold-absorber ( $1000 \mu\text{m}$ ,  $75 \text{ mm}^2$ ) is inserted to stop particles penetrating detectors A or B incident from the low energy end. LEMMS data from detectors A, E1, and F1 are also processed through a pulse height analyzer (PHA) that produces 64-channel energy spectra splitted in two ranges 32 channels each.

In addition to the 27 counters of the low energy end four priority counters (A0, A1, C0, C1) are selected which have microsector angular resolution, as mentioned above. Table XIV summarizes the low energy end electron and ion channels defined by logical conditions between the different electronic detector thresholds. The energy ranges mentioned in the tables are based on energy loss calculations and calibrations for the various detectors.



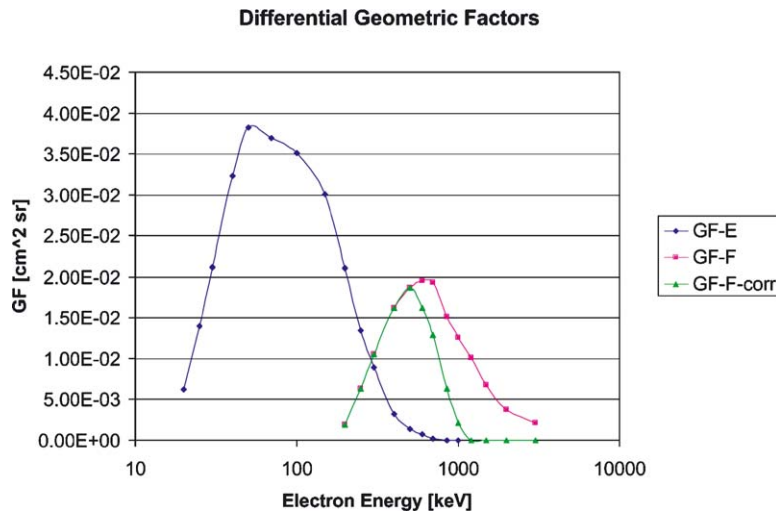


Figure 43. Geometric factors as a function of energy for detectors E, F and A for electrons calculated from detailed simulation results of the low energy end of LEMMS.

*High Energy End.* The high energy end consists of a stack of five detectors D1, D2, D3a, D3b, and D4 to measure high-energy ions (1.5–160 MeV/N) and electrons (0.1–5 MeV). In front of detector D1 a 25 mm Al-foil is inserted to suppress incoming light and the flux of low-energy ions. The opening angle of the high energy end collimator is 30°. The parameters of the high energy end detectors can be found in Table XV, and the calculated and measured electron and ion energy channel boundaries are shown in Table XVI. A summary of the thicknesses and active areas of the detectors used in LEMMS is given in Table XIII.

### 3.3.3. LEMMS Turntable

*Description of Features.* To be able to measure particles in every direction, the LEMMS experiment is mounted on a rotating platform which was developed by the Finnish company VIT Automation Space Technology. A photograph of the turntable without the LEMMS detector head and electronic is shown in Figure 44.

The turntable (TT) is able to rotate continuously left- or right-handed within 360°. It is designed for a 3 million revolutions lifetime in the temperature range of –35 to +45°C. The rotation speed is selectable from a range of 2° to about 12°/s. This is realized with a stepper motor and custom designed drive electronics with closed-loop control. The accuracy to let the motor rotate to a fixed position is about 0.01°. The TT provides the mechanical platform for the instrument and an attachment ring for the spacecraft (MLI). It is locked during launch by a Marman clamp ring, which is released by a thermal wax actuator. The TT also provides a 21 contact slip ring assembly for the LEMMS electrical signals, and a feedthrough for purge gas. The weight of the TT is 3.2 kg, and the power consumption is 2.5 W.

TABLE XV  
LEMMS channels description (high energy end) from calulations and calibration measurements.

Readout N	LEMMS channels	Logic	L/H end Species	p		He		C		O		Fe		Electrons		X-rays	
				$E_{min}$ (MeV)	$E_{max}$ (MeV)	$E_{min}$ (MeV/N)	$E_{max}$ (MeV/N)	$E_{min}$ (MeV/N)	$E_{max}$ (MeV/N)	$E_{min}$ (MeV/N)	$E_{max}$ (MeV/N)	$E_{min}$ (MeV/N)	$E_{max}$ (MeV/N)	$E_{min}$ (MeV)	$E_{max}$ (MeV)	$E_{min}$ (MeV)	$E_{max}$ (MeV)
27	E0	D11(D12)(D21)	High	Z = 1, e <sup>-</sup>	1.2	1.4								0.15	0.2	0.08	
28	E1	D11(D12)(D31)	High	e <sup>-</sup>										0.25	1		
29	E2	(D11)(D21)(D31)	High	e <sup>-</sup>										0.4	0.75	0.06	
30	E3	(D12)(D21)(D22)(D31)(D32)(D41)	High	e <sup>-</sup>										0.7	4		
31	E4	(D12)(D21)(D22)(D32)(D33)(D41)	High	e <sup>-</sup>										0.9	3		
32	E5	D21(D22)(D32)(D33)	High	e <sup>-</sup>										1.1			
33	E6	D32(D33)(D41)(D42)(B1)	High	e <sup>-</sup>										2.7	18		
34	E7	D41(D42)(B1)(B2)	High	e <sup>-</sup>										18			
35	G1	(D21)(D31)(D32)(D41)	High	X-ray												0.05	0.4
36	P1	D13(D15)(D21)	High	All	1.42	2.28	1.4	1.48	2.17	2.25	2.31	2.44	2.75	0.3	1	0.4	1.8
37	P2	D15(D16)(D21)	High	Z = 1, Z > 1	2.28	4.49	1.5	2.00	2.25	2.42	2.44	2.56	2.86	3.00		1.8	5.4
38	P3	D15(D16)(D21)(D23)(D31)	High	Z = 1	4.49	5.74											
39	P4	D12(D16)(D23)(D24)(D31)	High	Z = 1	5.74	7.89											
40	P5	D12(D15)(D24)(D25)(D31)	High	Z = 1	8.31	11.45											
41	P6	D24(D25)(D32)(D34)(D41)	High	Z = 1	11.47	13.43											
42	P7	D21(D25)(D33)(D35)	High	Z = 1	12.10	58.90	42.5	475.00									
43	P8	D12(D15)(D22)(D23)(D33)	High	Z = 1	25.19	59.00	142.5	475.00									
44	P9	D22(D25)(D32)(D33)	High	Z = 1, e <sup>-</sup>	58.99		475.0							1			5.14
45	H1	D16(D17)(D21)	High	Z > 1			2.0	4.5	2.42	3.08	2.56	3.13	3.04	3.36			
46	H2	D16(D17)(D21)(D26)	High	Z > 1			4.5	10.5	83.33	166.67							
47	H3	D25(D26)(D32)	High	Z > 1			11.3	25	83.33	666.67							
48	H4	D23(D25)(D35)	High	Z > 1			25.0	42.5	666.67								
49	H5	D22(D34)(D35)(D45)	High	Z = 1, Z > 1	20	25	42.5	75									
50	Z1	D17(D21)	High	Z > 6					3.08	8.00	3.13	9.38	3.36	14.64		19	
51	Z2	D17(D21)(D31)	High	Z > 6					8.00	20.92	9.38	24.38	14.64	42.86			
52	Z3	D26(D32)	High	Z > 6					20.92	83.33	24.38	187.50	42.86				
53	D1	D11	High	All	1.40	1.3			2.17		2.31	2.73		0.15	0.27		
54	D2	D21	High	All	4.40	4.5			8.00		9.38	14.64		0.18			
55	D3	D31	High	All	11.20	11.3			21.00		24.38	42.86		0.5			
56	D41	D41	High	All	19.00	19.5			36.17		42.50	76.79		1			

TABLE XVI  
Nominal electronic thresholds for the LEMMS detectors.

Detector A → PHA				Detector B			
Energy	Thresholds		Amp.	Energy	Threshold		Amp.
	Level	Description			Level	Description	
12 keV*	43.5 mV	A1	2nd	100 keV*	120 mV	B1	2nd
30 keV	108.75 mV	A2	2nd	400 keV	480 mV	B2	2nd
50 keV	181.25 mV	A3	2nd	1 MeV	230.8 mV	B3	1st
100 keV	362.5 mV	A4	2nd	4 MeV	923 mV	B4	1st
250 keV	906.25 mV	A5	2nd	13 MeV	3 V	B5	1st
500 keV	1.813 V	A6	2nd				
800 keV	2.9 V	A7	2nd				
1.6 MeV	0.96 V	A8	1st				
5 MeV	3.0 V	A9	1st				
Detector D1				Detector D2			
75 keV*	121.4 mV	D11	2nd	50 keV*	90 mV	D21	2nd
200 keV	323.7 mV	D12	2nd	700 keV	1.26 V	D22	2nd
400 keV	647.4 mV	D13	2nd	3 MeV	247.5 mV	D23	1st
760 keV	1.23 V	D14	2nd	6 MeV	495 mV	D24	1st
1.6 MeV	293 mV	D15	1st	12 MeV	0.99 V	D25	1st
5 MeV	916.7 mV	D16	1st	40 MeV	3.3 V	D26	1st
18 MeV	3.3 V	D17	1st				
Detector D3				Detector D4			
50 keV*	90 mV	D31	2nd	100 keV*	66 mV	D41	1st
400 keV	720 mV	D32	2nd	400 keV	264 mV	D42	1st
3 MeV	618.7 mV	D33	1st	1 MeV	660 mV	D43	1st
6 MeV	1.238 V	D34	1st	2.8 MeV	1.85 V	D44	1st
16 MeV	3.3 V	D35	1st	5 MeV	3.3 V	D45	1st
Detector E1 → PHA				Detector F1 → PHA			
15 keV*	100 mV	E11	2nd	100 keV*	120.4 mV	F11	1st
30 keV	200 mV	E12	2nd	170 keV	205 mV	F12	1st
45 keV	300 mV	E13	2nd	300 keV	361 mV	F13	1st
60 keV	400 mV	E14	2nd	530 keV	638 mV	F14	1st
100 keV	667 mV	E15	2nd	880 keV	1.06 V	F15	1st
200 keV	1.333 V	E16	2nd				
Detector E2/F2 (anti)							
\$50 keV*	100 mV	E2F2	1st				

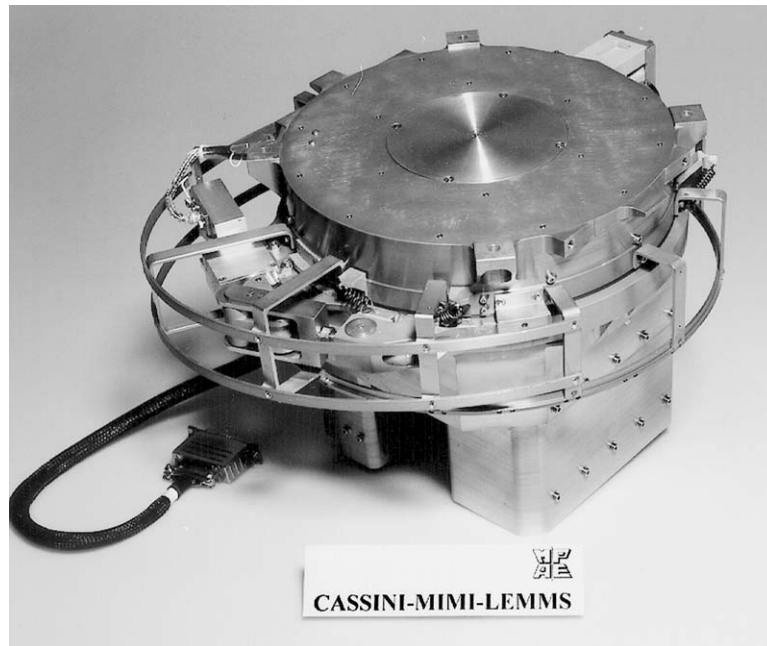


Figure 44. Photograph of the LEMMS turntable, developed by the Finnish company VTT.

#### 3.3.4. LEMMS Electronics

The LEMMS sensor electronics block diagram is shown in Figure 45. The signals coming from the silicon detectors are led to nine separate amplifier boards. Each of these boards includes low noise input FET, charge sensitive amplifier (CSA), differentiator, Gaussian filter and linear amplifiers. A power supply filter for each detector is also implemented. The amplifier boards for A, E1, D1 are designed for low-noise contribution. Amplifier board A with FWHM pulse-width of 900 ns generates less than 11 keV (FWHM) noise, E1 with 1900 ns/15  $\mu$ s as bipolar pulse less than 8 keV, and D1 with 470 ns width less than 15 keV. A power supply generates the detector bias voltages. The first supply provides four different voltages, 3-bit programmable from 0 to approximately 176 V. The second supply has been implemented both for redundancy and detector fine adjustment. It is 3-bit programmable with about 10% higher voltages.

The amplifier output pulses travel to the coincidence board #3, containing discriminators, coincidence logic, and counters. Eighteen 4-bit commandable discriminators and sixteen 24-bit accumulators are integrated in one ASIC each. Together, four accumulator and three discriminator chips are used. The control and communication to the sensor controller has been integrated into one 1020 Actel FPGA. 58 accumulators out of 64 for coincidences and 49 thresholds can be programmed individually from ground.

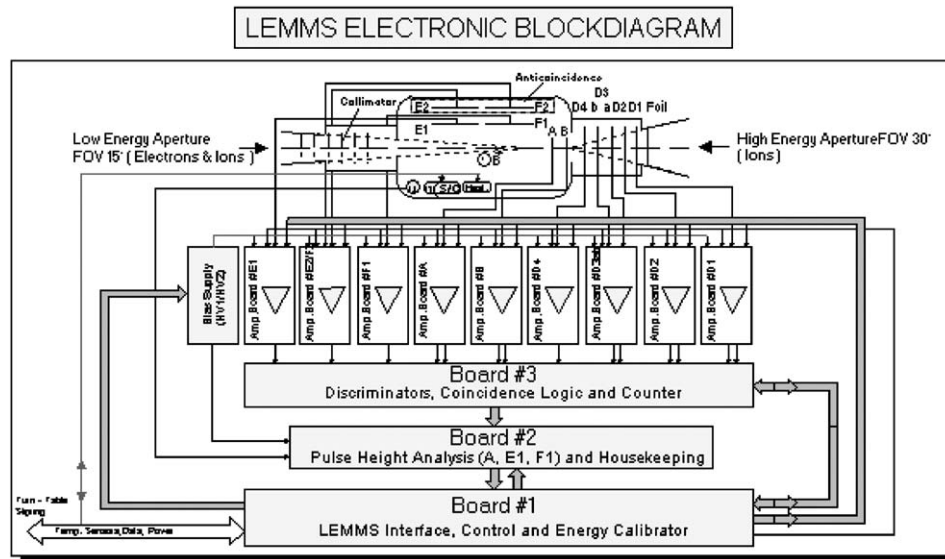


Figure 45. LEMMS electronics block diagram.

For the A, E1, and F1 detectors, a 7-bit pulse height analysis is done. The three channels are serially multiplexed. To cover the whole dynamic range there is a low- and a high-resolution mode for each detector. The corresponding mode is automatically indicated. These electronics are located on board #2, together with the house-keeping electronics that convert the sensor and electronic temperatures, as well as supply voltages into 7-bit digital data.

Board #1 contains the differential interface to the DPU, the sensor controller, integrated into one 1020 Actel FPGA and the energy calibrator. This internal calibrator generates stimulation signals for all amplifier boards from 3.5 keV to 40 MeV in two 8-bit ranges to check the electronics and the logic.

Data, power, and control signals to the sensor connect from the DPU via a 21 contact slip ring, integrated in the turntable. The electronic thresholds of the various LEMMS detectors are summarized in Table XVI.

### 3.3.5. LEMMS Calibration

More than 4600 calibration files have been accumulated over several calibration campaigns which have been performed to investigate the instruments characteristics. We used different beam facilities to calibrate the instrument with ions and electrons in various energy ranges. In addition we used radioactive sources for high-energy electron and gamma calibration.

The complete flight hardware was the subject of extensive tests, including internal calibrator tests, energy scans, motor position scans, vertical and horizontal

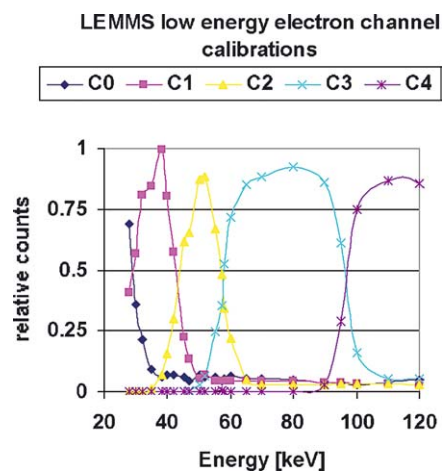


Figure 46. Determination of energy channel limits for electrons for LEMMS channels C0–C4 of the low energy end.

angle scans, detector threshold scans, and scans with and without collimators. As an example we show two energy scans from which the energy channels have been determined. Figure 46 shows the normalized count rates of several energy channels (C0–C4) from detectors E and F as a function of energy. The points where two curves from different channels cross each other were used to determine lower and upper energy limits for each channel. Figure 47 shows a similar energy scan for

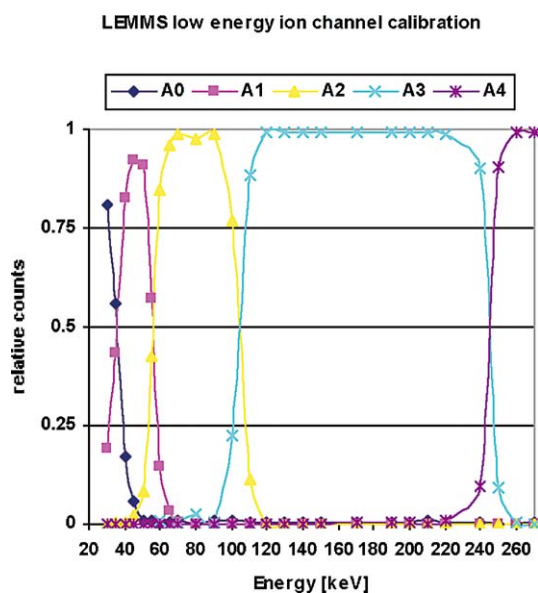


Figure 47. Determination of energy channel limits for ions for LEMMS channels A0–A4 of the low energy end.

ions measured in detector A (A0–A4). The results of these energy scans analyzed so far are summarized in Table XIV for the low energy end and in Table XV for the high energy end of the instrument.

### 3.3.6. First in-Flight Results

After a calibration period in January 1999 and a turn-on of LEMMS during the second Venus flyby in June 1999, the spacecraft returned to Earth in August 1999 to perform a close flyby. During this encounter LEMMS was switched on for nearly 4 weeks (August 17 to September 14, 1999). Cassini passed the Earth's radiation belts and left the Earth through the dawn magnetotail. The flyby was used for calibration in a “known” environment. Figure 48 shows the LEMMS particle measurements obtained during the Earth swingby inside the magnetosphere. The dynamic range of LEMMS covers nearly 6 decades in proton energies, more than 3 decades in electron energies, and 7 decades in intensities. The LEMMS parameters are summarized in Table XVII.

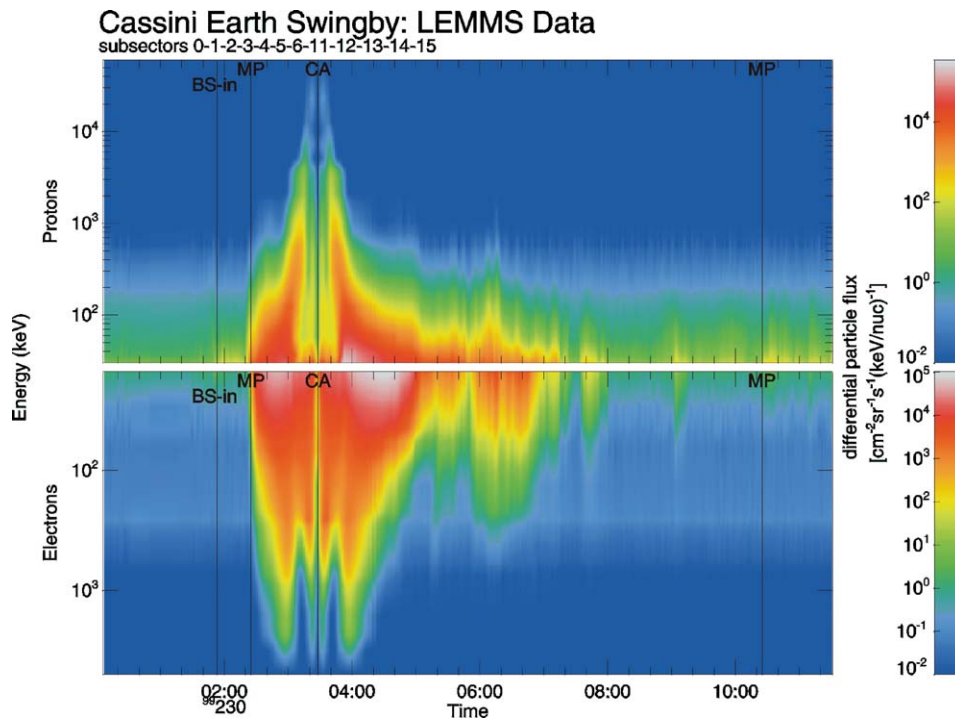


Figure 48. LEMMS energy spectra for protons and electrons in the Earth magnetosphere during the Cassini flyby on August 18, 1999. Solid lines mark the bow shock (BS) and magnetopause (MP) crossings, and the closest approach (CA) of the spacecraft. The highest intensities were measured in the radiation belts.

TABLE XVII  
LEMMS parameters summary.

Instrument name	Low energy magnetospheric measurement system (LEMMS)
Scientific objectives	Determination of the angular distribution of energetic particles in Saturn's magnetosphere
Principle	Measurement of energy loss of incident particles in semiconductor detectors
Design	Double-ended sensor head mounted on top of a programmable turntable
Aperture opening angle (full width)	15° (low energy end); 36° (high energy end)
Number of solid-state detectors	11
Species identification	Separation between electrons and ions through magnetic deflection (low energy end) and coincidence logic in a stack of four detectors (high energy end)
Number of channels	57 normal counters 4 priority counters 64 PHA channels for detectors A, E1, F1
Rotation axis	−y-axis of the S/C system
Scan plane	x–z plane of the S/C system
Angular resolution	22.5° per subsector (16 subsectors) 2.81° per microsector (128 microsectors)
Time resolution	86 s per rotation 5.31 per subsector 0.66 s per microsector
Energy range	<i>Normal counters</i> Ions: 0.030–160 MeV Electrons: 0.015–5.0 MeV <i>Priority counters</i> Ions: 0.030–0.036 and 0.036–0.053 MeV Electrons: 0.015–0.028 and 0.028–0.043 MeV
Weight	6.72 kg
Power consumption	5.2 W

### 3.4. SYSTEM CONFIGURATION

#### 3.4.1. Main Electronics Unit and Power Distribution

The MIMI instrument electronics is spread throughout the four assemblies that comprise the instrument (Figure 49). As seen in the sensor block diagrams (Figure 50), each of the three sensors contains amplifier chains and high voltage/bias supplies to operate detectors and provide steering voltages for the particle optics. This minimal set of electronics is sufficient to detect events and buffer the signals for further



## Cassini MIMI Instrument Overview

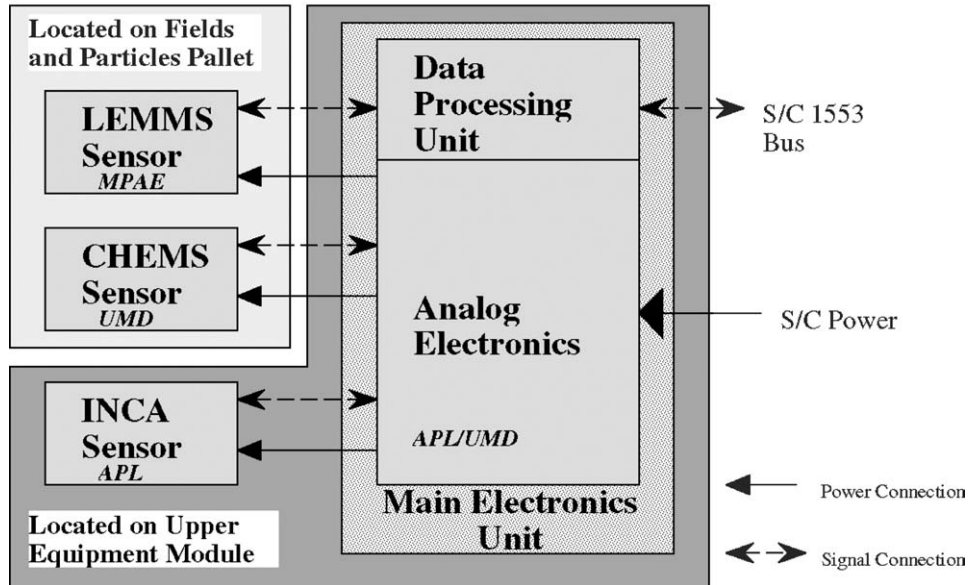


Figure 49. Cassini MIMI instrument overview.

central processing. The overall system parameters are shown in Table XVIII. *MEU*. The majority of the instrument analog and digital processing electronics is located in the Main Electronics Unit (MEU). This subsystem accepts the information from the sensors and performs necessary amplification, processing, and buffering of the event data. The signals from the CHEMS and INCA sensors are sent to the MEU as analog waveforms. The LEMMS events are sent in digital form, however, to reduce the effects of noise pickup in the sensor's rotating slipring interface. This is possible because the LEMMS event processing is significantly simpler than that

TABLE XVIII  
MIMI system overview.

Subsystem	Mass (kg)	Nominal power (W)	Allowable flight operational	Temp limits non-ops
INCA	6.92	3.0	-20/+35	-25/+50
CHEMS	6.66	3.5	-20/+35	-25/+40
LEMMS	6.72	5.2	-20/+35	-25/+40
MEU	7.20	8.6	+5/+50	+5/+50
Coax cables	0.61			
Total	28.11	20.3		

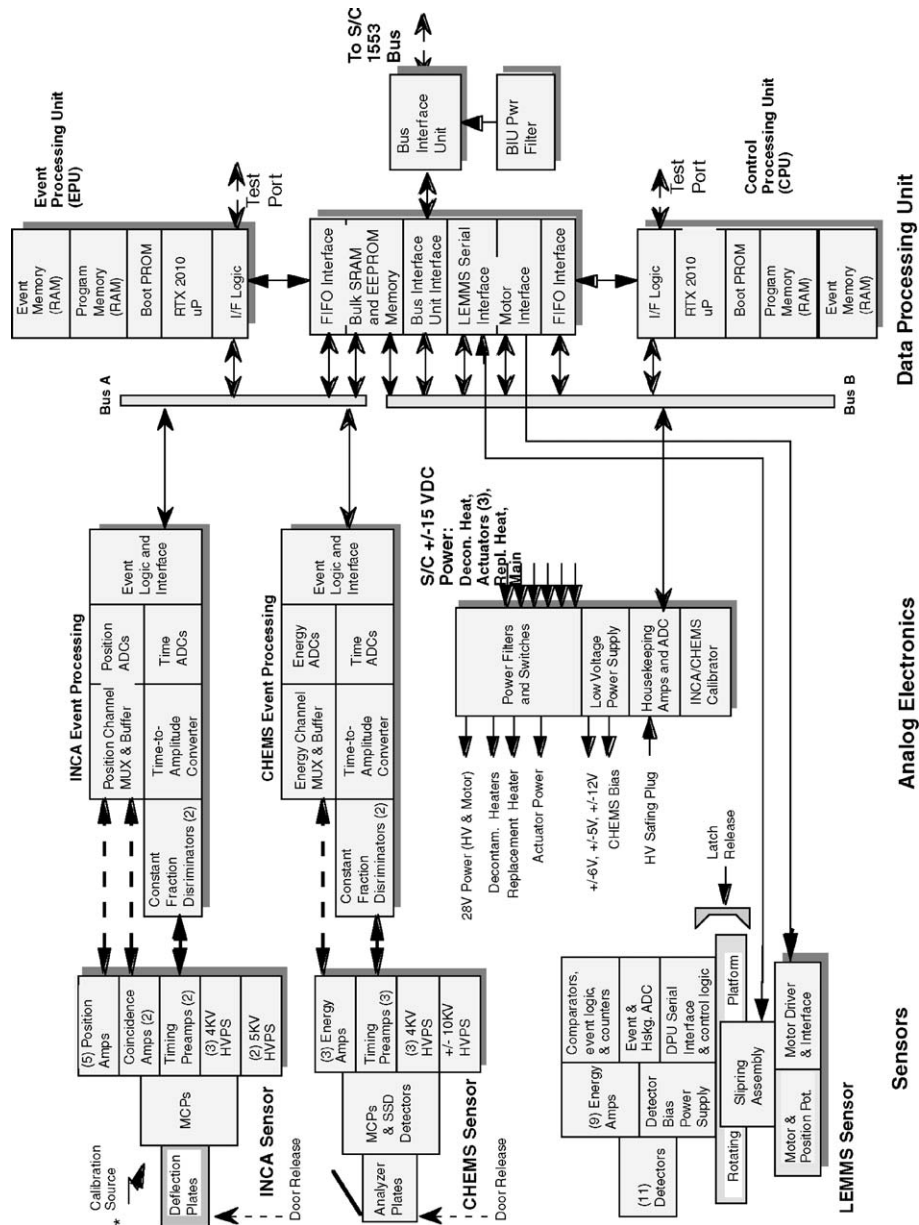


Figure 50. MIMI instrument block diagram.

for INCA or CHEMS, and the necessary digital logic could be co-located with the detector amplifiers.

In addition to processing events, the MEU also handles all spacecraft data and power interfaces, produces all secondary power voltages, and monitors the analog and digital status of the instrument. These functions are split between the two halves of the MEU: all analog processing is performed in the analog electronics (AE) section, and almost all digital processing is performed in the data processing unit (DPU). Both of these are physically located in the MEU enclosure, separated by a thin wall (to reduce EMI).

The analog electronics is comprised of nine PC boards (Figure 51): the low voltage power supply (LVPS), the LEMMS power interface board, the analog electronics motherboard, and six analog processing boards (power interface, housekeeping, CHEMS processing, CHEMS TAC, INCA processing, and INCA TAC).

MIMI has six spacecraft primary power interfaces: the LEMMS replacement heater, the sensor decontamination heaters (all run in parallel), the main instrument electronics power interface (LVPS), and one each for the sensor wax actuators (door/latch releases). The power for each of these interfaces is switched in the spacecraft via a solid-state hybrid. The hybrid provides current measurement, over-current limiting and cutoff, and controlled rise time activation.

The LVPS, mounted to the MEU side wall, supplies power to all three sensor assemblies and their processing electronics in the MEU. The converter produces

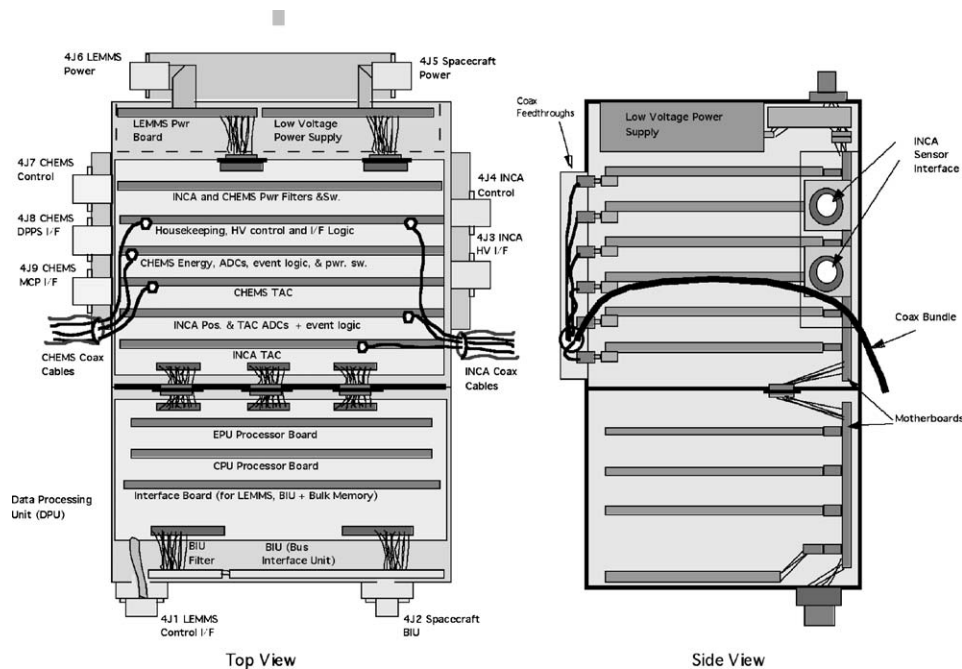


Figure 51. MIMI MEU configuration.

secondary voltages of  $\pm 5$  V (analog),  $\pm 6$ ,  $\pm 12$ ,  $\pm 5$  V (digital), +28, and +150 V (CHEMS bias) with an overall efficiency of 73% (nominal loads). The converter runs at 250 kHz (synchronized to the BIU 1 MHz reference) using push–pull drivers and current mode control. The +5V DPU and CHEMS bias outputs have separate windings, while the other outputs are stacked on a single tapped winding; all outputs share a single return (signal ground), which is tied to the spacecraft chassis ground only within the MEU.

The instrument includes a number of power switches to control the INCA and CHEMS high voltage supplies, the LEMMS motor and processing electronics, the analog processing electronics, and the INCA shutter mechanism. Most of the power switching is accomplished on the LEMMS power interface board and INCA/CHEMS power interface board. Also included on these boards are power filters for each of the spacecraft interfaces; these were included in an effort to isolate the instrument from noise generated elsewhere on the spacecraft. Figure 52 shows the power distribution within the instrument.

#### 3.4.2. Instrument Processing Boards

The INCA and CHEMS event data receive similar processing within the MEU. Two boards are dedicated to each sensor; one board to process time-of-flight information and the other to process the energy (CHEMS) or position (INCA) information.

The CHEMS time-to-amplitude (TAC) board accepts “start” and “stop” pulses from the microchannel plate (MCP) anodes in each of the three telescope heads (Figure 53). If the time between correlated “start” and “stop” pulses is measured to be between 9 and 540 ns, a “valid TOF” signal is sent to the CHEMS processing board, along with a TOF pulse whose amplitude is proportional to the measured particle flight time. If no “stop” is detected, the TAC circuitry resets itself at the end of the 540-ns window; the reset is delayed an additional 1000 ns when a “valid TOF” pulse is generated. No pile-up detection is performed during the TOF event analysis.

The CHEMS processing board accepts a shaped, unipolar (600 ns to peak) solid-state detector (SSD) energy pulse from each of the three telescopes in the CHEMS sensor and the TOF pulse from the TAC board. If the energy pulse exceeds a programmable threshold level, and valid event criteria are met, the energy and TOF pulse amplitudes are then converted to digital values and stored for retrieval by the DPU. The typical event criteria for CHEMS is a valid time-of-flight with the START, STOP, and ENERGY (optional) signals from the same telescope. Composite rates and individual TOF and energy rates are accumulated in hardware counters for periodic retrieval by the DPU. The board also contains the power switches for the INCA and CHEMS amplifier and analysis circuitry.

The INCA TAC board is very similar to the CHEMS TAC board, but only one start and one stop input are used (Figure 54). The acceptable TOF range is from 1 to 100 ns; the circuitry will reset itself 120 ns after an uncorrelated “start” pulse is measured, and 1.5  $\mu$ s after a “start” pulse and correlated “stop” pulse are

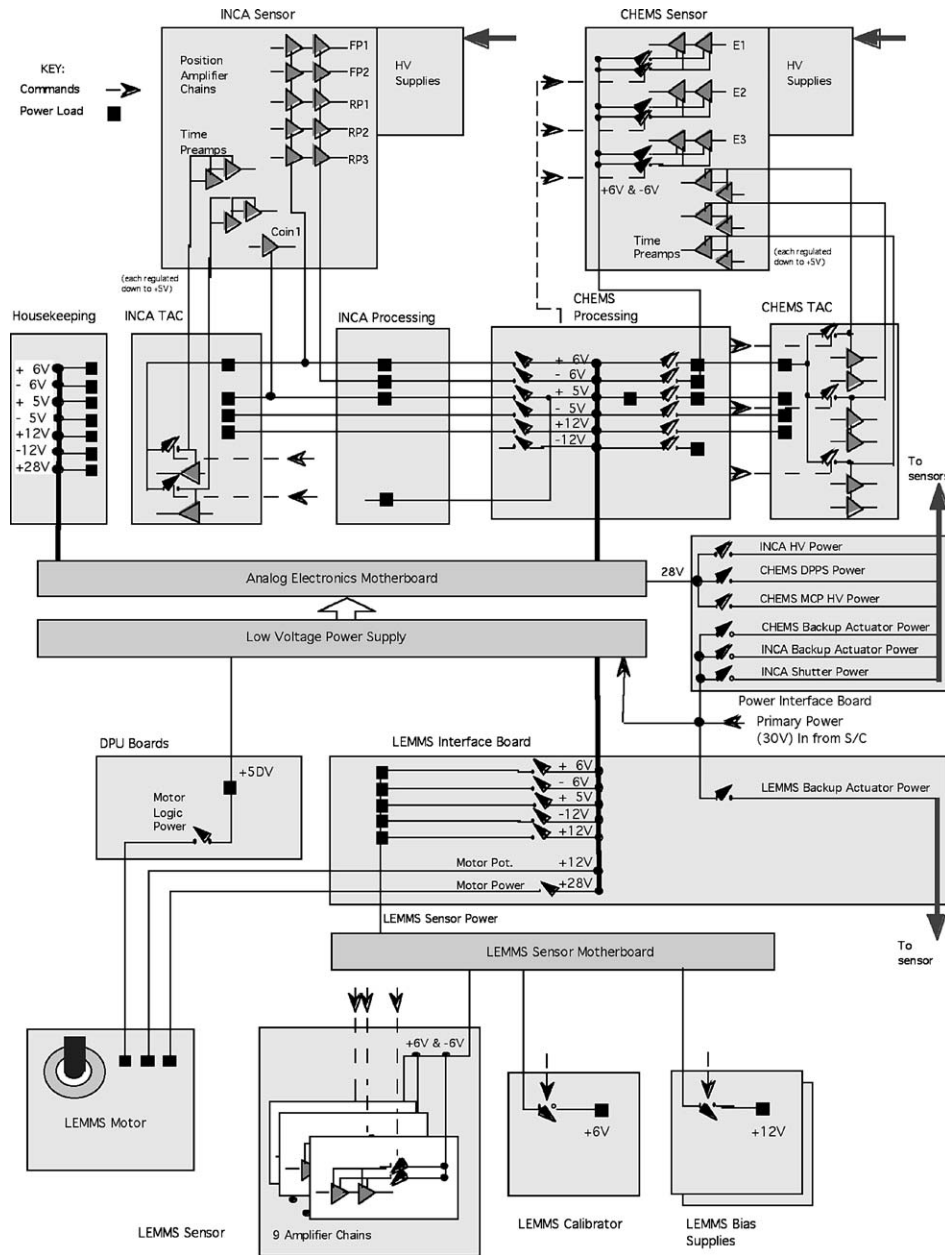


Figure 52. MIMI electronics power distribution.

detected. No pile-up detection is performed during the TOF event analysis. The INCA TAC board additionally has commandable input thresholds to help discriminate against UV-generated counts. The TOF calibrator circuitry is also on this board.

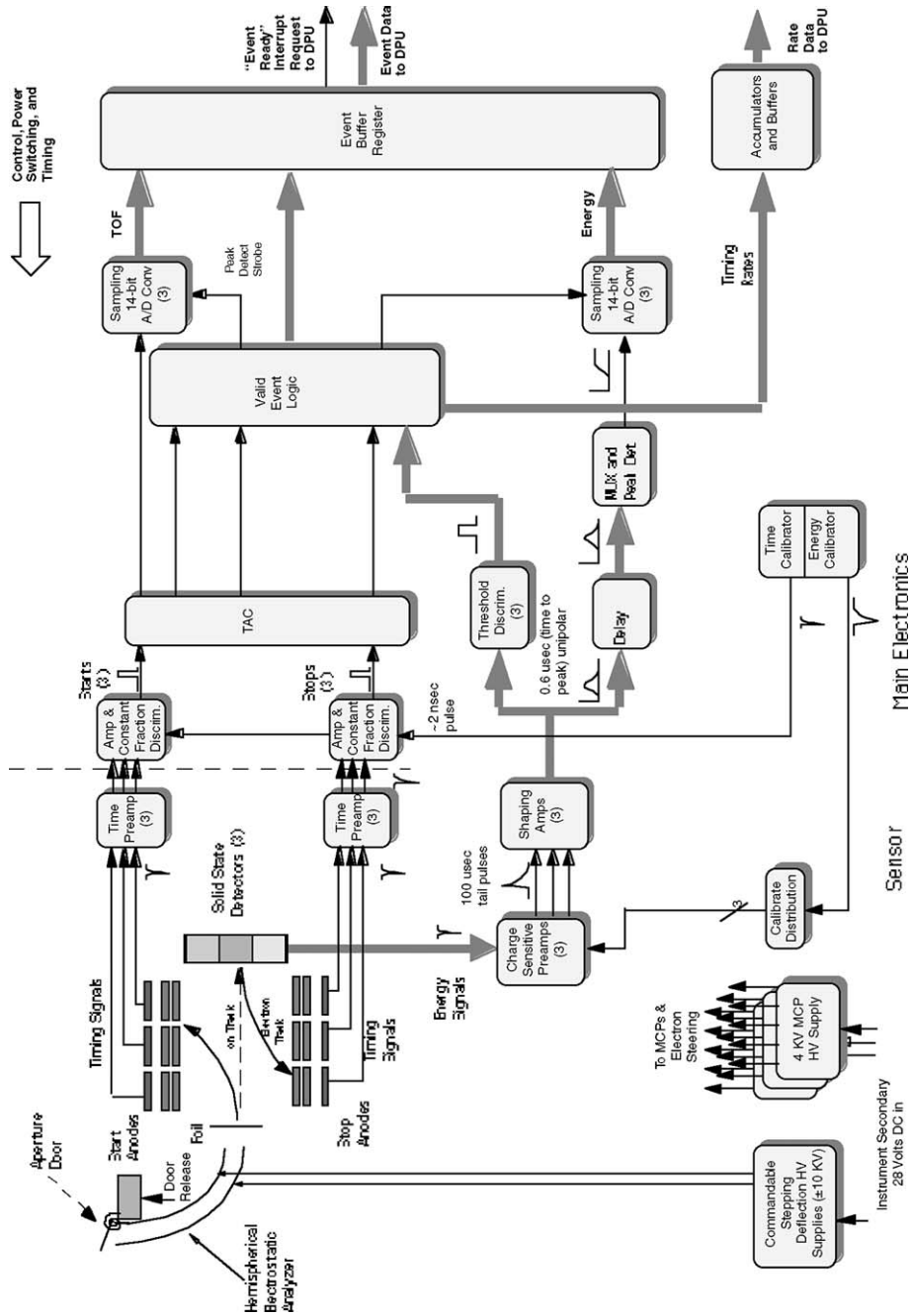


Figure 53. CHEMS subsystem block diagram.

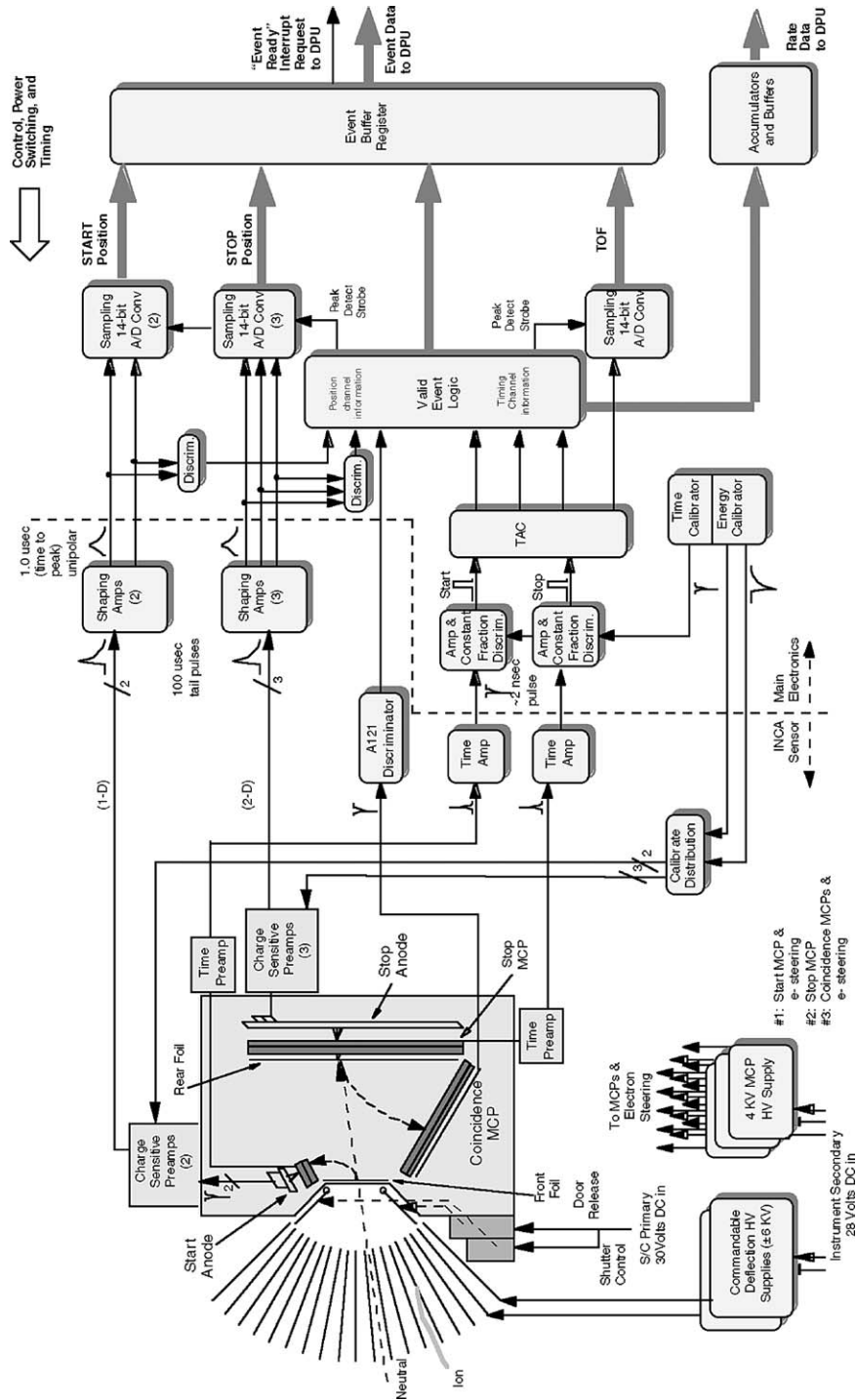


Figure 54. INCA block diagram.

The INCA processing board is very similar to the CHEMS processing board, but with the energy channel electronics replaced with five shaped, unipolar (1000 ns to peak) “position” channels: two shaped pulses come from the one-dimensional Start MCP anode and three shaped pulses come from the two-dimensional Stop MCP anode. These pulses represent the detected charge distribution on the START and STOP position-sensitive anodes, and will be used in the DPU to calculate the particle trajectory in iteration and azimuth angle. If valid event criteria are met, the position and TOF pulse amplitudes are then converted to digital values and stored for retrieval by the DPU. The typical event criteria for INCA are a valid TOF, start position, stop position, and coincidence signal all detected within approximately 100 ns of each other. Composite rates, coincidence MCP count rates, and individual TOF rates are accumulated in hardware counters for periodic retrieval by the DPU.

The housekeeping board handles most of the general status setting and monitoring for MIMI. Analog measurements are made for supply voltages (low- and high-voltage) and currents, instrument temperatures, and the LEMMS motor position. Analog references are provided for setting thresholds, calibrator pulse-heights, and high-voltage power supply (HVPS) levels. Digital outputs provide power switch-enables, HVPS enables, and digital references for the TOF calibrator and the CHEMS deflection plate power supply.

The LEMMS subsystem, as shown in Figure 55, is fairly self-contained; no LEMMS hardware is contained within the MEU. A detailed description of LEMMS can be found in Section 3.3.

#### 3.4.3. *Data Processing Unit (DPU)*

The DPU (right side of Figure 50) is responsible for all instrument control, data analysis, command, and telemetry functions. It is comprised of six boards: the control processing unit (CPU), the event processing unit (EPU), the support board, the bus interface unit (BIU), the BIU filter, and the DPU motherboard. The CPU, EPU, and support board are mounted into the motherboard, and make up the heart of the DPU. The BIU and its power filter are mounted directly to one of the MEU walls; they interface to the motherboard via a dedicated cable.

The CPU and EPU share an identical board design. Each has a Harris RTX 2010RH processor running at 6 million instructions/s, 192 kb of rad-hard SRAM, rad-hard PROM (8 kb for the CPU, 4 kb for the EPU), and 64 kb of rad-tolerant EEPROM. An additional 832 kb of rad-hard SRAM and 64 kb of rad-tolerant EEPROM is provided for each processor on the support board. In addition to providing this bulk memory to the processors, the support board also contains dedicated FIFO circuitry through which the EPU and CPU communicate, and FPGA-based interfaces for the LEMMS motor, LEMMS data, and the BIU. The BIU board, designed and built at JPL, provides redundant physical and logical interfaces to the spacecraft MIL-STD-1553 data bus.

The CPU and EPU are each dedicated to different hardware interfaces and tasks. The EPU only handles processing for the INCA and CHEMS events, and



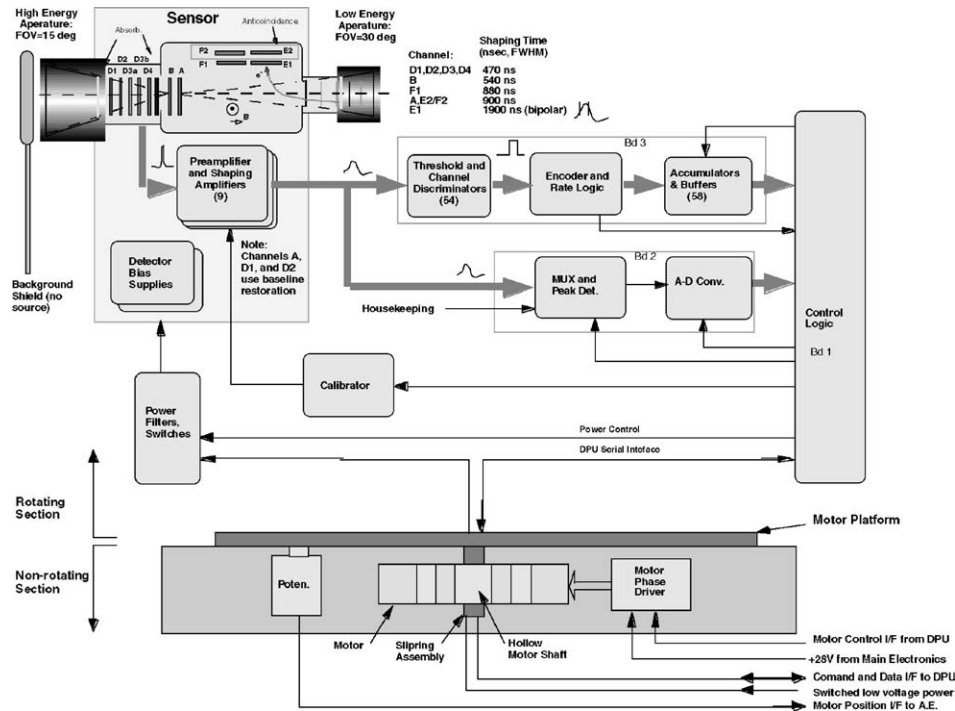


Figure 55. MIMI LEMMS subsystem block diagram.

is slaved to the CPU for all command and timing interfaces via the support board FIFOs and dedicated control lines. The EPU communicates with the INCA and CHEMS TAC and ADC boards and the support board. The CPU handles all other instrument tasks. It communicates with the housekeeping board, the LEMMS serial and motor interfaces, and the BIU interface. Since each processor can access only a portion of the instrument hardware interfaces, both are required to fully operate the instrument.

The BIU handles all 1553 communications, and communicates with the CPU via a dual-port 8 kb SRAM. When command and telemetry data are written to assigned memory locations within this SRAM, hardware flags are automatically set to indicate that data is available for pickup. The BIU has two dedicated digital I/O ports that the spacecraft can directly control/read without the CPU's participation. These lines provide the spacecraft the capability to provide high-level command/control lines to the instrument that are not dependent on the instrument processor itself. In MIMI, these lines are used to enable high voltage operation, reset the processors, enable the watchdog timers, and request the "SLEEP" mode. Status tell-tales also let the BIU monitor the DPU boot process to aid in possible fault analysis. A 9720  $\mu$ F capacitor bank is connected to the BIU +5 V supply line to filter out the large transients generated when the BIU is transmitting data over the 1553 bus.

*DPU Software.* Software for both the EPU and CPU is written in the Forth language, which is directly executable by the RTX processors. Flight code is normally stored in the processor's EEPROM memories, and is loaded 10 s after a processor reset or POR. A copy of the flight code is also stored in the spacecraft's SSR, which could be used if the EEPROM were to fail. New code will normally be written to the SSR, then downloaded to the processor memory, but it may also be loaded directly from the ground if necessary.

The CPU operating system is multitasking, which enables the processor to handle its large number of diverse tasks based on a priority basis. Command and hardware interface processing are of highest priority, followed by telemetry processing and image compression. The EPU operating system is non-multitasking, since it only handles a limited number of processes. Events from INCA and CHEMS are buffered in separate software FIFOs, which are then polled in a round-robin fashion, thus insuring that neither sensor can monopolize the EPU processing. As implemented in the software at launch, each INCA event requires (200  $\mu$ s to process, while each CHEMS event requires (135  $\mu$ s to process; we plan to speed this processing in later software versions.

To maximize the throughput of events in the system, the EPU is responsible only for the INCA and CHEMS event collection, processing, binning, and image cropping. The CPU takes this data (at spin/sector boundaries) and further processes it. The resulting CHEMS and INCA data is then formed into suitable telemetry packets.

There are several sources of computational dead-time in the EPU. When data is transferred between the EPU and CPU on microsector, subsector, sector, and quadrant boundaries, the normal EPU data collection is halted. The largest dead-times will be on sector and quadrant boundaries when INCA high-time resolution and low-time resolution images are transferred. A more significant source of dead-time is the image motion compensation (IMC) calculations performed by the EPU once every subsector. This results in a total dead-time of up to 0.6 s while in the "Staring Mode," and 0.07 s while in the "Spin Mode." The IMC dead-time applies only to event processing, however; new events will still be added to the software FIFOs (up to their 256 event limit).

*Command Functions.* The DPU command processing is very flexible. Normal commands and memory loads are transferred to the instrument on an immediate or time-delayed basis via the spacecraft CDS. Commands for MIMI are sent from the spacecraft over the 1553 bus. Each command is comprised of one or more 16-bit words, where the MSB of the first command word is a unique opcode. All commands have a fixed length (except for IEB\_LOAD). A flight rule restricts normal commanding to no more than one command per second to reduce possible command errors; memory loads are transferred at rates up to 1280 16-bit words/s from the SSR.

The instrument has the ability to store and run two different types of command sequences. The first type, known as macros, represent quasi-permanent sequences

used for instrument control functions that are not expected to change. Most instrument alarm responses and the LEMMS motor maintenance procedures are stored as macros. The second type, known as instrument expanded blocks, or IEBs, represent temporary sequences that are used for instrument orbital operations. IEBs are created and compiled on the ground using GSE software. A dedicated set of instrument commands is used to load, manage, and trigger IEBs in the DPU memory. Normally the trigger commands will be integrated into the spacecraft activity timeline, thus synchronizing a set of predefined MIMI science operations with the overall spacecraft activity plan.

#### 3.4.4. MIMI Operational Modes and Controls

*Operational Modes.* The instrument has a large number of operating modes, given that the three sensors may be commanded to a number of different configurations and individually enabled or disabled. Of this superset, however, a small subset has been chosen as standard operating modes, as shown in Figure 56:

*POR Mode:* This is the mode that is entered when the instrument is first turned on or reset. Only the DPU and housekeeping boards will be active; analog and sensor power will be off.

*FULL Mode:* This is the standard operating mode of the instrument. All three sensors are power and active, high voltages are at their operational levels, and the LEMMS motor is rotating; only the INCA shutter and the electronic calibrators are off.

*SLEEP Mode:* This mode is used to temporarily reduce the instrument power consumption, thus allowing the spacecraft to time multiplex instrument operations. When activated, this mode will turn off the LEMMS motor, the INCA shutter, all INCA and CHEMS amplifier, calibrator, and processing electronics, and will command the EPU to a slower clock speed. When this mode is exited, the former state of the electronics will be resumed. Note that all high voltages and LEMMS sensor power are unaffected.

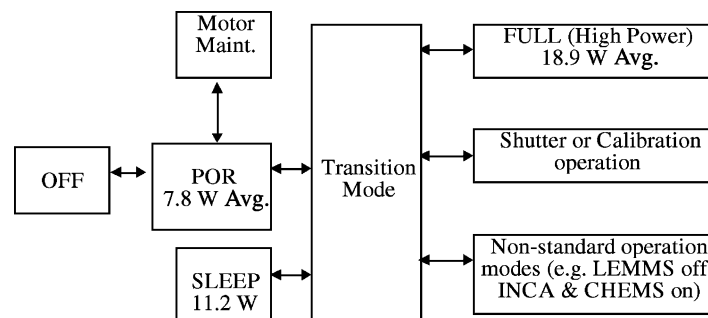


Figure 56. MIMI power states.

MIMI can also be commanded to store several different instrument configurations for later recall. This can be used to switch between standard operating modes during the mission with only a few commands.

*Fault monitoring and protection.* The DPU monitors the instrument operation via both digital and analog status data. All instrument temperatures, secondary voltages and several secondary currents are measured parameters.

*In-flight calibration.* The CHEMS and INCA sensors share an electronic calibration circuit, located in the MEU, which provides predefined energy and timing stimuli to the processing electronics.

The LEMMS sensor contains a similar circuit to provide energy stimuli to its processing electronics. The MIMI DPU will control the calibrator levels and sequencing; the calibrators will be powered off during nominal instrument operation. It should be noted that the CHEMS/INCA calibrator use is limited due to a known electronics flaw.

The INCA shutter, thermostatically driven by a coil-wound bimetallic spring heated with a 1.5-W heater, requires approximately 15 min to open or close. When the shutter is closed, the sensor will see counts from two AM-241 sources, each 0.075  $\mu\text{Ci}$ , producing 5.4 MeV  $\alpha$  particles as well as 60 keV X-rays.

*Thermal control.* The thermal design of MIMI is tightly coupled to that of the spacecraft. All four subassemblies are conductively mounted to the spacecraft structure, and their bulk thermal performance is largely determined by the overall spacecraft temperatures. The INCA collimator assembly is thermally isolated from the rest of the sensor, however, to limit radiation losses. The rotating section of LEMMS is not thermally coupled well to the spacecraft, due to the limited mechanical contact through its motor bearings. The sensor electronics or a replacement heater is always on to insure that the sensor temperature does not drop too low. Instrument temperatures are independently measured by both the spacecraft and the MEU.

#### 4. Data and Image Processing

Because of the high sensitivity and high angular, energy and time resolution of the three MIMI sensors, continuous transmission of the raw data would require impossibly large bit rates. So, extensive onboard data processing and data compression is a fundamental aspect of the MIMI experiment. The MIMI flight software has been designed to meet the scientific requirements of the mission even in limited data transmission allocation conditions. A variety of data products have been defined, each corresponding to a virtual instrument, and a combination of them is transmitted to the telemetry.

All MIMI data acquisition and processing is synchronized to an internally generated "sector clock," which when the spacecraft is in spinning mode is synchronized to the spacecraft rotation. One spacecraft rotation is divided into 16 sectors, each

sector thus corresponding to  $22.5^\circ$  of spacecraft rotation. Each sector is then subdivided into 16 subsectors, and each subsector into 16 microsectors. For the nominal spacecraft spin period, which is  $\sim 23$  min, a sector corresponds to  $\sim 86.2$  s, a subsector to  $\sim 5.4$  s, and a microsector to  $\sim 0.34$  s. These values are updated at the beginning of each sector, by taking into account the most recent spin rate information transmitted by the spacecraft AACS. This allows the MIMI sectoring scheme to adapt to spacecraft spin-ups and spin-downs. When the spacecraft is in a staring mode, the same MIMI sectoring scheme is still applied, but now the sector duration is a fixed parameter value, that mimics spacecraft rotation. Transition between the two modes, i.e. staring or spinning, is performed automatically, by monitoring the spacecraft spin rate data transmitted by the AACS.

The MIMI instrument incorporates two 16-bit RTX 2010 processors; the control processing unit handles all instrument command, telemetry, and control tasks, as well as the LEMMS data collection. The event processing unit is dedicated to collecting and processing the raw INCA and CHEMS data.

INCA image data are organized in three different image groups, simultaneously generated: high spatial resolution images, acquired over four sectors; high time resolution images, acquired each sector; and high time-of-flight and mass resolution images, acquired over four sectors (Figure 57).

The EPU collects data from the INCA instrument, generates the images, performs image motion compensation (by taking into account the spacecraft attitude data, correcting thus for spacecraft mosaic-like attitude motion), and sends the images to the CPU. The images are then compressed by the CPU and sent to the telemetry. A double buffering process is used in order to acquire an image set in the EPU in parallel with the processing of the previous instrument cycle image set in the CPU. The INCA image types generated in neutral (ENA) mode are also shown in Table XIX.

TABLE XIX  
INCA image types generated in neutral (ENA) mode.

	Number of images	Image accumulation period	Pixels/image	Memory pixels/image
High spatial resolution Low TOF	3	4 sectors	$64 \times 64$	$128 \times 96$
High spatial resolution High TOF	3	4 sectors	$32 \times 32$	$64 \times 48$
High time resolution Low TOF	1	1 sector	$32 \times 32$	$64 \times 48$
High time resolution High TOF	1	1 sector	$32 \times 32$	$64 \times 48$
High <i>m</i> -TOF resolution: (neutral mode)	$5 \times 8$	4 sectors	$16 \times 16$	$32 \times 24$

### INCA Image Planes: Neutral Mode

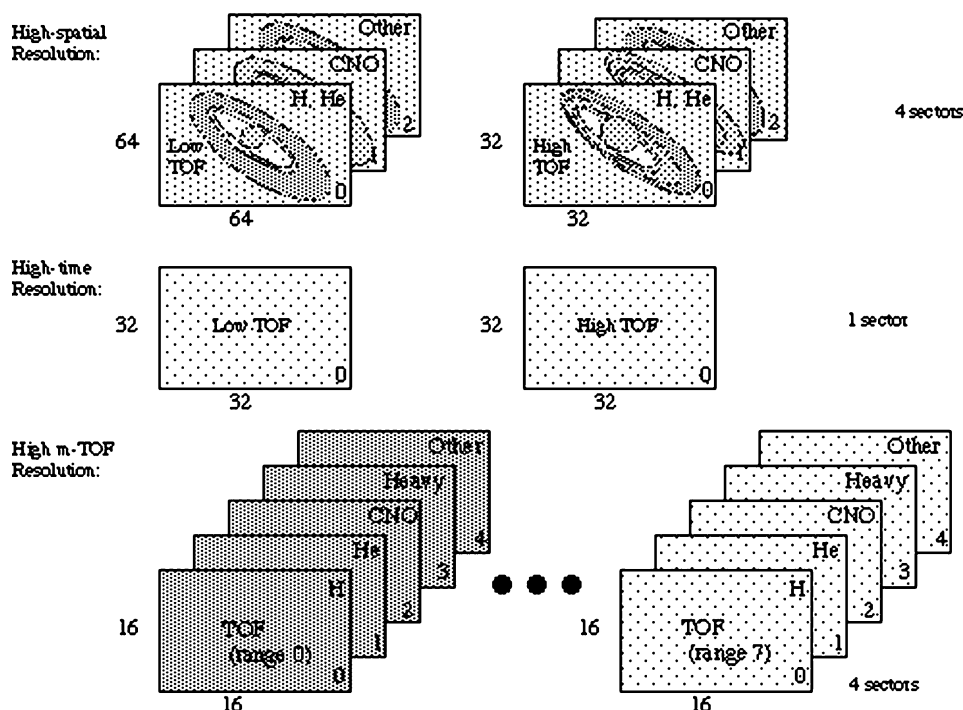


Figure 57. INCA images.

The INCA images must be compressed in order to fit into the available telemetry allocation. The data compression is a four-step process: event binning, selection of the “useful” part of the image, logarithmic compression, and “real” image compression.

Event binning, and organization of the image data into the scheme shown in Table XIX, results in a preliminary data compression by a factor of  $\sim 20$ . As shown in the table, every four sectors INCA generates three  $64 \times 64$  pixel images (high spatial resolution), eleven  $32 \times 32$  pixel images (eight high time resolution and three high spatial resolution images) and forty  $16 \times 16$  pixel images (high TOF/mass resolution). This corresponds to an average of  $\sim 98$  pixels/s. Without the implementation of such a binning scheme, a single set of images would be generated, providing the full spatial, time and  $m$ -TOF resolution, i.e.  $5 \times 8$  images,  $64 \times 64$  pixels each, generated every one sector. This would have required an average of  $\sim 1900$  pixels/s.

Selection of the “useful” part of the image results in the reduction of the initial  $180^\circ \times 180^\circ$  equivalent FOV, allocated in the DPU memory, to the  $90^\circ \times 120^\circ$  image sent to the telemetry. At the start of image integration each  $180^\circ \times 180^\circ$

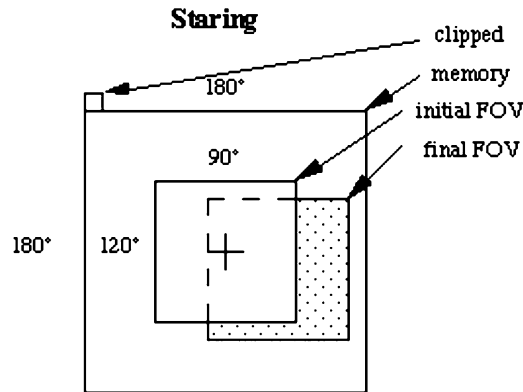


Figure 58. INCA image integration in stare mode.

image buffer is centered with INCA's FOV (Figure 58). As the spacecraft moves, the FOV can move and rotate within the image buffer, image motion compensation taking into account for that. Nevertheless, at the end of the image accumulation, only the  $90^\circ \times 120^\circ$  part of the image, i.e. equal to the INCA instantaneous field of view (corresponding to the most exposed part of the  $180^\circ \times 180^\circ$  image) is sent to the telemetry. This corresponds to a data reduction factor of 3.

Logarithmic compression of the accumulated counts is then performed by the CPU on each pixel (except during the very high bit rate), and results in a 16–8-bit compression. This is lossless only for the first 32 values, but the maximum relative error does not exceed 3.1%.

"Real" image compression is then performed by the CPU, and it is a lossless Rice or Fast compression. The compression algorithm is selected via uplink command, and its use is flagged in the downlink data stream as a header variable. The Fast algorithm is an encoding scheme that examines a block of  $J$  pixels and finds the maximum pixel value in the block. It then calculates the minimum number of bits required to code this maximum value. Each pixel of the block is then represented using only this smaller number of bits. A block header is required for each block, that contains the value used for encoding the pixels in the block. The Rice algorithm is based on using a Comma code. The Comma code for any positive integer,  $k$ , is simply  $k$  leading zeroes followed by an ending "1." As in the Fast encoder, the data are processed in a  $4 \times 4$  pixel block at a time. The Rice algorithm considers the block values as containing a certain number,  $m$ , of incompressible least significant bits (lsbs). These lsbs are stripped off of each block value and saved. The Rice algorithm must determine the best value for  $m$ , and the number of lsbs to strip off for each block of data, so that the overall code length of the encoded block is minimized. The remaining most significant bit values (msbs) are then Comma encoded. Both Rice and Fast algorithms have been tested on a test image set, generated from

simulated INCA images, as the one shown in Figure 12, in which instrument noise was then introduced in order to examine the noise effects on the image entropy and the compression factor.

Compressed images are then organized in telemetry subpackets, each subpacket corresponding to a self-contained part of the parent image, including the necessary header information. It should be noted that image compression is performed within the image part corresponding to each subpacket. This allows decompression of each subpacket independently, so as to allow reconstruction of correct partial images in case of loss of some subpackets. INCA image subpackets (and all other MIMI science data product subpackets) are inserted into the fixed-length MIMI science packets, and are transmitted to the spacecraft solid-state recorder (SSR).

Other MIMI data products include:

- INCA and CHEMS accumulator rates, which are periodic readouts of the hardware accumulators in these instruments (9 INCA accumulators and 17 CHEMS accumulators). These are subject to a 24–10 bits logarithmic compression.
- INCA and CHEMS PHA events, which correspond to the complete information on the subset of the particles detected by these two instruments. For INCA this includes: TOF, pulse-height of the signal output from the front and rear MCPs, MCP identification (coincidence, start/stop), calculated azimuth and elevation, and mass range. For CHEMS it includes: TOF, pulse-height of the signal output from the SSD, MCP, and SSD identification, deflection voltage (DPPS) step, and calculated range (one of seven basic rates, each one being a subdivision of the  $m - m/q$  space).
- CHEMS basic rates and science rates, i.e., total number of detected ions corresponding to each of the 7 basic rates and 34 science rates, measured for each DPPS step. These are subject to a 16–8 bits logarithmic compression.
- LEMMS accumulator rates, which are periodic readouts of the 57 normal counters and the 4 priority counters, each corresponding to a different particle, energy, or species range. These are subject to a 24–10 bits logarithmic compression.
- LEMMS PHA data, corresponding to the periodic readout of 64 energy channels  $\times$  3 detectors and are subject to a 16–8 bits logarithmic compression.

Table XX gives an overview of the MIMI science data products and of the periodicity of their transmission to the telemetry stream. Note that during spinning mode, INCA 16-sector images, corresponding to a  $360^\circ$  azimuthal FOV, are transmitted to the telemetry as four separate  $90^\circ$  azimuthal FOV images, each one accumulated over a 4-sector period.

In addition to the above INCA, CHEMS and LEMMS sensor data products, the MIMI science telemetry stream also includes some auxiliary data, such as LEMMS



TABLE XX  
Overview of MIMI science data products.

	Staring		Spinning	
	Neutral	Ion	Neutral	Ion
INCA				
High spatial resolution images	4 sectors	—	16 sectors*	—
High time resolution images	1 sector	1 sector	1 sector	1 sector
High <i>m</i> -TOF resolution Images	4 sectors	1 sector	16 sectors*	1 sector
PHA events	4 subsectors			
Accumulator rates	1 subsector (# of events varies with telemetry mode)			
CHEMS				
Science rates	1 subsector (2 subsectors in <i>Very Low Bit Rate</i> )			
Accumulator rates	1 subsector			
Basic rates	1 subsector (2 subsectors in <i>Very Low Bit Rate</i> )			
PHA events	1 sector (# of events varies with telemetry mode)			
LEMMS				
Accumulator rates	4 “priority” counters: 2 microsectors			
	60 remaining counters: 16 microsectors			
	(32 in <i>Very Low Bit Rate</i> )			
PHA events	1 subsector in <i>Very High Bit Rate</i> and <i>High Bit Rate</i>			
	2 subsectors in <i>Medium Bit Rate</i>			
	4 subsectors in <i>Low Bit Rate</i>			
	8 subsectors in <i>Very Low Bit Rate</i>			

turntable rotation data, spacecraft attitude data, MIMI instrument status data, etc.

The MIMI science packet and subpacket headers have been designed to include all the necessary information for data and mode identification, decompression, and time tagging, while minimizing the overhead to the telemetry bit rate. This overhead is about 2.4%, including the standard CCSDS and Cassini project packet headers.

A flexible scheme has been implemented in order to optimally match the limited SSR allocation and the variable compression rates, while transmitting the maximum amount of information possible. Five telemetry rates have been defined for each of the three MIMI sensors: very high bit rate, high bit rate, medium bit rate, low bit rate, and very low bit rate (cf. also Table XX). Each 24-h period, corresponding to an SSR allocation, has been divided into a series of “observation periods,” and a default telemetry rate is programmed by uplink command for each of the

three sensors and for each observation period. The higher telemetry rates can thus be programmed for the orbit sections corresponding to satellite flybys, flux tube crossings, etc. The MIMI DPU monitors the science packet data volume sent to the spacecraft SSR during each observation period. If this volume exceeds a pre-defined threshold, the sensors automatically switch to a lower than the default programmed bit rate for the next observation period, so as to avoid an early saturation of the SSR partition allocated to MIMI. But if the monitored data volume is lower than anticipated, then for the next observation period the sensors switch to a higher than the default programmed bit rate, thus making optimum use of the SSR partition.

### **5. Toward Accomplishment of Science Goals**

The unprecedented capabilities of the MIMI investigation, coupled with the comprehensive nature of the overall Cassini mission, will result in an epochal change in our understanding of the space environment of the Saturnian system. A summary of the measurement advances that the MIMI investigation will make over previous measurements would include: (1) the first global magnetospheric imaging of the hot ion populations of the Saturnian magnetosphere, Titan and possibly icy satellite exospheres, and dust interactions within the inner magnetospheric regions; (2) unambiguous composition analysis of hot ions, critical for ascertaining plasma sources, and the first measurement of charge state distributions, critical for the study of processes, such as charge exchange, that fractionate the compositional distributions; and (3) much more comprehensive in-situ angular coverage and finer angular resolutions, critical for calculating the charge particle invariant quantities that order the transport of hot plasma populations. These instrumental advances must be added to the advances that will accrue simply from the fact that the Cassini is an orbital mission, allowing a comprehensive in-situ survey of all of the critical regions of the Saturnian system. We have emphasized in this paper that the energetic charged particle populations interact strongly with other components of the Saturnian space environment, including Saturn's atmosphere, the rings and dust particulates, neutral gas populations, icy satellite surfaces, and Titan's atmosphere. When the advanced capabilities of the MIMI investigation are combined with other measurements, our understanding of these interactions will also increase dramatically.

Table XXI summarizes the anticipated accomplishments of the MIMI investigation. It lists the major science objectives, the observations required for those objectives, and the results expected. Needless to say, such a table must be limited in scope. There is not the space here to discuss the rich array of possible multi-instrument studies involving MIMI and all of the other advanced instrumentation that is flying with the Cassini mission.

TABLE XXI  
Expected accomplishments of the MIMI investigation.

Objective	MIMI product	Interpretation
Global morphology of Saturn's magnetosphere	ENA images (remote), orbital intensity survey (in-situ)	Direct views of remote images; image inversion; combine with UVIS neutral gas images; orbital data assimilation statistics and models
Plasma source(s)	Composition and charge state distributions, energy spectra	Species identification; ionization states; source process modeling; analysis of CRAND spectral features
Plasma energization	Energy spectra (in-situ); pitch angle distributions (in-situ); ENA images (remote)	Location and evolution of energization events; spatial and temporal evolution of spectra
Global dynamics and possible substorms	ENA images (remote); orbital intensity survey (in-situ)	Direct views of remote images; image inversion; orbital data assimilation and orbit-to-orbit comparisons
Plasma convection	Ion angular distributions (in-situ)	Quantitative plasma flow analysis
Hot plasma and radiations transport	Phase space densities (in-situ); intensity profiles (in-situ); ENA dust interaction image (remote)	Diffusion theory analysis of phase space densities; material interaction feature evolution analysis (e.g. satellite macro/micro signatures), dust interaction modeling
Saturnian aurora energy source	ENA images (remote); orbital survey of electron and ion spectrum moments (in-situ), phase space densities	Correlate hot plasma dynamics with auroral dynamics; quantitative analysis of electron and ion energy precipitation limits; pitch angle diffusion analysis.
Hot plasma/Saturnian atmosphere interactions	Composition spectra (in-situ)	Identification of atmospheric species by location
Hot plasma/satellite and ring interactions	ENA images (remote); intensity profiles, phase space densities, composition spectra (in-situ)	Quantitative ENA intensity analysis of dust emissions; micro/macrosignature transport analysis; species identification; quantitative surface deposition sputtering calculations
Titan remote monitoring of magnetospheric dynamics	Remote ENA images of Titan	Analysis of position of magnetopause based on the intensity of Titan ENA emissions
Jovian science	ENA images (remote), ion composition and charge state distributions (in-situ)	Images analysis and sorting by various system drivers (solar wind, Jupiter rotation, Io position, etc.); composition source analysis; analysis of charge state in context of hot plasma transport models.

## 6. Summary

It is beyond doubt that the Cassini orbiter mission to Saturn will increase manyfold our knowledge of the overall Kronian system, beginning with the rings, Titan, icy moons, magnetosphere, atmosphere, aurora, dust environment, etc. If any proof were needed, it has been provided by the spectacular Galileo results from the Jovian system and the preliminary results from Cassini's flyby at Jupiter.

The MIMI investigation is designed to make key contributions to each of the subjects enumerated above, using an array of sensors that will provide comprehensive measurements of the hot plasmas in Saturn's environment with unprecedented resolution in energy and species. Furthermore, MIMI's ability to image plasmas indirectly, through their ENA emissions, represents a heretofore unreachable objective of space plasma research that has long eluded instrument designers in this field. It has been amply demonstrated on the IMAGE mission in Earth orbit (Mitchell *et al.*, 2001). This new capability opens up a large class of studies on plasma dynamics that may enable us to not only address long-standing unsolved questions (e.g., substorm initiation and development) in magnetospheric physics, but also lead to radically new insights on the large-scale structures and evolution of such systems.

The in-flight performance of the instrument has been nominal so far, and we expect that to continue through Saturn orbit insertion and the 4-year encounter operations. The comprehensive orbiter payload will make possible a large array of collaborative studies that guarantee an exciting harvest of scientific results.

## Acknowledgments

We are grateful to a great number of people who contributed to the hardware effort for MIMI at the institutions central to the activity, namely, the Johns Hopkins University Applied Physics Laboratory (JHU/APL), the Department of Physics at the University of Maryland, the Max-Planck-Institute für Aeronomie (MPAe), and Centre d' Etude Spatiale des Rayonnements (CESR), in Toulouse. At JHU/APL the assistance of personnel in the Technical Services Department made possible the timely layout and fabrication of INCA and the MEU. In the Space Department key contributions were made by several people, among whom are J. Heiss, Dr. N.P. Paschalidis, R.E. Thompson, and S.R. Vernon. The CHEMS sensor was developed by the space physics group in the Department of Physics at the University of Maryland. Many individuals contributed to its design, development, fabrication, testing, and calibration over the years 1991–1997. We are particularly grateful to the following individuals: Paul Wilson IV, Jeff Rizza, Edvin Tums, Richard Pappalardo, Maurice Pairel, Pota Floros, Scott Lasley, Wayne Shanks, George Ho, and Joseph Zanelotti. The success of the LEMMS sensor at MPAe owes much to the excellent work of W. Boeker, B. Goll, K. Heerlein, H.G. Kellner, Dr. A. Lagg, A. Loose, O. Matuschek, H. Sommer, and W. Tappert. We would also like

to thank the team from VTT Automation Space Technology under the lead of K. Viherkanto for an excellent job in building the turntable. Many thanks also to the staff from the Institut für Geophysik und Meteorologie at the Technical University of Braunschweig for LEMMS internal magnetic field measurements. Thanks to Prof. Treusch, Dr. R. Maier, Dr. F. Dworschak, W. Brautigam and Dr. Protic and their teams from the Kernforschungszentrum Jülich, Germany; the people from the 88-inch cyclotron of the Lawrence Berkeley Laboratory; Drs. B. Blake and M. Looper from the Aerospace Corporation in providing excellent beam facilities and help during instrument calibration. We especially acknowledge the work in the design of LEMMS by our colleague B. Wilken who unfortunately died in 2001, 3 years before Cassini's arrival at Saturn. We will miss him as a very knowledgeable scientist and friend. The contributions to the DPU of personnel at CESR, including those of M. Gangloff and N. Casajus, with key assistance from T. Psomoulis of Democritos University of Thrace are appreciated with thanks. Important contributions were also made by personnel at the University of Arizona (foils) and the University of Kansas (LEMMS design). The dedicated work of S. Brown and C. Smith in operating the Goddard Space Flight Center accelerator was instrumental to the successful calibrations of all three MIMI detector systems. Finally, we are most grateful to the JPL project personnel, including R. Spehalski, T. Gavin, W.G. Fawcett, D. Matson, J. Feynman, M. Burton, and S. Bolton for their assistance in various phases of the program. The MIMI program at JHU/APL was supported by the NASA office of Space Science under Task I of contract N00024-97-C-8119 between the Johns Hopkins University and the Department of the Navy, and by sub-contract at the Universities of Maryland, Kansas, and Arizona. Mission operations and data analysis are supported under Task Order 003 of contract NAS5-97271 between the NASA/GFSC and the Johns Hopkins University. The German part of LEMMS at MP Ae was financed by the Bundesministerium für Bildung und Forschung (BMBF) through the Deutsches Zentrum für Luft und Raumfahrt e. V. (DLR) under contract no. 50 OH 93028. The work at CESR was supported by CNES.

## References

- Amsif, A.: 1996, *Etude et modélisation de la production d'atomes énergétiques neutres dans l'exosphère de Titan*, Ph. D. Thesis, P. Sabatier University, Toulouse, France.
- Amsif, A., Dandouras, J., and Roelof, E. C.: 1997, *J. Geophys. Res.* **102**, 22169.
- Barbosa, D. D.: 1987, *Icarus* **72**, 53.
- Barbosa, D. D. and Eviatar, A.: 1986, *Astrophys. J.* **310**, 927.
- Barbosa, D. D., Eviatar, A., and Siscoe, G. L.: 1984, *J. Geophys. Res.* **89**, 3789.
- Baron, R. L., Owen, T., Connerney, J. E. P., Satoh, T., and Harrington, J.: 1996, *Icarus* **120/122**, 437.
- Barrow, C. H. and Desch, M. D.: 1989, *Astron. Astro. Phys.* **213**, 495.
- Belcher, J. W.: 1983, in: Dessler, A. J. (ed.), *Physics of the Jovian Magnetosphere*, Cambridge University Press, Cambridge, UK and New York, p. 68.

- Broadfoot, A. L., Sandel, B. R., Shemansky, D. E., Holberg, J. B., Smith, G. R., Strobel, D. F., McConnell, J. C., Kumar, S., Hunten, D. M., Atreya, S. K., Donahue, T. M., Moos, H. W., Bertaux, L., Blamont, J. E., Pomphrey, R. B., and Linick, S.: 1981, *Science* **212**, 206.
- Burns, J. A., et al.: 1994, *An Integrated Strategy for the Planetary Sciences: 1995–2010*, Report of the Committee on Planetary and Lunar Exploration, Space Studies Board, National Research Council, Washington, DC.
- Carbary, J. F. and Krimigis, S. M.: 1982, *Geophys. Res. Lett.* **9**, 420.
- Cheng, A. F.: 1986, *J. Geophys. Res.* **91**, 4524.
- Cheng, A. F. and Krimigis, S. M.: 1989a, *J. Geophys. Res.* **94**, 12003.
- Cheng, A. F. and Krimigis, S. M.: 1989b, in: Waite, J. H., Burch, J., and Moore, R. (eds.), *AGU Solar System Plasma Physics*, p. 253.
- Cheng, A. F., Keath, E. P., Krimigis, S. M., Mauk, B. H., McEntire, R. W., Mitchell, D. G., Roelof, E. C., and Williams, D. J.: 1993, *Remote Sens. Rev.* **8**, 101.
- Clarke, J. T., et al.: 1996, *Science* **274**, 404.
- Curtis, C. C. and Hsieh, K. C.: 1989, *AGU Solar Syst. Plasma Phys., Geophys. Monogr. Ser.* **54**, 247.
- Dandouras, J. and Amsif, A.: 1999, *Planet. Space Sci.* **47**, 1355.
- Desch, M. D. and Barrow, C. H.: 1984, *J. Geophys. Res.* **89**, 6819.
- Dessler, A. J.: 1983, *Physics of the Jovian Magnetosphere*, Cambridge University Press.
- Esposito, L. W., Cuzzi, J. N., Holberg, J. B., Marouf, E. A., Tyler, G. L., and Porco, C. C.: 1984, in: Gehrels, T., and Matthews, M. S. (eds.), *Saturn*, The University of Arizona Press, Tucson, p. 463.
- Eviatar, A.: 1992, *Adv. Space Res.* **12**(8), 367.
- Eviatar, A., Mekler, Y., and Coroniti, F. V.: 1976, *Astrophys. J.* **205**, 622.
- Fisk, L. A., Schwadron, N. A., and Gloeckler, G.: 1997, *Geophys. Res. Lett.* **24**, 93.
- Gehrels, T.: 1976, *Jupiter*, University of Arizona Press, Tucson, Arizona.
- Geiss, J., Gloeckler, G., Fisk, L. A., and von Steiger, R.: 1995, *J. Geophys. Res.* **100**, 23373.
- Geiss, J., Gloeckler, G., Mall, U., von Steiger, R., Galvin, A. B., and Ogilvie, K. W.: 1994, *Astron. Astrophys.* **282**, 924.
- Geiss, J., et al.: 1992, *Science* **257**, 1535.
- Gloeckler, G.: 1996, *Space Sci. Rev.* **78**, 335.
- Gloeckler, G. and Geiss, J.: 1998, *Space Sci. Rev.* **86**(1–2), 127–159.
- Gloeckler, G. and Geiss, J.: 1996, *Nature* **381**, 210.
- Gloeckler, G. and Hsieh, K. C.: 1979, *Nucl. Inst. Methods* **165**, 537.
- Gloeckler, G., Fisk, L. A., and Geiss, J.: 1997, *Nature* **386**, 374.
- Gloeckler, G., Balsiger, H., Bürgi, A., Bochsler, P., Fisk, L. A., Galvin, A. B., Geiss, J., Gliem, F., Hamilton, D. C., Holzer, T. E., Hovestadt, D., Ipavich, F. M., Kirsch, E., Lundgren, R. A., Ogilvie, K. W., Sheldon, R. B., and Wilken, B.: 1995, *Space Sci. Rev.* **71**, 79.
- Gloeckler, G., Jokipii, J. R., Giacalone, J., and Geiss, J.: 1994, *Geophys. Res. Lett.* **21**, 1565.
- Gloeckler, G., Geiss, J., Balsiger, H., Fisk, L. A., Galvin, A. B., Ipavich, F. M., Ogilvie, K. W., von Steiger, R., and Wilken, B.: 1993, *Science* **261**, 70.
- Goertz, C. K.: 1989, in: Waite, J. H., Burch, J. L., and Moore, R. L. (eds.), *AGU Solar System Plasma Physics, Geophysical Monograph Series Vol. 54*, p. 427.
- Gurnett, D. A., et al.: 1982, *J. Geophys. Res.* **87**, 1395.
- Hilchenbach, M. et al.: 1998, *Astrophys. J.* **503**, in press.
- Holzer, T. E.: 1977, *Rev. Geophys. Space Phys.* **15**, 467.
- Hsieh, K. C. and Curtis, C. C.: 1989, in: Waite, J., Burch, J., and Moore, R. L. (eds.), *AGU Solar System Plasma Physics*, p. 159.
- Hsieh, K. C. and Curtis, C. C.: 1988, *Geophys. Res. Lett.* **15**, 772.
- Hsieh, K. C., Shih, K. L., Jokipii, J. R., and Gruntman, M. A.: 1992a, *Astrophys. J.* **393**, 756.
- Hsieh, K. C., Shih, K. L., Jokipii, J. R., and Gruntman, M. A.: 1992b, in: Marsch, E., and Schwenn, R. (eds.), *Proceedings of the 3rd COSPAR Colloquium*, p. 365.

- Hsieh, K. C., Sandel, B. R., Drake, V. A., and King, R. S.: 1991, *Nucl. Inst. Methods* **B61**, 187.
- Hsieh, K. C., Keppler, E., and Schmidtke, G.: 1980, *J. Appl. Phys.* **51**, 2242.
- Ip, W. H.: 1997, *Icarus* **126**, 42.
- Ip, W. H.: 1996, *Astrophys. J.* **457**, 922.
- Ip, W. H.: 1992, in: *Proceedings of the Symposium on Titan*, Toulouse, France, ESA SP-338, p. 243.
- Ip, W. H.: 1990, *Astrophys. J.* **362**, 354.
- Ip, W. H.: 1984, *J. Geophys. Res.* **89**, 2377.
- Ip, W. H., Williams, D. J., McEntire, R. W., and Mauk, B. H.: 1998, *Geophys. Res. Lett.* **25**, 829.
- Ip, W. H., Williams, D. J., McEntire, R. W., and Mauk, B. H.: 1997, *Geophys. Res. Lett.* **24**, 2631.
- Ipavich, F. M., Lundgren, R. A., Lambird, B. A., and Gloeckler, G.: 1978, *Nucl. Inst. Methods* **154**, 291.
- Johnson, R. E.: 1990, *Energetic Charged Particle Interactions with Atmospheres and Surfaces*, Springer-Verlag, New York.
- Johnson, R. E., Pospieszalska, M., Sittler, E., Cheng, A. F., Lanzerotti, L. J., and Sieveka, E. M.: 1989, *Icarus* **77**, 311.
- Kaiser, M. L.: 1993, *J. Geophys. Res.* **98**, 18757.
- Kirsch, E., Krimigis, S. M., Ip, W. H., and Gloeckler, G.: 1981a, *Nature* **292**, 718.
- Kirsch, E., Krimigis, S. M., Kohl, J. W., and Keath, E. P.: 1981b, *Geophys. Res. Lett.* **8**, 169.
- Krimigis, S. M.: 1992, *Space Sci. Rev.* **59**, 167.
- Krimigis, S. M.: 1986, *Comparative Study of Magnetospheric Systems*, CNES, LEPADUE Editions, Toulouse, France, Vol. 99.
- Krimigis, S. M. and Armstrong, T. P.: 1982, *Geophys. Res. Lett.* **9**, 1143.
- Krimigis, S. M., Carbary, J. F., Keath, E. P., and Armstrong, T. P.: 1982a, *EOS* 1068.
- Krimigis, S. M., Armstrong, T. P., Axford, W. I., Bostrom, C. O., Gloeckler, G., Keath, E. P., Lanzerotti, L. J., Carbary, J. F., Hamilton, D. C., and Roelof, E. C.: 1982b, *Science* **215**, 571.
- Krimigis, S. M., Carbary, J. F., Keath, E. P., Armstrong, T. P., Lanzerotti, L. J., and Gloeckler, G.: 1983, *J. Geophys. Res.* **88**, 8871.
- Krimigis, S. M., Decker, R. B., Hamilton, D., and Gloeckler, G.: 2000, *AIP Conf. Proc.* **528**, 333–336.
- Krimigis, S. M., Zwickl, R. D., and Baker, D. N.: 1985, *J. Geophys. Res.* **90**, 3947.
- Krimigis, S. M., Mitchell, D. G., Hamilton, D. C., Dandouras, J., Armstrong, T. P., Bolton, S. J., Cheng, A. F., Gloeckler, G., Hsieh, K. C., Keath, E. P., Krupp, N., Lagg, A., Lanzerotti, L. J., Livi, S., Mauk, B. H., McEntire, R. W., Roelof, E. C., Wilken, B., and Williams, D. J.: 2002, *Nature* **415**, 994.
- Krimigis, S. M., et al.: 1988, *Planet. Space Sci.* **36**, 311.
- Krupp, N., Woch, J., Lagg, A., Wilken, B., Livi, S., and Williams, D. J.: 1998, *Geophys. Res. Lett.* **25**, 1249–1252.
- Lagg, Andreas: 1998, *Energierreiche Teilchen in der inneren Jupitermagnetosphaere: Simulation und Ergebnisse des EPD-Experimentes an Bord der Raumsonde GALILEO*, Dissertation, Max-Planck-Institut fuer Aeronomie, Lindau/Harz, Germany, MPAE-W-807-98-01.
- Lee, M. A.: 1982, *J. Geophys. Res.* **87**, 5063.
- Mall, U., Fichtner, H., Kirsch, E., Hamilton, D. C., and Rucinski, D.: 1998, *Planet. Space Sci.*, submitted for publication.
- Mauk, B. H. and Krimigis, S. M.: 1987, *J. Geophys. Res.* **92**, 9931.
- Mauk, B. H., Krimigis, S. M., Mitchell, D. G., Roelof, E. C., Keath, E. P., and Dandouras, J.: 1998, *Planet. Space Sci.* **46**, 1349.
- Mauk, B. H., Williams, D. J., and McEntire, R. W.: 1997a, *Geophys. Res. Lett.* **24**, 2949.
- Mauk, B. H., Williams, D. J., McEntire, R. W., Khurana, K. K., and Roederer, J. G.: 1999, *J. Geophys. Res.* **104**, 22759.

- Mauk, B. H., Krimigis, S. M., Mitchell, D. G., and Roelof, E. C.: 1998, *Adv. Space Res.* **21**, 1483.
- Mauk, B. H., Krimigis, S. M., and Acuña, M. H.: 1994, *J. Geophys. Res.* **99**, 14781.
- Mauk, B., Krimigis, S. M., and Lepping, R.: 1985, *J. Geophys. Res.* **90**, 8253.
- McEntire, R. W. and Mitchell, D. G.: 1989, in: Burch, J., and Waite, J. (eds.), *Outstanding Problems in Solar System Plasma Physics*, AGU Monograph.
- Meckbach, W., Braunstein, G., and Arista, N.: 1975, *J. Phys. B* **8**, L344.
- Mendis, D. A., Hill, J. R., Ip, W. H., Goertz, C. K., and Grün, E.: 1984, 'Electrodynamic processes in the ring system of Saturn', in: Gehrels, T., and Matthews, M. S. (eds.), *Saturn*, The University of Arizona Press, Tucson, p. 546.
- Mitchell, D. G., Hsieh, K. C., Curtis, C. C., Hamilton, D. C., Voss, H. D., Roelof, E. C., and Brent, P. C.: 2001, *Geophys. Res. Lett.* **28**, 1151.
- Mitchell, D. G., Krimigis, S. M., Cheng, A. F., Jaskulek, S. E., Keath, E. P., Mauk, B. H., McEntire, R. W., Roelof, E. C., Schlemm, C. E., Tossman, B. E., and Williams, D. J.: 1996, in: *Proceedings SPIE International Symposium on Optical Science Engineering and Instrumentation*, Mission to the Sun, Vol. **2803**, p. 154.
- Ness, N. F., et al.: 1982, *J. Geophys. Res.* **87**, 1369.
- Neubauer, F. M.: 1992, in: *Proceedings of the Symposium on Titan*, Toulouse, France, ESA SP-338, p. 267.
- Paonessa, M. and Cheng, A. F.: 1986, *J. Geophys. Res.* **91**, 1391.
- Paranicas, C., Cheng, A. F., and Williams, D. J.: 1998, *J. Geophys. Res.* **103**, 15001.
- Paranicas, C. P., Mauk, B. H., and Krimigis, S. M.: 1991, *J. Geophys. Res.* **96**, 21135.
- Prangé, R., Zarka, P., Ballester, G. E., Livengood, T. A., Denis, L., Carr, T., Reyes, F., Bame, S. J., and Moos, H. W.: 1993, *Geophys. Res.* **98**, 18779.
- Reiner, M. J., Fainberg, J., Stone, R. G., Kaiser, M. L., Desch, M. D., Manning, R., Zarka, P., and Pedersen, B. M.: 1993, *J. Geophys. Res. Planets* **98**, 13163.
- Roelof, E. C.: 1992, in: Marsh, E., and Schwenn, R. (eds.), *Proceedings of the 3rd COSPAR Colloquium*, p. 385.
- Roelof, E. C.: 1987, *Geophys. Res. Lett.* **14**, 652.
- Roelof, E. C. and Williams, D. J.: 1990, *Johns Hopkins APL Tech. Dig.* **11**, 72.
- Roelof, E. C., Mitchell, D. G., and Williams, D. J.: 1985, *J. Geophys. Res.* **90**, 10991.
- Sandel, B. R. and Broadfoot, A. L.: 1981, *Nature* **292**, 679.
- Satoh, T., Connerney, J. E. P., and Baron, R. L.: 1996, *Icarus* **122**, 1.
- Schneider, N. M. and Trauger, J. T.: 1995, *Astrophys. J.* **450**, 450.
- Schulz, M. and Lanzerotti, L. J.: 1974, *Particle Diffusion in the Radiation Belts*, Springer-Verlag.
- Shemansky, D. E. and Hall, D. T.: 1992, *J. Geophys. Res.* **97**, 4143.
- Simpson, J. A., Bastian, T. S., Chenette, D. L., McKibben, R. B., and Pyle, K. R.: 1980, *J. Geophys. Res.* **85**, 5731.
- Sittler, E. C., Ogilvie, K. W., and Scudder, J. D.: 1983, *J. Geophys. Res.* **88**, 8847.
- Van Allen, J. A.: 1984, in: Gehrels, T., and Matthews, M. S. (eds.), *Saturn*, p. 281.
- Williams, D. J. and Mauk, B. H.: 1997, *J. Geophys. Res.* **102**, 24283.
- Williams, D. J., Mauk, B., and McEntire, R. W.: 1997a, *Geophys. Res. Lett.* **24**, 2953.
- Williams, D. J., Mauk, B. H., McEntire, R. W., Roelof, E. C., Armstrong, T. P., Wilken, B., Roederer, J. G., Krimigis, S. M., Fritz, T. A., Lanzerotti, L. J., and Murphy, N.: 1997b, *Geophys. Res. Lett.* **24**, 2163.
- Williams, D. J., Mauk, B. H., McEntire, R. W., Roelof, E. C., Armstrong, T. P., Wilken, B., Roederer, J. G., Krimigis, S. M., Fritz, T. A., and Lanzerotti, L. J.: 1996, *Science* **274**, 401.
- Williams, D. J., McEntire, R. W., Schlemm, C. E., Lui, A. T. Y., Gloeckler, G., Christon, S. P., and Gliem, F.: 1994, *J. Geomagn. Geoelectr.* **46**, 39.
- Witte, M., Banaszkiewicz, M., and Rosenbauer, H.: 1996, *Space Sci. Rev.* **78**, 289.



- Woch, J., Krupp, N., Lagg, A., Wilken, B., Livi, S., and Williams, D. J.: 1998, *Geophys. Res. Lett.* **25**, 1253–1256.
- Woch, J., Krupp, N., Khurana, K. K., Kivelson, M. G., Roux, A., Perraut, S., Louarn, P., Lagg, A., Williams, D. J., Livi S., and Wilken, B.: 1999, *Geophys. Res. Lett.* **26**, 2137–2140.
- Zwickl, R. D., Krimigis, S. M., Carbary, J. F., Keath, E. P., Armstrong, T. P., Hamilton, D. C., and Gloeckler, G.: 1981, *J. Geophys. Res.* **86**, 8125.